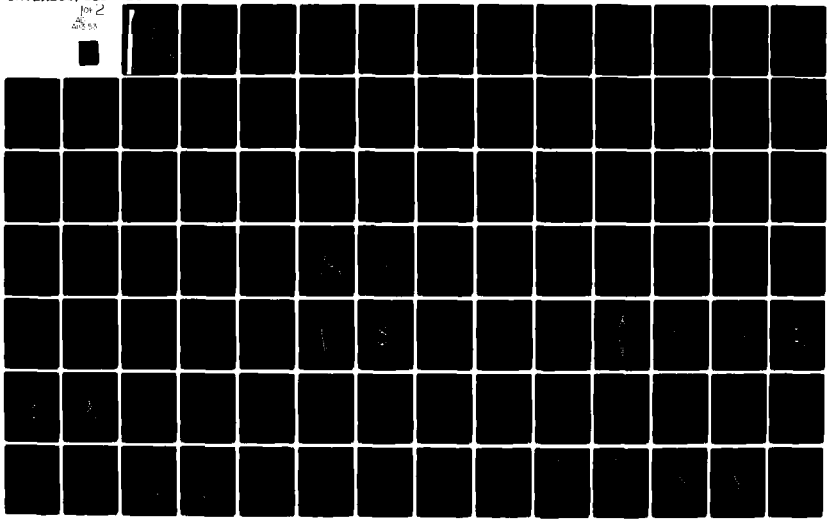


AD-A113 153

BRISTOL UNIV (ENGLAND) DEPT OF AERONAUTICAL ENGINEERING F/6 28/4
PRESSURES ON A SLENDER, AXISYMMETRIC BODY AT HIGH ANGLE OF ATTA—ETC(U)
JAN 62 P C DEXTER, J W FLOWER DAJAS7-61-C-0052
DLH/PC08201 NL

UNCLASSIFIED

for 2
2025



12

Report No. / PCD8201
R/D-3033-AN

AD A11 3153

UNIVERSITY OF BRISTOL

DEPARTMENT OF
AERONAUTICAL ENGINEERING



PRESSURES ON A SLENDER, AXISYMMETRIC BODY AT
HIGH ANGLE OF ATTACK IN A VERY LOW TURBULENCE
LEVEL AIR STREAM

Final Report
by
P. C. Dexter and J. W. Flower

January 1982

US ARMY EUROPEAN RESEARCH OFFICE
AND
US AIR FORCE EUROPEAN OFFICE OF
AEROSPACE RESEARCH AND DEVELOPMENT

London, England

Grant Number DAJA37-81-C-0052

Approved for Public Release; distribution unlimited

DTIC
SELECTED
APR 6 1982
H

DTIC FILE COPY

UNCLASSIFIED

SECURITY CLASSIFICATION OF THIS PAGE (When Data Entered)

R&D 3033-A1

REPORT DOCUMENTATION PAGE		READ INSTRUCTIONS BEFORE COMPLETING FORM
1. REPORT NUMBER	2. GOVT ACCESSION NO. AD-A113153	3. RECIPIENT'S CATALOG NUMBER
4. TITLE (and Subtitle) Pressures on a Slender, Axisymmetric Body at High Angle of Attack in a Very Low Turbulence Level Air Stream		5. TYPE OF REPORT & PERIOD COVERED Final Technical Report 18 Dec 80 - 17 Dec 81
7. AUTHOR(s) P.C. Dexter and J.W. Flower		6. PERFORMING ORG. REPORT NUMBER
9. PERFORMING ORGANIZATION NAME AND ADDRESS University of Bristol Department of Aeronautical Engineering Bristol, UK.		8. CONTRACT OR GRANT NUMBER(s) DAJA37-81-C-0052
11. CONTROLLING OFFICE NAME AND ADDRESS USARDCG-UK Box 65 FPO NY 09510		10. PROGRAM ELEMENT, PROJECT, TASK AREA & WORK UNIT NUMBERS 6.11.02A 1T161102BH57-06
14. MONITORING AGENCY NAME & ADDRESS (if different from Controlling Office)		12. REPORT DATE January 1982
		13. NUMBER OF PAGES 113
		15. SECURITY CLASS. (of this report) Unclassified
16. DISTRIBUTION STATEMENT (of this Report) Approved for Public Release; distribution unlimited		15a. DECLASSIFICATION/DOWNGRADING SCHEDULE
17. DISTRIBUTION STATEMENT (of the abstract entered in Block 20, if different from Report)		
18. SUPPLEMENTARY NOTES		
19. KEY WORDS (Continue on reverse side if necessary and identify by block number) High Angle of Attack Aerodynamics Side Forces and Side Moments		
20. ABSTRACT (Continue on reverse side if necessary and identify by block number) This report describes experimental work which has been carried out to investigate the flow over axisymmetric slender bodies at high angles of incidence. Surface pressure measurements were made on the cylindrical section of a rigidly mounted nose/cylinder model in a low speed, very low turbulence level freestream at incidences from 30° to 90° and for the full roll angle range. Tests were performed for a variety of different nose shapes at subcritical Reynolds numbers and the pressure data was integrated to produce local side and normal force coefficient distributions. Much of		

DD FORM 1 JAN 73 1473 EDITION OF 1 NOV 65 IS OBSOLETE

UNCLASSIFIED

SECURITY CLASSIFICATION OF THIS PAGE (When Data Entered)

UNCLASSIFIED

SECURITY CLASSIFICATION OF THIS PAGE(When Data Entered)

20. Contd.

the data was generated using three calibre ogive nose profiles, but in all cases the model roll orientation was found to significantly affect the side and normal forces. The side forces were reduced by both hemispherical nose blunting and by using shorter ogival noses. A two calibre conical nose was also used. Details of surface oil flow visualisation are presented.

Accession For	
NTIS	<input checked="" type="checkbox"/>
DTIC	<input type="checkbox"/>
USMA	<input type="checkbox"/>
Indefinite	<input type="checkbox"/>
By	
Distribution	
Availability	
Special	

A



UNCLASSIFIED

SECURITY CLASSIFICATION OF THIS PAGE(When Data Entered)

SUMMARY

This report describes experimental work which has been carried out to investigate the flow over axisymmetric slender bodies at high angles of incidence. Surface pressure measurements were made on the cylindrical section of a rigidly mounted nose/cylinder model in a low speed, very low turbulence level freestream at incidences from 30° to 90° and for the full roll angle range. Tests were performed for a variety of different nose shapes at subcritical Reynolds numbers and the pressure data was integrated to produce local side and normal force coefficient distributions. Much of the data was generated using three calibre ogive nose profiles, but in all cases the model roll orientation was found to significantly affect the side and normal forces. The side forces were reduced by both hemispherical nose blunting and by using shorter ogival noses. A two calibre conical nose was also used. Details of surface oil flow visualisation are presented.

TABLE OF CONTENTS

	<u>Page No.</u>
1. INTRODUCTION	1
2. APPARATUS	3
2.1 Wind Tunnel Equipment	3
2.2 Data Recording Equipment	4
3. TEST PROCEDURE	6
4. RESULTS	7
4.1 Three Calibre Ogive Nose	7
4.1.1 50° Angle of Incidence	7
4.1.2 Independent Nose Rolling	10
4.1.3 Other Incidence Angles	11
4.1.4 Correlation of Results	17
4.1.5 Effect of Reynolds Number	17
4.2 Other Nose Geometries	18
4.2.1 Effect of Nose Blunting	19
4.2.2 Effect of Nose Length	21
4.2.3 Two Calibre Conical Nose	22
4.3 Normal Force	23
5. FLOW VISUALISATION	25
6. CONCLUSIONS	31
7. REFERENCES	34
8. NOTATION	35

1. INTRODUCTION

It has been known for over twenty-five years that axisymmetric bodies are subject to side forces when inclined at high angles of incidence to a uniform stream. Since the late 1960's much experimental work has been reported on high incidence research as the need to enlarge the flight envelopes of missiles and bodies arose. Indeed a recent paper by Ericsson and Keating (ref. 1) include well over 100 references relevant to high incidence flow fields. However, much of this earlier work showed inconsistencies, and although certain trends emerged it was not difficult to find exceptions. Often large discrepancies were found between results of different workers. The extent of the problem was illustrated by the study of Wardlaw and Morrison (ref. 2) in which they were forced to try correlating side force measurements by linear regression. They found that ordinary conventional flow and geometry parameters were insufficient owing to the wide margin of differences in available data. Even now there are still areas of high incidence aerodynamics where the fundamental causes of some of the observed flow features are disputed.

The present study was originated in order to try to understand why there should be such large differences in the data. It was planned to undertake some very careful experiments to try to isolate different contributing factors and hence to find ways in which reliable data could be produced. If these methods could be established then it would become possible to collect data which could be used to investigate the effects of varying conventional flow and geometry parameters in the normal way.

Previous experimental studies had given some clues as to the origins of the difficulties. It had been found by most experimenters who looked for it that the side force might vary in both size and direction at different roll angles. It was also found by Lamont and Hunt (refs 3 and 4) that unsteadiness, both from the mounting system and the freestream turbulence, caused experimental difficulties. Their transient records showed differences in switching pattern with roll angle while the inferred unswitched levels seemed to be unaffected. They postulated that the observed influence of roll angle on the time-averaged results would be eliminated if the unsteadiness were eliminated.

The initial work of this study was performed under U.S. Army Grant number DA-EOR-77-G-073 and has been reported in three volumes (refs 5-7). Initially the study set out to check on Lamont and Hunt's (refs 3 and 4) notion of the importance of freestream turbulence using a rigidly mounted model in a very low turbulence level freestream. The model used was the same as that used by Lamont and Hunt and at the same subcritical Reynolds numbers. It was found, as reported in ref. 5, that freestream turbulence did have a significant effect on the time-dependent pressures on the body, but that there was still a roll angle variation. The mean value of the measured pressures was changing as the roll angle changed, but there were no large variations in the time-dependent pressures as Lamont and Hunt had observed in their tests. Hence the

change in mean level was not due to the variation in switching pattern as they had suggested.

Knowing that there was still a roll angle variation even in a very low turbulence freestream, an effort was made to see if this could be eliminated using an accurately manufactured model. It was shown (ref. 6.) that although it may not be impossible, it was certainly very difficult, and for most applications it is likely that there will be a roll angle dependence.

This report gives more information, in addition to that of refs 5-8, on the work which has been conducted into determining the effects of the roll angle dependence, and of how reliable data may be obtained at high angles of incidence. A suitable method was developed based on previous experience and this was used to obtain results which are presented and discussed for a variety of different model nose geometries, including hemispherical nose blunting.

The work has been conducted by measuring pressure distributions over the model body. This method, although slower than force measurements, produces much more information concerning the flow around the model. It is possible, for instance, by comparing the pressure distribution at a given model station to that around a circular cylinder at 90° to a uniform flow, to determine that all these tests were performed with laminar separation. As mentioned in the text, force measurements may overlook some important feature of the flow which may even lead to incorrect conclusions being drawn.

Additionally some surface flow visualisation tests have been performed and are discussed in this report. It was hoped that they might provide a greater understanding of the flow around the model but merely illustrated how complex the problem is with a series of primary and secondary vortices and consequent separations.

2. APPARATUS

2.1 Wind Tunnel Equipment

The work reported here was conducted in the 4 ft x 3 ft Experimental Low Turbulence Wind Tunnel at R.A.E. Farnborough. This tunnel has a contraction ratio of 31.1:1 with a working section of 1.2 m x 0.9 m, which has a free-stream turbulence level of about 0.01% over the majority of its cross-sectional area. The maximum tunnel speed is about 250 ft/sec (about 75 m/sec).

The model used for most of the tests consists basically of several 51 mm diameter screw-in sections which form a nose-cylindrical body configuration. Various different nose shapes have been used in the study, although the large majority have been with a three calibre tangent ogive nose. The measurement part of the model is constructed in five identical sections, each 1 diameter long and housing two measurement stations. At each measurement station there are 36 pressure tappings at 10° intervals around the body and each tapping has narrow bore pressure tubing connected to it.

The nose section can screw directly into the measurement section or can be attached via a dummy section (as in fig. 1) which effectively increases the length of the measurement section. The dummy section was carefully made to ensure that the roll angle of the nose relative to the measurement section is unchanged, whether the dummy is used or not. During the course of wind tunnel testing the section nearest the nose became damaged and had to be replaced. This resulted in the body being rotated through approximately 170° roll angle relative to the nose. However all roll angles were measured relative to the nose at all times as it was proved beforehand, and borne out by subsequent results, that the nose roll angle is dominant in determining the flow over the body (see section 4.1.2). Hence the change in model section had little effect.

The measurement section screws into the support section which is held by model clamps. The clamps actually grip a pair of roller bearings fitted accurately on to the support section and allow the model to be rolled but prevent it vibrating. The model support clamps are rigidly held by 51 mm diameter steel pylons to the roof and floor of the wind tunnel which is braced externally against a steel framework. The model rotates in a horizontal plane to achieve incidence. Roll angle is controlled by means of a worm driven by a flexible cable. The worm engages on a gear mounted on the rear of the body. Roll angle is read directly from a scale on the model support body. The 360 tubes from the pressure tappings in the model measuring section are led through the inside of the model, along the tunnel floor and into the observation room. They terminate in a total of 10 Scanivalve rings which can be connected in turn to the five Scanivalves of the newly made data acquisition system. The pressures from each tube were read several times, usually three, by the new system and then transferred to paper tape for storage. Subsequently the readings were fed on to a computer back at

Bristol University for processing and analysis of results. These measurements gave the pressure distribution over a large part of the body and by numerical integration enabled the local side and normal force coefficients to be determined at each measurement station.

The test technique used has been evolved from previous experience of using this model with a different data recording system which would allow only one Scanivalve ring to be read at a time. Also tests were performed using a wool tuft grid placed in the lee of the body to study the flow patterns generated. It was found that the flow with the three calibre ogive nose was quite stable and exhibited similar degrees of asymmetry, which may be of either 'hand', over large roll angle ranges (this will be discussed later). This behaviour was found over most of the incidence range covered in these tests, and so for the other nose shapes a test technique was used which involved a roll angle traverse at just one incidence to determine the ranges over which the flow was in the asymmetric state. This was done with the wool tuft grid and with pressure measurements. Tests at other angles of incidence were then performed for just two roll angles, one for each of the 'hands' of the asymmetric state. This technique is discussed later in section 4.2.

2.2 Data Recording Equipment

The experience gained from wind tunnel tests when first using the multi pressure tapped model showed that the data recording equipment available was not very well suited to this application. The equipment was a Solartron Data Logger, belonging to the Aeronautical Engineering Department at Bristol University, weighing about 50kgms and measuring approx. 56 cms x 85 cms x 94 cms. Eventime testing was to be undertaken this had to be transported 100 miles to R.A.E. Farnborough and installed in the 4 ft x 3 ft low turbulence wind tunnel which involved awkward manoeuvring up some steep steps. Additionally, the Data Logger was capable of recording readings from only one Scanivalve at a time which meant that each test was taking approximately an hour. This was not making the best use of available tunnel time and was also a rather tedious process.

Consequently provision was made in this contract to purchase additional Scanivalves and transducers and to build a microprocessor-controlled data acquisition system with five channels which would be more portable than the old system and would speed up recording times considerably. The design, construction, programming and testing of the system took about half of the contract time but proved to be very successful.

The system is comprised of five basic parts. They are:-

- (1) Intel 8085 Microprocessor and power supply unit
- (2) A to D and interfaces cabinet
- (3) Scanivalves and 24 volt d.c. power supply

- (4) Pressure transducers and associated equipment
- (5) Terminal, screen and paper tape punch

They are shown diagrammatically in figure 2. The microprocessor is programmed to control up to five separate channels simultaneously, where each channel comprises a Scanivalve and transducer, a Scanivalve stepping/homing interface, an A to D channel and a microprocessor I/O port. The program is fairly flexible in that any or all of the channels can be controlled and any sequence of port stepping can be specified by the user. The length of settling time per port and the time between, plus number of readings at each port, are also user specified. Readings are taken by means of a multiplexed 12 bit analogue to digital converter (A to D) providing 4096 different possible combinations, which gives a reading error of less than $\pm 0.02\%$ full scale. The readings are stored in memory whilst the data are being acquired. Subsequently they can be written on to the terminal screen for inspection or on to paper tape for storage and transfer to computer.

The program is written so that readings on a given channel are taken immediately before the associated Scanivalve is stepped on to its next port. The Scanivalve is held at this port for a period to allow the pressure to settle. Each channel behaves in the same way and it is during this settling time that the other channels are read and stepped on. Consequently data are collected from five channels on this new system in the same time that it took the old system to read one channel.

Having five recording channels available on this data acquisition system meant that some extra equipment had to be made to take full advantage of the increased capacity. A power supply unit was built which could provide five 24 volt d.c. supplies to the transducers. Each channel had to be isolated because of the transducer electronic design. Additionally a five channel low pass filter/amplifier was designed and built to process the output signal from the transducers before being passed into the A to D converter. The low pass filter was designed with a 4 Hz cut off frequency which would prevent high frequency unsteadiness from passing but also allow a reasonably short settling time to be used. The amplifier stage was designed to match the maximum transducer output voltage to the full scale reading of the A to D converter and hence improve the resolution of the data readings.

TEST PROCEDURE

The basic model used in these tests is described in section 2. The model was installed in the wind tunnel such that all but the very worst flow-induced model vibrations were eliminated. In the great majority of test conditions no model vibrations could be observed and even for those cases where the nose tip could be seen vibrating (around 20° incidence, with the three-caliber ogive model) their amplitude was very small, less than $\pm 0.2 \mu\text{m}$ measured by traveling microscopes. The initial test in each test series was conducted at 30° incidence and zero roll angle. This was to check that the roll angle datum was being correctly aligned and also served to indicate which pressure tubes, if any, were giving false readings. Generally these were very few, 3 or 4, and were probably due to leaks. Although it is realized that inflow or outflow of air from the pressure tapping on the model surface may possibly have some effect on the flow it was considered better not to try to cure the leaks because any attempt to get at the tubes inside the model was likely to cause more damage than it could mend. Provision was made in the data reduction to allow for these known erroneous readings which were corrected by interpolation.

The test procedure with the new data acquisition system was slightly different to that with the old data logger. When using the new system the tunnel would be run up to speed and then readings taken from five of the ten scanivalve rings. The readings would be inspected on the terminal and if there were no obvious errors would be stored on paper tape. The model would then be rolled to the next test roll angle and readings again taken from the same five rings. This procedure would be repeated until all the planned roll angles had been covered at which time the tunnel would be run down and the nose returned to its original roll angle. The Scanivalve rings would then be swapped over so that those previously not used would be connected to the data acquisition system. Note that at all times the rings which were not being read were dicked off. The tunnel would then be run up again and the test continued as before. This method did mean that the model was rotated between having the first half of its pressure distribution measured and the second half but it was found that this rarely caused any problem. The model roll angle could be aligned fairly accurately and it was known from previous testing that the flow depended on the model roll orientation even if the tunnel was spinning when the model was rolled. The only occasions where discontinuous data were obtained between the two halves were when the model was in a roll angle position between two opposite 'hands' of the more normal asymmetric flow. Generally in these regions the flow pattern change rapidly with roll angle and even a tiny slippage in roll alignment could be noticeable.

The test method with the old data logger was much slower. The model was aligned in roll angle and the tunnel run up. Readings were then recorded from all the scanivalve rings, connecting each in turn to the single scanivalve until all ten were completed. The tunnel was then run down at the end of the test.

4. RESULTS

The results obtained in this investigation have nearly all been pressure measurements. Generally the pressures measured around each body station have been reduced to coefficient form, based on crossflow dynamic pressure, and integrated to give local normal force and side force coefficients, based on crossflow dynamic pressures and body diameter. Most of the discussions will be about the force distributions which are of a form shown in figure 3. The normal force reduces from the nose rearwards and the side force has a cyclic distribution with each successive peak reducing in magnitude. Various points on this diagram are identified for future use in discussions. They are

$C_{y_{max_1}}$, $C_{y_{max_2}}$ corresponding to peak values

x_{max_1}/D , x_{max_2}/D corresponding to the positions of the peak values

x_0/D corresponding to the position of a node in the side force distribution.

Unless stated otherwise all results were obtained at a Reynolds number of 10^5 where Reynolds number is defined as $(VD \cos \alpha)/\nu$.

4.1 Three Calibre Ogive Nose

A three calibre ogive nose shape has been used for the majority of this investigation. Testing with this nose began in the work programme well before the start of this contract but previous results will be included for completeness. It had been noted early on that the flow was dependent upon roll angle of the model and to assist in investigating the cause of this phenomenon it was desirable to have two noses of the same profile. There was already available a three calibre ogive, made of aluminium alloy, so a new three calibre ogive was also constructed, but out of stainless steel in order to get a better surface finish. They are referred to as the old nose and the new nose respectively. The old nose was a veteran of many wind tunnel tests and consequently no longer had a good surface finish and even had some identifiable small dents. The new nose was finished quite well but even so had a few marks, mainly from the manufacturing process.

4.1.1 50° Angle of Incidence

A great many tests were performed using these noses, with the majority of the tests at an incidence angle of 50°. This angle was chosen because the flow over the body produced steady pressures, determined from early time-dependent pressure testing (ref. 5), and a highly asymmetric flow. Initially the tests at this incidence covered the full roll angle range for both noses in 30° intervals. These results were obtained with the old data logger system, but subsequently the resolution was improved by reducing the roll angle step length to only 10° intervals throughout the full 360° of roll. These later tests were performed with the new data acquisition system. Very good agreement was found between the two methods, including repeat tests. A typical force distribution is shown in figure 4 for a roll angle of 0°. Note that at

positions $x/D = 7.5$ and 8.0 there are duplicated readings. This is because the first part of the distribution from $x/D = 3.5$ to 8.0 is obtained without the dummy section included in the model and the second part from $x/D = 7.5$ to 12.0 is with the dummy. There is good agreement obtained at this crossover which means that lengthening the model had little effect on the flow. This indicates that although the nose was placed in a different part of the wind tunnel flow the results were not affected and also that the influence of the large model support pylons does not reach as far upstream as the last measuring station on the model.

Figure 5 shows the side force distribution obtained with the old nose at 50° incidence for 12 different roll angles at 30° intervals. A similar diagram is shown in figure 6 for the new nose. In order to make some sense of these figures the value $C_{y_{max_1}}$ for each curve, plus the values obtained for all the other intermediate roll angles, has been plotted against roll angle for both noses in figure 7. Study of this figure shows that the flow depends very much on roll angle. There appears to be a regular state for the flow giving a magnitude for $C_{y_{max_1}}$ of around 2. The flow may be of either 'hand', but if we consider the nature of the flow this is not surprising. Twin vortices are formed in the lee of the body over the nose and they become asymmetric, with one of them growing and separating from the body before the other. The sign of the side force is merely an indication of which side the first vortex is shed from. Hence it would appear that for most of the roll angle range the flow is tending towards the regular state, of one hand or the other. However, there are the crossover regions between these two hands where the flow is clearly different. Even though at this incidence the crossover generally occurs fairly rapidly with roll angle the flows found through the crossover region are steady, stable flows. They produce lower side forces and a more 'stretched out' distribution of side force along the body length as seen in figures 5 and 6. Generally they are also associated with lower normal forces too but this will be discussed later in section 4.3.

Although the flow has the two preferred hands of a more regular state it is still quite possible to get any value of $C_{y_{max_1}}$ between these two extremes. Considering again the flow it is not easy to visualise why this happens. If the initial twin vortices become unstable in some way for most roll angles what is happening to prevent this in these crossover regions? It could be that asymmetric disturbances in the flow over the body are enough to give rise to the 'regular' state for most roll angles, but in the crossover regions the disturbances to the flow are almost symmetric. This could lead to a less settled flow than for the regular state, due to these disturbances, but also it could result in the flow remaining basically symmetric, at least for time-averaged readings. This is a hypothesis which is confirmed to a certain extent by the time-dependent pressure measurements in ref. 5. An alternative is that at the point in the crossover region where there is zero side force the flow experiences no disturbances and so remains symmetric. However this seems unreasonable because even a small disturbance in the wind tunnel flow should be enough to trigger the instability, and it was found that the zero

side force could be maintained indefinitely in tests. The fact that the regular state remains largely unaltered at this incidence for most roll angles suggests that once there is a sufficient asymmetry in the flow disturbances over the body then any increase in asymmetry has little further effect. There will be more discussion on a 'regular' state later when considering other angles of incidence.

The difference between the flows of one hand of the regular state, with high side force values, and a case in a crossover region with very low side forces can be seen by looking at their pressure distributions. The side force distribution for the old nose at zero roll angle, corresponding to a regular state, is shown in figure 4. It can be seen from figure 7 that a zero side force case for the old nose could be expected at a roll angle of about 235° . In fact the zero case occurred at $\phi = 231\frac{1}{2}^\circ$ and the force distribution is presented in figure 8. It is evident that there is virtually no side force all along the length of the measuring section of the body. Notice too the low normal force values. Also shown are cases obtained at the same time but for roll angles of approximately $\frac{1}{2}^\circ$ either side $\phi = 231\frac{1}{2}^\circ$. These show how rapidly the crossover is occurring in this region.

Two pressure distributions for a regular case are presented in Figure 9. They are similar in form, but correspond to sectional side forces of opposite sign, one from the first half cycle of the distribution and one from the second (compare with the force distribution of Figure 4). The degree of asymmetry is larger at $x/d = 3.5$, corresponding to the larger side force value of 2.2 (compared to 1.2 at $x/d = 6$). Tracing the curves from the windward generator (either $\theta = 0^\circ$ or $\theta = 360^\circ$), there is a rapid acceleration along the windward face of the body, followed by a small pressure recovery and separation of the primary boundary layer. The small pressure rise to separation is consistent with the boundary layer being laminar. These pressure distributions are qualitatively similar to those presented by Lamont and Hunt (see Figure 25 of Reference 3).

Pressure distributions at the same two stations are shown in Figure 10 for the roll angle of Figure 8 where the side force amplitude is virtually zero. The high degree of symmetry in the pressure distributions can be seen. The primary separations are again laminar. The rapid pressure rise toward the leeward generator suggests that the wake flow consists of twin, symmetric vortices. The flow reattaches along the leeward generator and accelerates along the back of the body until secondary separations occur, see section 5 for a more detailed description. This pair of vortices forms over the nose section of the body and remains present along the body length, without becoming asymmetric. This has been observed using a wool tuft grid (ref. 7). It is known that the flow in the regular state starts with twin vortices over the nose but these rapidly become asymmetric, and the flow in the lee of the body seems to be less unsteady than for the symmetric case, judging by pressure measurements (ref. 5) and wool tuft grid tests (ref. 7). However the symmetric case is a stable flow. Indeed if it were producing a time-varying flow as in the case of a von Karman vortex

street behind a circular cylinder the pressure distribution would be more like that shown in figure 11 where there is no pressure recovery near the leeward generator. In fact this is seen in figure 12 for the pressure distribution obtained at $x/D = 11.5$ on a regular case ($\phi = 0^\circ$ with the old nose). At a station this far back on the model the flow is tending more and more to become like that found on an infinite yawed circular cylinder with a von Karman vortex street type of flow. This was found in the early time-dependent pressure measurements made in this study and reported in ref. 5. Clearly the flow over the upstream stations of the body for the zero side force case is not of this form.

4.1.2 Independent Nose Rolling

The above results showed a strong roll angle dependence. The pressure distributions, such as those in figure 9, indicated that the asymmetry in the flow started over the nose, ahead of the first measuring station. This suggested that the flow was probably dependent upon the roll orientation of the nose section only. In order to verify this a new model section was designed and constructed which would allow the nose to be rolled independently of the body and is shown in figure 13. The section is $\frac{1}{2}$ calibre long which means that the first measuring station is at $x/D = 4$ rather than 3.5.

A series of tests was undertaken at 50° incidence using this extra rotator section in combination with both of the three calibre ogive noses. The first tests were performed keeping the cylindrical body section at the datum roll angle, $\phi = 0^\circ$, but with the nose rotated through 360° in 30° steps. These results showed generally good agreement between the corresponding cases where just the nose was rolled and where the whole model was rolled. Typical cases for each nose are shown in figures 14 and 15 for both a regular case with large side forces and an intermediate case with low side forces. In the regular cases the agreement is quite good for both normal force and side force distributions. Notice that the position of the first peak in the side force distribution, $C_{y_{max1}}$, occurs ahead of the first measuring station when the rotator section is included, so this cannot be used as a correlating parameter.

The intermediate case for the old nose is at $\phi = 60^\circ$ which is in a rapid crossover region between two regular 'hands'. Because the flow varies rapidly with roll angle (see figure 7) any slight misalignment in roll angle would be enough to cause the discrepancy shown in figure 14. This is true for any of the crossover regions. The intermediate case for the new nose in figure 15 shows good agreement for side and normal force but this is not in a crossover region. It is a roll angle where the side forces are generally low, see figure 7, so a slight misalignment would not produce any dramatic changes.

In order to correlate the results through the total roll angle range a correlating parameter was necessary. As it is known that the force distributions either are in generally good agreement throughout the length of the model measurement section, or they disagree over the entire length, it is

enough to choose the value of the local side force coefficient at the first measuring station ($x/D = 4$). This is as close to $C_{y\max}$, as can be attained for the regular cases. These values were plotted against nose roll angle for both noses in figure 16 which also shows the corresponding measurements for the cases where the whole model was rolled. It can be seen for each nose that the variation of side force with roll angle is very similar whether just the nose or the whole model is rolled. The best agreement in this respect is with the old nose, which is the less perfect of the two. As it is probably the geometric imperfections of the nose which cause the flow disturbances and hence determine the hand of the flow this might be expected.

Tests were performed using the rotator section to see if the roll orientation of the body rather than the nose could be responsible for the roll angle variation. The model was set at 50° incidence with the nose at the datum angle, $\phi = 0^\circ$, and the cylindrical body section was set to roll angles of 0° , 90° , 180° and 270° with each nose. The old nose was also tried at $\phi = 60^\circ$. In each of these cases it was found that the roll position of the body had no effect on the force distributions at all. A typical result is shown in figure 17 where the old nose is at $\phi = 0^\circ$ and the body at $\phi = 90^\circ$. Also shown is the result for the whole model at $\phi = 0^\circ$ and it can be seen that the agreement is excellent. Note from figure 7 that in the case where the whole model is at $\phi = 90^\circ$, the other hand of the regular state would have been found. These results proved that the cylindrical section has little effect on the flow development.

Hence the conclusion from these tests must be that the roll orientation of the nose is of over-riding importance in determining the subsequent flow over the rest of the body. It has not been proven here but it is likely that the front of the nose is most important. Judging from the side force distributions the flow asymmetries begin well toward the front of the nose at this 50° incidence (although extrapolation is an unsatisfactory procedure) and the asymmetries are probably caused by the minor geometry of the nose. (Some ad hoc tests reported in ref. 5 indicate the importance of the tip region.) Once the asymmetry in the flow has been established then any other geometric imperfections will have to be larger than those nearer the tip in order to have any significant effect on the flow. As wind tunnel models are generally made quite well the size of imperfections are evenly distributed over the body, and so the region nearest the nose tip is of most importance.

4.1.3 Other Incidence Angles

Having performed extensive tests at 50° incidence it was desirable to extend the coverage to get results throughout the incidence range where side forces were developed and could be measured. Hence results were obtained from 25° incidence upwards and for both of the three calibre ogive noses. The table below gives details of configurations tested. The entries in the table indicate the range of roll angle covered and the step size of the roll angle increment, in degrees.

<u>Incidence Angle^o</u>	<u>New Nose</u>	<u>Old Nose</u>
25	-	0,270
30	0(45)360	0(45)360
35	-	0(30)360
40	0(30)360	0(30)360
45	-	0(30)360
50	0(10)360	0(10)360
55	-	0(30)360
60	0(30)360	0(30)360
65	-	0(30)360
70	0(90)360	0(90)360
75	0(90)360	0(90)360
90	0	0

In some cases the results were obtained over the first ten measuring stations and in the others over all twenty stations.

Results obtained from most of these tests are presented in figures 18 to 31 which are plots of local side force coefficient distribution. Generally normal force has not been included as the figures would be even more complicated than they already are (see section 4.3).

At the lowest incidences (up to 30^o) the new nose generated only very small side forces at any roll angle. Figure 18 gives an indication of results at 30^o incidence with the highest side forces that were encountered. All the other cases fell between these extremes. Some of these tests were repeated and agreement was good. Above 30^o incidence the flow became asymmetric and exerted side forces on the body. Figures 19, 6 and 20 show measured side force distributions for 12 roll angles at 40^o, 50^o and 60^o incidence respectively. Notice that the distribution becomes more compressed towards the front of the model as the incidence increases until at 60^o most of the first half cycle of the distribution is occurring ahead of the measurement section of the body on the nose. At 70^o incidence the results of figure 21 showed side forces remaining only at one of the four roll angles tested. This was at zero roll angle. The other cases were all very similar to the one shown at 90^o roll. At 75^o incidence no side forces could be found in the measurements as shown in figure 21 for the same two roll angles.

The lowest incidence that the old nose was tested at was 25^o, for two roll angles. The measurements, in figure 22, indicated that the flow was slightly asymmetric, even at this low incidence, for these particular roll

angles. It had been anticipated from other results at higher incidences that these roll angles were most likely to produce measurable side forces. At 30° incidence figure 23 shows results at four roll angles clearly indicating that side forces are being developed. Measurements obtained at each of 12 roll angles for incidences of 35°, 40°, 45°, 50°, 55°, 60° and 65° are shown in figures 24 to 26, 5, and 27 to 29 respectively. Again in these figures it can be seen that the side force distribution becomes compressed towards the front of the model as the incidence increases. At 70° incidence figure 30 indicates that the flow still develops side forces, though mostly on the nose section, and at 75° incidence figure 30 shows that the side forces have just about died away, even for the roll angle of 270°, which results at other incidences would suggest is the most likely case to produce them. At 90° incidence the body behaves just like a circular cylinder across a uniform stream and produces zero time-averaged side force loading along the body length. This is shown for both noses in figure 31.

It is noticeable from the preceding figures that side forces are present on the old nose at lower angles of incidence than they are on the less imperfect new nose, and that the maximum values generally obtained in the side force distribution is higher for the old nose than for the new at incidences between about 30° and 50°. However, at angles of 50° and above the values are about the same. Also it can be seen that the forces vary with roll angle at all of the incidences.

In order to make these points clearer the results of the above figures for both noses have been correlated by plotting values of the maximum local side force coefficient occurring in the first half cycle of the distribution, i.e. $C_{y_{max1}}$, against roll angle in figures 32 and 33. At incidences greater than 50° the position of $C_{y_{max1}}$ is occurring on the nose, ahead of the first measuring station so in figures 34 and 35 $C_{y_{max2}}$ has been used. This is the value of the second peak in the side force distribution, which is of opposite sign to the first and seems to be generally related to it.

Figure 32 shows that at 30° incidence the peak value of side force coefficient varies over a narrow range for most of the cases except 2 roll angles of the old nose. These give much the highest values, one of each sign, or 'hand'. Otherwise the variation is not very strong with roll angle. At 40° incidence, in figure 32, the roll angle variation has a greater effect and the magnitudes of $C_{y_{max1}}$ are generally larger for the old nose. The ranges of roll angle where low side forces can exist are decreasing in size too with faster changeovers from one sign to the other. This is even more evident in figure 33 for 50° incidence. In this figure the 'regular' states can be seen, which are the same for both noses and exist as either hand (discussed in section 4.1.1). Clearly at the lower incidences the 'regular' state is not apparent.

Figure 34 shows the variation of $C_{y_{max_2}}$ against roll angle at 50° incidence. It has a very similar form to figure 33 but the signs of all the points are reversed and their magnitudes have decreased. Otherwise the roll angle variations shown are basically the same with 'regular' states and rapid crossover regions between opposite hands. This behaviour is also seen at 60° incidence in figure 35. Results at 65° incidence were only obtained for the old nose and these also showed a tendency toward a 'square wave' type variation (see in figure 37). Above this incidence the position of $C_{y_{max_2}}$ is moving on to the nose too and cannot be measured and only a few results were obtained, and above 70° the side forces die away quite rapidly.

Hence it seems that a 'regular' state may exist at very high angles of incidence, 50° and greater, and also it becomes increasingly difficult to sustain intermediate states with lower side force values. This 'regular' state is independent of model minor geometric imperfections (which probably determine the hand of the state) but depends upon the nose profile. At lower incidences below 50° the minor model geometry plays a greater role in determining the state of flow. The more imperfect old nose tends to produce higher side forces than the better finished new nose even though both have the same basic nose profile, a three calibre ogive, and the 'regular' state notion no longer applies.

It is of interest to see how the roll angle variation on each nose varies with incidence. Consider first the old nose. Figure 36 shows how $C_{y_{max_1}}$ varies with roll angle for the incidence range 30° to 50° . The variation with roll angle is basically very similar throughout this range, but becoming more of a 'square wave' type as the incidence increases. Results from 50° to 65° incidence are shown in figure 37 which plots $C_{y_{max_2}}$ against roll angle. It can be seen here that the variation with roll angle remains very much the same as was found at 50° in figure 36, but with the signs reversed of course. At all incidences the side forces at any given roll angle are of the same 'hand' (i.e. the first shed vortex developing on the same side of the body) and the crossover points between hands occur at about the same roll angle positions (as near as can be determined).

Now consider the results with the new nose. Here the situation is a little different, similar in nature but with significant exceptions. Broadly, the type of pattern is the same with the flow producing steady side forces which change in direction as the model is rolled, producing the mirror image states of opposite hands for significantly large roll angle ranges. As for the old nose, as the incidence increases to 50° , shown in figure 38, the pattern tends to become more of a 'square wave' type, with the crossover range reducing, and above 50° , shown in figure 39, the flow is more of the type with 'regular' states of either hand. However, there are certain points which need commenting on. At a roll angle of 30° the sign of the side force at an incidence of 50° differs to that at the other incidences. This particular test was performed earlier in the test programme than those at the other

incidences and unfortunately a section of model had to be replaced before these other tests were made. (The section that had to be changed, due to accidental damage, was the first, upstream component of the measurement section. It was found that generally this had little effect on the subsequent measurements. It did however result in the cylindrical part of the model being turned through about 170° roll relative to the nose, due to the screw thread connections. Roll angle in the tests was always relative to the nose section as it had been established earlier that this was of overriding importance.) Previously some tests had been performed where the nose could be rotated independently of the body (section 4.1.2) and it was found in these tests (at 50° incidence) that for the nose rolled to an angle of 30° and the body kept at 0° roll the side force distribution produced was a mirror image of the corresponding case where the whole model was at 30° roll. This would give a result agreeing with the later tests at the other incidences. (This was the only case where rolling the nose produced a different result of opposite sign when compared with rolling of the whole model.) It can also be seen in figure 7 (which has better resolution than figure 38) that for the new nose at 50° incidence the sign of $C_{y_{max}}$ changes between roll angles of 30° and 40° . Hence any small misalignment in roll angle could be enough to produce a result of opposite hand, and then the curves in figures 38 and 39 would all be in agreement at this 30° roll angle.

The general form of the dependency on roll angle is similar at the incidences below 50° shown in figure 38 with the 'hand' of the side forces being the same at given roll angles and the changeovers from one hand to the other occurring at approximately the same roll angles. This agrees with the observations made with the old nose throughout the incidence range. However, the behaviour at 60° incidence shows several changes as seen in figure 39. Firstly, at 240° roll the side force changes sign. This was found to happen at 50° incidence also, but at a roll angle of 260° and can be seen in figure 7 which has results for every 10° of roll. Secondly, the position of the changeover in sign that occurred near 125° roll at lower incidences, figure 38, takes place at about 105° roll at this incidence. Likewise for the changeover near 195° roll at lower incidences which occurs at approximately 170° roll for this case. Thirdly, however, the other changeover points are positioned at the same roll angles as for the lower incidences.

It is worth looking more closely at the differences mentioned secondly above. It can be seen for 50° incidence in figure 7 that near the region of 110° - 120° roll angle the behaviour is somewhat unpredictable with three changes of sign within 20° . At the higher incidence of 60° (figure 39) the flow produces a negative hand to the side force distribution at a roll angle of 120° whilst at the lower incidence of 40° (figure 38) it is positive. At 50° incidence both these changeover points are found in figure 7, with a reversal between which may not be occurring at the other incidences, or is not found in the resolution of figures 38 and 39. The other point mentioned secondly above concerned the shift in position of a changeover point at 60° incidence. In figures 38 and 39 it can be seen that at 50° incidence there is a changeover in

sign at about 193° roll. However figure 7, which has better resolution in roll, indicates that it is at about 186° roll angle. Likewise it can be seen in figure 7 that the change in sign is very rapid. If figure 9 were re-drawn bearing this in mind then the changeover which is shown occurring at 169° roll angle for 60° incidence would be shifted to nearer 176° roll. Hence the difference in position of changeover between 50° and 60° incidence which was first observed as being about 25° of roll is in fact probably nearer only 10° .

All these points discussed above show that the apparently large differences between the roll behaviour at 50° and 60° incidence as shown in figure 39 are probably not so large after all and the true roll behaviour would be more like that shown in figure 40.

The cause of the differences cannot be attributed to the fact that part of the model body was changed because the data at 30° , 40° and 60° incidence were all obtained during the same test series (whereas most of the data at 50° incidence was obtained in earlier tests). It is more likely that the cause is related to the three dimensional nature of the flow. It has been postulated that the flow develops asymmetrically, giving rise to side forces, because of its unstable nature. Small imperfections on the model nose can cause enough disturbance to trigger the hand of the flow one way or the other. Now, as the incidence increases so the resulting flow pattern becomes more compressed toward the front of the model. Likewise the region in which nose geometry imperfections can have a triggering effect will diminish in size. On the old nose there are significant blemishes in the tip region which could well be causing the triggering and are of sufficient size to have an effect throughout the incidence range where stable asymmetric vortices are first developed. However the new nose has a better finish, although by no means perfect, and it is likely that the geometry imperfections which cause triggering in one direction at a low incidence are not of sufficient size, or are in the wrong position, to have an effect at the higher incidences. Likewise imperfections which may cause triggering in the opposite direction at higher incidences may not cause it at lower incidences. As the model is rolled either of these imperfections may be brought into what is the critical region, or rolled out of it, at an earlier or later stage depending upon the size and position of the imperfection and the incidence angle. This probably accounts for the small changes in roll angle dependency as the incidence increases, seen particularly with the new nose.

Basically the behaviour with roll angle remained essentially the same throughout the incidence range for each of the three calibre ogive noses. Hence the method chosen for performing later less extensive tests on other nose shapes (see section 4.2).

4.1.4 Correlation of Results

It has been shown that changing the model roll angle causes the flow to vary continuously between two 'hands' of a mirror image state which gives the maximum local side forces, and it is possible to achieve any value of local side force between these states, with a steady flow pattern. However, it can be seen in figures 5, 6 and 18 to 31 that as the value of $C_{y_{max_1}}$ decreases so its position moves further aft on the body. It would appear that the flow is stretching out down the body. This effect has been correlated in figures 41 to 47. The value of $C_{y_{max_1}}$ has been plotted against the position on the body where it occurs in figures 41 and 42 for both three calibre ogive noses and for angles of incidence up to 50° . Above this incidence the position of $C_{y_{max_1}}$ was occurring ahead of the measurement section and hence could not be determined in these experiments. Likewise figures 43 and 44 show the correlation between the value of $C_{y_{max_1}}$ and the position of the node point of the side force distribution x_o/d . These figures suggest that there are families of curves which describe the possible state of the flow over the body.

At the higher incidences the value and position of $C_{y_{max_2}}$ were used as parameters and their correlations are shown in figures 45 to 47. These do not show as good correlation as was found with the first half cycle of the distribution, so an alternative method was tried which also involved reconsideration of the node point position. Figure 48 shows plots of $C_{y_{max_1}}$ against the distance between the first maximum value and the node point of the side force distribution. Similarly figure 49 gives the correlation obtained for the variation of $C_{y_{max_2}}$ against the distance between the node point and the position of the second maximum value. It can be seen in both these figures that there is very little variation found in relative position of both the node and the second maximum position of the local side force even though the magnitudes of the side forces are varying throughout their range. Hence the original supposition that the whole distribution 'stretches out' with reduction in side force is not quite correct. The position of the first maximum value does change as in figures 41 and 42. At a fixed incidence, the greater the value of $C_{y_{max_1}}$ the nearer the front of the model it occurs. It cannot be determined from the available data whether this is due to a change in the position of the onset of asymmetry or whether the flow takes longer to produce a lower maximum value, but the spacing of the rest of the successive distribution remains fairly well constant relative to the position of the first peak. This might suggest that the development of the flow subsequent to the first peak develops by the same mechanisms irrespective of the preceding flow. These correlations could be used as the basis of an empirical prediction method.

4.1.5 Effect of Reynolds Number

A limited investigation of the effect of Reynolds number was performed using the old nose at zero degrees roll angle, which would correspond to one hand of a regular state. The Reynolds number, based on $l/\sin \alpha$, was varied

by changing the freestream velocity and the range of variation was limited by the available pressure transducers. Results were obtained at three incidences, 40° , 50° and 60° and at three Reynolds numbers for each. Additionally results were obtained for three other roll angles at 50° incidence only. The local side and normal force distributions are shown in figures 50 to 52. It can be seen that changing Reynolds number had little significant effect. As the flow would be expected to remain laminar (and the pressure distributions indicated that this was true), and the variation of Reynolds number was not very large, the results were not surprising. The only exceptions occurred at the highest incidences and highest speeds, which would be the most likely to show effects of transition. Certainly reducing the Reynolds number below 100,000 had no significant effect indicating laminar flow over the body at the Reynolds number used for the bulk of this investigation.

4.2 Other Nose Geometries

The results obtained using both of the three calibre ogive noses were used as a basis for developing a test technique to limit the amount of testing required for other nose geometries. It had been found with the old and new noses that rolling the model affected the results but that there were ranges of roll angle where the flow remained essentially unchanged. These ranges covered the roll angles which produced the maximum side forces and these forces could be of either mirror image 'hand'. (Most project designers would find the maximum side force case of greatest importance when designing real vehicles.) Additionally it was found that the behaviour was such that a roll angle in the centre of one of these ranges was likely to produce a maximum side force case for all incidences (see section 4.1.3).

A wool tuft grid had been constructed and used previously with the old and new noses to study the flow in the lee of the model (ref. 7). It was found that the flow was very steady, consisting of asymmetric vortices for most roll angles. Comparisons have been made between the measured pressures (and hence forces) and the observed flow patterns and it was relatively easy to see an agreement between them. The ranges of roll angle corresponding to a regular state of either hand could be readily determined by use of the wool tuft grid.

With these two established facts, above, a technique was developed and used for testing other nose geometries with a minimum of effort. Firstly the model was set to a moderately high incidence, usually 50° , and the wool tuft grid was set in position behind it. The tunnel was then run and the grid was observed as the model was rolled through the full 360° . In this manner the nature of the flow could be seen and the ranges corresponding to regular states noted. The tunnel was then stopped and the grid removed. Tests were then performed in the normal way (section 3) with a roll traverse in 30° steps at the one moderately high incidence. Some feel of the roll angle behaviour could be obtained by inspection of the readings from the pressure transducers but the final results could not be obtained without the use of a computer, which was not readily available. However, by also using the observations made

with the wool tuft grid two roll angles were chosen which should give the maximum side forces, one for each 'hand'. Incidence traverses, in 10° steps, were then carried out for each of these roll angles, from 30° to 70° incidence usually. In this manner it was hoped that a reasonable amount of information could be gained without spending undue time on non-essential cases.

4.2.1 Effect of Nose Blunting

The above technique was used to investigate the effect of hemispherically blunting the tip of the old nose. Two bluntness ratios were chosen, 5% and 20%, and were applied to the old nose section in turn. The bluntness ratio is defined as the radius of the applied blunting divided by the radius of the cylindrical body section. These two bluntnesses reduced the overall nose length by 0.053 calibres and 0.224 calibres respectively.

In both cases the wool tuft grid was used, and roll angle traverse performed, at 50° incidence. The tuft grid showed generally the same type of steady flow as was seen with the pointed noses and the roll angles to be used for the incidence traverses were chosen. The local side force coefficient distributions obtained for the 12 roll angles at 50° incidence are shown in figure 53 for the 5% blunted nose and in figure 54 for the 20% blunted case. It is immediately obvious from these figures that the increased blunting produces generally lower side forces. Values of $C_{y\max_1}$ have been extracted from these figures and are plotted against roll angle in figure 55 which also includes values obtained with the original pointed old nose. It can be seen in this figure that the small degree of blunting, 5%, had some effect on both the roll angle variation and the magnitude of $C_{y\max_1}$. The 20% blunting produced a significant change in roll angle variation, with only one 'cycle' per revolution compared with two 'cycles' for the other nose shapes. This is not significant in itself except that it is the geometry in the region of the nose tip which has been altered to produce the different roll angle behaviour and this is more evidence of the importance of the nose tip in influencing the flow over the body.

This figure also shows that increasing bluntness over the range covered reduces the maximum side forces on the body. Note that if the tests had been at just one roll angle, say zero degrees roll, then this conclusion might well have been different. At this roll angle reducing the bluntness from sharp (0%) to 5% shows a change of sign and reduction in magnitude of $C_{y\max_1}$ and then increasing the bluntness to 20% shows an increase in $C_{y\max_1}$. This type of behaviour can contribute towards the discrepancies reported in available published data on blunting effects. It is only by considering the roll angle behaviour that the true picture emerges.

The two roll angles chosen by the wool tuft grid technique for the 5% blunted nose were 60° and 240° , and for the 20% blunted nose 0° and 90° were chosen. Figure 55 confirms that these correspond to opposite hands of the

case with maximum side forces. For comparison, in subsequent figures results are shown for the original old nose without blunting at 0° and 90° roll angle, which also correspond to regular states.

Local side force coefficient distributions are shown in figures 56 and 57 for incidence angles of 40° , 50° , 60° and 70° . At the lowest incidence tested, 30° , the two blunted noses produced no significant side forces and so the results are not shown. Note in the two figures that the measuring stations change position relative to the nose tip because the blunting reduces the nose length. Figure 56 shows that at 40° and 50° incidence all the noses produced side forces with the greater peak values occurring further forward on the body, as was observed for different cases with the sharp nose when the model was rolled at a fixed incidence. The curves for the results at 60° and 70° incidence, in figure 57, have each been split into two sets. Each set corresponds to one 'hand' of the flow, so at 60° incidence one 'hand' for the 20% blunted nose produced no side force whereas the other hand did. This second hand shows that the distribution has shifted down the body relative to the distributions with the other two noses. In fact the 5% blunted nose results shows a small rearward shift relative to the sharp nose too. At 70° incidence the differences between the sharp and 5% blunted nose distributions are moderately small, but the 20% blunted case shows similar differences to those observed at 60° incidence.

The various different states of the flow observed for the 12 roll angles at 50° incidence can be correlated for the blunted noses in much the same way as was done for the sharp noses. Figure 58 shows a plot of the magnitude of the peak in the first half-cycle of the local side force distribution against its position and also against the position of the node in the distribution. This is shown for both bluntness ratios and it can be seen that the various states of the flow fall into a family of curves for each nose.

The smallest nose blunting, 5%, had quite a large effect at the lower incidences, below 50° , but its effect became much reduced as the incidence angle was increased. The greater blunting, 20%, which is still moderately small, had significant effects on the side force distribution as well as the peak local side forces developed on the model throughout the incidence range. This modification of distribution could lead to the situation where a particular configuration of given length could have a greater overall side force with the blunted nose than with the sharp nose. For instance at 60° incidence the upper set of curves in figure 57 shows that for a model length of about five calibres (and ignoring base effects) the sharp nose produces two half-cycles in the side force distribution (one on the nose section) which are of opposite sign producing a diminished overall side force, but high yawing moment. The 20% blunted nose result in the same figure shows just over one half-cycle in the side force distribution over the same length which could lead to a greater overall side force than for the sharp nose, but also with a smaller yawing moment. However, in general, nose blunting reduces side forces.

4.2.2 Effect of Nose Length

A brief investigation into the effect of nose length on the local force distributions was performed by using the test technique outlined in section 4.2 on a two calibre ogive and a one calibre ogive nose. These were nose sections which were used originally by Lamont and Hunt (ref. 3) and were manufactured out of aluminium alloy.

Provisionally it had been planned to perform the roll angle traverse at 50° incidence for both noses. However, in each case it was found that this was unsuitable and 60° had to be used. This was because the flow was found to be very unsteady behind the body as seen in the wool tuft grid. No discernible pattern of asymmetric vortices could be seen at all for any incidence except 60° and even then the flow was still quite unsteady. It resembled the flow behind a bluff body, rather than that seen with previous noses and consisting of tightly formed vortices surrounded by very steady flow. It was noticed as the tunnel was run up to speed that at low speeds the flow did adopt this type of pattern but very soon changed to the more random unsteady flapping. The subsequently measured pressure distributions were inspected to see if there were signs of transition of the boundary layer but it was found that the separation was laminar in all cases. It is not easy to decide from the pressure distributions if there is any turbulent reattachment after the initial separation when there is any vortex structure in the flow as this will be causing changes in the pressures on the body. But even in the cases where the flow was very unsteady with no time-average side forces the pressure distributions showed no sign of any reattachment. Of course, if it was a time-dependent occurrence then the measurements could not show it up.

Having performed the wool tuft study at 60° incidence two roll angles were chosen for each nose which would be used for the incidence traverses. The roll angle traverse was performed in the usual manner at 60° incidence and the local side force coefficient distributions obtained are shown in figure 53 for both of the noses. This figure shows that the side forces are of a similar nature for both of them. In each case the magnitudes are low and also it is the first half-cycle of the distribution. The peak values for both occur around $x/D \approx 3\frac{1}{2}$ and the node points at approximately $x/D \approx 5\frac{1}{2}$. The longer three calibre ogive noses showed much larger side forces and earlier development of flow asymmetry (the second peak in the local side force distribution occurring at $x/D \approx 5$ and the node point at $x/D \approx 4$) at 60° incidence. The variation of $C_{y_{max_1}}$ with roll angle is plotted in figure 60 for both noses.

Results were also obtained at incidences of 30° , 40° , 50° and 70° for both noses and generally these showed very low levels of side force, even though the roll angles were chosen to give the maximum values. This had been expected after using the wool tuft grid and seeing the unsteady flow.

Figures 61 and 62 show the effect of reducing the nose length (but maintaining an ogival profile) on the local side force distributions at incidences of 40° , 50° , 60° and 70° , for cases giving maximum side forces of each hand. The roll angles chosen were 0° and 90° for the 3 calibre, 240° and 330° for the 2 calibre and 180° and 300° for the 1 calibre nose. The difference between the longest nose and the other two is very pronounced at all incidences except at 70° where the 2 calibre nose does approach the type of distribution seen with the 3 calibre nose. It is quite likely that the flow over ogive noses has similarities in certain respects to the flow over cones and it is known that for cones the incidence angle required for separated flow is related to the nose semi-apex angle. If this is true for ogives too then the higher the incidence angle the shorter the nose length required for separated flow. The semi-apex angles are 18.9° , 23.1° and 53.1° for the 3, 2 and 1 calibre ogive noses respectively so if the 2 calibre nose starts to behave similarly to the 3 calibre ogive only at incidences somewhere between 60° and 70° then it is unlikely that the 1 calibre ogive nose ever will.

Hemispherically blunting the tip of the three calibre ogive nose produced a decrease in side forces. So too did blunting the nose by reducing its length (but maintaining the ogival profile), but in this latter case the flow also became much more disturbed showing very little sign of having any vortex structure developing in the lee of the body. It was not established whether sufficient hemispherical blunting would ultimately lead to such unsteady flows too.

4.2.3 Two Calibre Conical Nose

Tests were carried out using a 2 calibre conical nose on the model in the manner described in section 4.2. This nose section was also one originally used by Lamont and Hunt (ref. 3) and made of aluminium alloy.

No difficulties were experienced using the wool tuft grid with the model at 50° incidence and the patterns in the grid illustrated a flow very similar to that observed with the three calibre ogive noses (ref. 7). The patterns showed a very steady flow with asymmetric vortices, and as the model was rolled they would change 'hands' at fixed roll positions. The changeover was fairly rapid at this incidence. It was quite easy to choose two roll angles which would be expected to give maximum side forces throughout the incidence range.

The roll angle traverse was performed at 50° incidence taking readings at 30° roll intervals. The local side force coefficient distributions are shown in figure 63, and the variation with roll angle of the first peak in the distributions is shown in figure 64. These measurements confirm the findings with the wool tuft grid, that there is a regular state for the flow, of either hand, and that the crossovers between the two are fairly rapid. It is interesting to note that the regular state with this two calibre cone nose

produced a magnitude of $C_{y_{max_1}}$ slightly greater than that obtained using a three calibre ogive nose (see figure 7) at the same incidence.

The two roll angles chosen for the incidence traverse were 30° and 300° , and figure 64 shows that they correspond to opposite hands of the regular state. Results were obtained for these roll angles at incidences from 30° to 70° in 10° steps and the local force distributions are presented in figures 65 to 67. It can be seen that at 30° incidence the flow has started to develop asymmetrically as was found for the three calibre ogive noses. The curves for incidences less than 50° also show that the regular state is probably not well defined, though more evidence is really needed. However, at incidences of 50° and above the side force results from the two roll angles appear as mirror images and would suggest that the regular state is probably well defined. Again, more evidence is needed to be certain of this, but generally the results are very similar to those found using a three calibre ogive nose. Using these longest ogive noses it was found that the flow at any given incidence tended to produce a family of possible states, depending upon the roll angle, but the states correlated very well. Figure 67 shows such a correlation obtained for the two calibre conical nose at 50° incidence. The magnitude of peak side force coefficient is plotted against its position, and also is plotted against the position of the node point in the distribution. It can be seen that the two plots produce curves on which all the results fit, indicating that the various different states of the flow with this nose also belong to the same family, at least as far as the node point.

4.3 Normal Force

In all the tests performed the measured pressures were numerically integrated to produce values of the local side coefficient at each station and also the local normal force coefficient. In many of the figures produced for this report the normal force distribution has been omitted to prevent overcrowding of the figures. However, these distributions have been studied and do appear in some of the figures.

It is noticeable in all cases where the flow develops asymmetrically over the model that the normal force distribution shows variations along the model length, dependent upon the vortex structure of the flow. However, it has not been possible to find any distinct pattern to these variations or to relate the normal force variation precisely to the side force variation or vortex development. Certain trends have emerged though.

Whenever there is a strong, steady asymmetric vortex structure in the lee of the model the normal force tends to be relatively large, due to the high flow velocities, associated with these strong vortices, which cause pressure reductions over the back of the body. Similarly, when the flow is not asymmetric the normal force reduces, as found at high incidence in two ways. The model could be at a roll orientation that produces only low side

forces, even though at a moderately high incidence angle as seen in figure 8, or the steady asymmetric pattern obtained in the region of the nose and forward part of the model may be dying away, as at stations far from the nose at fairly high incidences and shown in figure 4. In this latter case the flow very far from the nose develops into the Von Karman vortex street type of flow found on infinite yawed cylinders in uniform freestreams producing time-dependent vortex shedding. The mean crossflow drag coefficient for such a flow with laminar separation is approximately 1.1-1.2, and the normal force coefficient found far from the nose in these tests generally tended to approach this value (the results at 90° incidence usually produced values of about the same magnitude). Generally, of course, at low incidences the side forces were steady and low or non-existent, and at very high incidences the side forces were also low or non-existent, and the flow unsteady. In both cases the normal forces were low.

The main observation of normal force must be that at all incidences which produce asymmetric flow the overall normal force will be a function of roll angle just as the side force is.

5. FLOW VISUALISATION TESTS

During the course of this investigation two methods of flow visualisation have been used. The first method involved using a wool tuft grid placed in the lee of the model to study the development of the body vortices. This technique was found to be useful in subsequent testing as discussed in section 4.2, and has been fully documented in refs 7 and 8. However, the grid can only be used to show large features of the flow behind the body and of course will be having some influence on the flow.

In order to study the flow close to the body it was decided to use the oil surface flow visualisation technique and to monitor pressures on the body simultaneously. It has been shown that the flow on the body can be changed by small geometric changes, especially on the nose tip, and it was feared that introducing oil on to the model surface might similarly upset the flow. Obviously it would be pointless to perform the experiments without knowing whether the flow had been affected or not which is why surface pressures on the body were monitored during the tests.

The model used for these tests consisted of a support body with two sections ahead of it which were used for measuring time-dependent pressures in the earliest investigations of this test programme. Ahead of these was the nose rotator section shown in figure 13 which allowed the nose section, fitted ahead of it, to be rolled independently of the rest of the model. Two pressure tappings were used for monitoring body pressures. These were situated at $\pm 75^\circ$ to the body freestream generator, see figure 68, at a station 4.5 calibres back from the nose tip. The difference between the two pressures is strongly related to the side force at that station, which at the 50° incidence of the tests is usually quite high, see figure 68. Two matched pressure transducers were mounted inside the model and connected by short tubes (for high frequency response), one to each of the pressure tappings. Their difference was taken electrically and was recorded on a u/v recorder. The other 30 pressure tappings on the model were blanked off from inside to prevent any flow through them and it was found in the course of the testing that, as expected, they did not appear to affect the flow.

The test technique used was to set up the model with the pressure measurement section aligned correctly and to choose the nose roll angle for the test. The roll angle of the nose was changed independently of the body for these tests which made the setting-up easier, and it has already been shown in section 4.1.2 that the nose roll angle is of overriding importance in determining the flow over the body. The tunnel was run up to speed without any oil on the model and recordings made of the pressure difference ΔC_p . The tunnel was then run down and the oil mixture applied to the model. Finally the tunnel was again run up to speed and recordings made of ΔC_p as the pattern developed and lastly when it was dried off. If the recorded traces were all the same then it was probable that the flow with the oil on

the model was the same as that without it, at least up to the stations where the pressure tappings were situated.

The oil mixture consisted of paraffin with day-glo powder mixed in and a tiny drop of oleic acid which helps to prevent globules forming. It was applied to the model by brush over the whole of the surface except for a patch just ahead of the pressure tappings. The region from about $x/D = 3\frac{1}{2}$ to $x/D = 4\frac{3}{4}$ and between $\theta \approx \pm 80^\circ$ was left clear of oil so that none would be able to flow into the tappings. This meant that the flow in this region could not be visualised but it is obvious from the results that it is merely attached flow travelling around the body until it reaches the primary separation line and is of no significant importance. The model was mounted in the wind tunnel such that the incidence plane was horizontal. This meant that the oil tended to flow across the model as it was applied and could dry out too soon. The time between applying the mixture and running the tunnel up to test speed was kept to a minimum but in some of the results it is possible to detect brush marks, etc. where the oil had dried out. However this was not a major problem, nor was the effect of gravity during the test, as had at first been feared. In some tests the oil tended to collect into certain regions which took a long time to dry (up to about 45 minutes with the tunnel on). As this oil protruded out into the flow slightly it was washed away a little from its original collection point, and this can be seen in the results but again was not a major problem.

The oil patterns developed on the body were recorded photographically. Day-glo powder fluoresces under ultra-violet illumination so the wind tunnel was blacked-out and a single u/v lamp shone on to the model. A camera fitted with a u/v filter (to let through visible light but block off ultra-violet light) was used to photograph the flow patterns on the model from four viewpoints. The camera was tripod-mounted for the very long exposures used and the model was rolled through 90° for each of the four shots, which comprised views from the model rear (leeward), top (port), front (windward) and bottom (starboard as mounted in the tunnel).

In each test case the front view showed the oncoming freestream impinging on the model and flowing around it up to the separation lines, and little else. These are not very significant and are not presented in this report.

Three test cases were chosen, all using the old three calibre ogive nose and all at 50° incidence. Two of the cases were chosen to correspond with the two hands of the regular case, for which 0° and 90° nose roll angle were used (see fig. 7). The third case was for a roll angle giving zero side force on the body, as near as could be found.

The testing for the first two cases was fairly straightforward and figures 69 and 70 show the u/v traces of the pressure difference ΔC_p that were obtained with and without the oil on the model. Notice that in each case the

natures of the traces are the same and that the mean value remains the same when the oil is put on the model. This indicates that the flow probably remains unaltered too. The mean values measured from these traces were $\Delta C_p \approx 2.23$ at 0° roll angle and -2.27 at 90° roll angle which correspond to approximately 2.37 and -2.35 respectively for the tests with the multi-pressure tapped model under similar conditions. This is a satisfactory agreement considering all the differences in the two experiments.

More difficulty was encountered with the third case. First the roll angle of the nose was adjusted until a position was found which gave a zero mean pressure difference ΔC_p with no oil on the model. This roll angle was found to be $\phi = 56^\circ$ (see figure 7). Next, oil was applied to the model as for the previous cases and the experiment performed. The resultant pressure trace was satisfactory but the oil pattern on the model had too many areas where brush marks showed so the test was repeated. Unfortunately it was no longer possible to obtain a satisfactory pressure trace after several attempts and eventually a compromise was necessary. Oil was applied over the model in the usual way except for the very front $\frac{1}{2}$ -calibre or so. The resulting experiment was then found to be satisfactory in all respects and figure 71 shows the pressure traces obtained. Note the zero mean value, and also the more disturbed nature of both traces than was found in the regular cases. This has been commented on in section 4.1.1. Before photographing the resulting pattern of this last test a small smear of oil was placed on the nose tip so that it would show up in the pictures.

The flow patterns found in these three tests are shown in figures 72, 73 and 74. In each figure the upper view shows the pattern on the top (port side) of the model, the middle view shows the pattern on the rear (leeward side) of the body and the lower view shows the underside (starboard) of the model. The most interesting views are those in the middle, or the rear of the model. The features of the flows can be traced directly across to the upper and lower views, but the middle view illustrates just how asymmetric the flow can be. Note how the results for the first two tests very closely mirror one another. In these the main flow features are the same, but changed side for side, so a discussion of one only is included, that in figure 72 at zero roll angle. An annotated line drawing of some main features is shown in figure 75 and reference will be made to the identified areas and lines in this figure.

Firstly in the flow over the nose there is clearly more than one separation line. The flow from the attachment line at the windward side of the model separates at the primary separation lines, A, and rolls into vortices one from each side. These vortices entrain flow which forms another attachment line on the leeward side of the model forming the herring bone pattern associated with such vortex flow, region B. The reversed flow of region B quickly separates at the secondary separation lines C and small secondary vortices are formed beneath them as shown in figure 76, top. These vortices

also have attachment and separation lines and 'herring bone' patterns are formed. There is a region of rather dead air between the secondary vortex separation lines and the primary separation lines (see figure 76). In this region the air which has flowed over the secondary vortex gets entrained into the air forming the primary vortex and although it has a circulatory motion it is not another true vortex formed out of viscous flow in boundary layers, but merely reverses its direction because that is the only way for it to go. It is not easy to make out all of this flow pattern from the figures, but it can be seen that the primary flow over the body, that before first separation and the two major vortices which dominate the flow, leaves a large area at the side and rear of the body where there are secondary flows and fairly dead regions. This is true along the whole body length. It can be seen at the end of the nose section, position D, that one of the first primary vortices is starting to separate from the upper part of body (as seen in the figures) and the remaining vortex is moving across the back of the body, as shown in figure 76 bottom, vortices 1 & 2. (The wool tuft grid flow visualisation also showed this upper vortex as the first to be shed).

In view of the complicated nature of the oil pattern, after the test was completed at 0° roll angle some attempt was made at flow visualisation using a single wool tuft mounted on a hand held probe. With the tunnel running the door was opened and the probe placed in the lee of the model. It was fairly easy to track vortices by observing the spinning of the wool tuft. Where possible the track of vortex cores was traced using the probe and figure 76 bottom shows the approximate positions of vortex cores before they are shed from the body. When the body boundary layer stops feeding the vortices they are shed from the body and move off in approximately the free-stream direction. Although this was not a precise method of observing the flow, with only a rough sketch as its result, it was invaluable in interpreting the oil flow pictures, and the bottom of figure 76 can be related in many instances to the flow pattern in figure 72.

There are some areas, E, F, G, H where oil patches were formed. This was particularly noticeable with E and F, much less so with G and H. It is not known why such areas as E and F should be formed, where the flow appears to be inward on all sides (note that as the oil built up it protruded into some external flow and got washed from its original position by a small margin - this can be seen in the figures). They are situated in regions where the flow is very weak, or dead and the pressures are very low. It seems that just aft of these points there must be some local flow on the body surface travelling forward towards the nose tip into the low pressure region. Area G may be formed as the result of the secondary vortex lying upstream of it becoming engulfed in the flow which forms the primary vortex on that side, but this is not certain.

Note from figure 76 that the primary vortex remaining attached after the first one to be shed (no.2 in the figure) moves laterally to sit very

much at the back of the body. Ultimately it too is shed, identifiably at about position J in figure 75 and vortex no.3 in figure 76 becomes the dominant one. It rapidly veers sharply across the body where vortex no.2 has left space and produces a complicated flow pattern on the body in region K (figure 75) involving fairly rapid flow velocities in an almost axial direction. It is not clear what happens to it then as it seemed to disappear and merge into the flow with the one below, but the flow pattern on the body here indicates that there is a vortex of the same sense present just aft of this position too. It is obviously a complicated flow but vortex no.3 was not detected being shed by the single wool tuft grid. Vortices nos.4 and 5 of figure 76 were detected, with no.4 being very much more to the side of the body.

At stations further downstream than this the flow is becoming increasingly time-dependent so the oil patterns will show only the mean flow, but it would appear that vortices 4 and 5 show some lateral movement before vortex no.5 is shed somewhere near region L. It is very likely that vortex 5 is connected with, or even the extension of, vortex 3 although the flow at their junction is very difficult to interpret. The overall flow pattern shows alternate shedding of vortices from each side, as found in pressure measurement tests.

This is a very broad interpretation of the flow patterns observed in the first two test cases, and much of the finer detail which perhaps needs explaining is difficult to analyse. This is partly because so much of the flow pattern on the body is not caused directly by the primary vortices present at any particular station but is the result of secondary flows and dead air regions. However, it is clear that the flow is very complicated, and although there are vortices shed from alternate sides of the body, as has been postulated many times and explains the phenomenon of side forces, the nature of each shedding is a little different. There seem to be secondary vortices playing a part in the shedding of the first vortex, which is developed from the nose and also has another strong primary vortex present in the flow. The second vortex has been developed from the nose and is shed very much from a position in the lee of the body. The third vortex then undergoes a complicated history probably developing into vortex number 5 before it too is shed in a position well downstream where it seems there are no secondary vortices. It appears that the conditions for vortex shedding are different in each case.

Also apparent is the fact that in some places the axial flow is halted, or even reversed, and in others there is a very strong axial flow. This means that flow surveys around the body which take into account only two velocity components (such as the crossflow plane), although providing very valuable information, do miss some important features.

The flow patterns found here on the body in figures 72 and 73 and the

vortex patterns causing them, as shown in figure 76, have been compared to the local side force coefficient distributions measured under similar conditions, see figure 5 and particularly figure 4. It has been found that there probably is some agreement between them. Comparing figure 5 with figures 72 and 76 it seems that the peak magnitudes in the local side force distributions occur slightly ahead of the probable vortex shedding locations, and the local side force is directed away from the side that sheds the vortex, as has been observed before with the wool tuft grid (ref.7).

The third case to be considered in these surface oil flow experiments is that in figure 74 for nominally symmetric flow. Certainly up to the pressure measuring station at $x/D = 4.5$ the recorded pressure traces of figure 71 indicated that the flow was symmetric. This is confirmed in the photographs of figure 74, which also show that at stations further downstream some asymmetry does develop, with a possible vortex shedding location near $x/D = 11$. However, the region of most interest in this case is over the front part of the model and the discussion will not concern the region aft of $x/D = 8$. In the regular cases discussed above (0° and 90° roll angle) asymmetry in the flow had developed well forward on the nose, whereas in this case the flow has remained symmetric. Unfortunately it was not possible to observe the flow pattern right up to the nose tip as the oil affected the flow. However, on the nose it can be seen that the separation lines are symmetrically disposed and the resulting flow is probably very like that shown in figure 77 (top) with symmetric primary vortices. The secondary vortices are also symmetric and appear to rapidly diminish in strength at stations downstream of the nose. The 'herring bone' pattern caused by the primary vortices can be observed well aft on the cylindrical body section, but those due to the secondary flow are not easily discernible much beyond the nose section. The surface flow on the body directly affected by the twin primary vortices increases further downstream and the separation lines caused by the secondary flow become much less distinct. The flow at a station near $x/D = 8$ would probably be as shown in figure 77 (bottom).

It was very noticeable in the regular cases (0° and 90° roll angle) that the angular positions of the primary separation lines varied considerably on each side of the body. In this third case the angular positions do not vary by very much, moving slightly forward in the crossflow plane as distance from the nose is increased, and remain symmetric. In none of the three cases was there any sign of transition in the flow ahead of the primary separation lines, or of separation bubbles. There appeared to be nothing in any of the surface patterns to suggest why the flow should become strongly asymmetric in two cases (of opposite hands) but not in the third.

6. CONCLUSIONS

An experimental investigation has been carried out to measure surface pressures on the cylindrical part of an axisymmetric nose-cylinder wind tunnel model with the aim of examining the causes of discrepancies in previously available data on side forces at high angles of incidence. The following main conclusions were drawn from this work.

There are three main flow regimes as incidence is varied from 0° to 90° . At low incidences, up to about 25° to 30° , the flow remains symmetric, even when separation occurs, and steady with no resultant side forces on the body. At very high incidences, above about 75° , the flow breaks down into unsteady von Karman periodic vortex shedding, also with no resultant mean side forces. It is with the region between these boundaries, from about 30° incidence to about 75° that most of this investigation has been concerned. In this region the flow over the body becomes asymmetric and the vortices formed from each side in the separated region in the lee of the body are shed from the body at different axial locations. After a vortex has been shed from one side of a body another starts to form from the same side. This gives rise to a cyclic side force distribution on the body with gradually decreasing magnitudes at stations further distant from the nose. The flow in the first half cycle or so is generally fairly steady but at distances far from the nose the flow behaves like that around an infinite yawed cylinder with periodic vortex shedding giving no resultant mean side forces. At moderate angles of incidence this flow pattern is spread out along the body length and as the incidence increases the pattern becomes more compressed towards the front of the body.

The asymmetric flow at a given incidence has been found to vary as the model has been rolled. However, the flow will remain steady and repeatable under the same given conditions. Using a model section which allows the nose and cylindrical body to roll independently it was shown convincingly that the roll orientation of the nose is of overriding importance (at fixed incidence) in deciding the flow state over the body.

The range of high incidence where side forces are developed can be subdivided into two parts based on the results found with two different nose sections with the same basic nose profile, a three calibre ogive.

At moderately high incidences, between about 30° and 50° , the flow is dependent upon the roll angle and varies slowly as the model is rolled, generally with peak side forces falling between the same positive and negative bound, which increases as incidence goes up. At high angles of incidence between about 50° and 70° the side forces on the model are dependent upon roll angle but there are large ranges where the flow hardly varies with roll, preferring a 'regular' state. This gives the largest side forces, and changes rapidly to the same state but of the opposite hand over small roll angle ranges at certain roll orientations. Generally these changeovers were found

at approximately the same roll positions throughout the 30° to 70° incidence range.

Any flow state between the opposite hands of the boundary state was found to be fairly steady, although states with low side forces become increasingly difficult to attain as incidence increases. Although the flow was found to vary in this manner analysis of local side force magnitudes and positions showed that all the states correlated very well. The lower the peak local side force the further aft on the body it occurred, hence also affecting the remainder of the side force distribution.

Evidence generally suggested that imperfections on the model nose, especially in the tip region, were of most importance in deciding the state of the flow. At only moderately high incidences it seems that these imperfections help to determine both the sign of the side forces and to some extent also play a part in deciding the magnitude. At high incidences they mainly determine only the sign of the side forces and it is the nose profile which determines the magnitude, as shown by the regular state for both three calibre ogive noses being the same at high incidences.

Further evidence of the importance of the tip region of the nose came when one of the noses had small amounts of hemispherical blunting applied to it. The first case, 5% blunting, produced a small reduction in the regular state side forces but also modified the roll angle behaviour. The second case, 20% blunting, considerably affected both the roll angle behaviour and the side force distribution causing a significant reduction in magnitude.

It was found using both a two calibre ogive and one calibre ogive nose that the flow over the model became very much less steady than had been found with the three calibre ogive and there appeared to be no organised vortex structure in the model wake. In both these cases the unsteadiness caused there to be virtually no measurable mean side forces developed at incidences below about 60° . At this incidence both developed low (and fairly similar) side force distributions. Above this the shorter nose again developed no side forces but the longer of the two began to develop distributions similar in form to those observed with the three calibre ogive noses. Results obtained using a two calibre conical nose were very similar in all respects to those found with the three calibre ogives, except producing slightly greater side force magnitudes. The flow with this nose was generally very steady with strong asymmetric vortices in the lee of the model.

Using the original three calibre ogive noses it was found that varying Reynolds number (by varying flow speed) produced very little effect. This was expected as the investigation was performed in the subcritical range and there was no influence of transitional flow. Consequently all the results obtained in this investigation have been repeatable. When the Reynolds number increases into the critical region transition can occur and repeatability becomes a major problem in tests of this sort.

Although mostly concerned with side forces some note was made of normal force during this investigation. It was found in general terms that the lower the side force (whether because of low incidence, model roll orientation or axial station far from the nose) the lower, too, the force. This means that in the incidence range 30° to 75° the normal force is a function of roll angle.

Some of the main reasons for discrepancies found in earlier data can be attributed to the following reasons:-

- a) poor wind tunnel flow quality,
- b) model vibrations, often found in force measurement tests where the model is mounted on a balance,
- c) the effect of roll angle, and
- d) performing tests in the critical Reynolds number range.

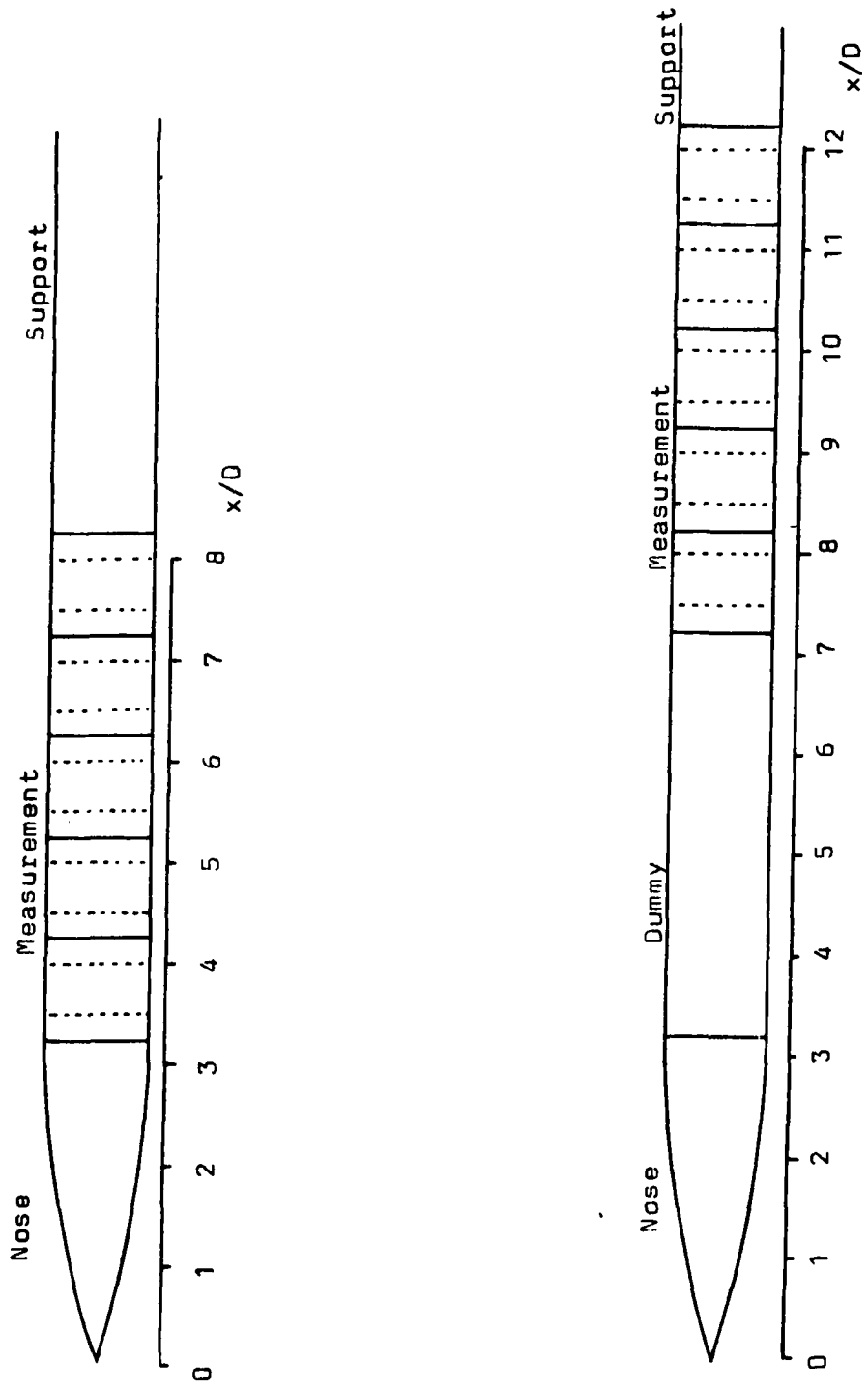
7. REFERENCES

1. Ericsson, L.E. Vortex-induced asymmetric loads in 2-D and 3-D flows.
Reding, J.P. AIAA Paper 80-0181 1980
2. Wardlaw, A.B. Induced side forces at high angles of attack.
Morrison, A.M. J. Spacecraft, Vol.13, no.10, 580-593 1976
3. Lamont, P.J. Pressure and force distributions on a sharp-nosed
Hunt, B.L. circular cylinder at large angles of inclination to
a uniform subsonic stream.
J. Fluid Mechanics, Vol.76, part 3, 519-559 1976
4. Lamont, P.J. Prediction of aerodynamic out-of-plane forces on
Hunt, B.L. ogive-nosed circular cylinders.
J. Spacecraft, Vol.14, No.1, 38-44 1977
5. Hunt, B.L. Pressures on a slender, axisymmetric body at high
Dexter, P.C. angle of attack in a very low turbulence level air
stream. First Annual Report.
Univ. of Bristol, Aero.Eng.Dept. BLH/7801 1978
6. Hunt, B.L. Pressures on a slender, axisymmetric body at high
Dexter, P.C. angle of attack in a very low turbulence level air
stream. Second Annual Report.
Univ. of Bristol, Aero.Eng.Dept. 1979
7. Dexter, P.C. Pressures on a slender, axisymmetric body at high
Flower, J.W. angle of attack in a very low turbulence level air
stream. Third Annual Report.
Univ. of Bristol, Aero.Eng.Dept. 1980
8. Dexter, P.C. The effects of roll angle on the flow over a slender
Hunt, B.L. body of revolution at high angles of attack.
AIAA Paper 81-0358 1981

8. NOTATION

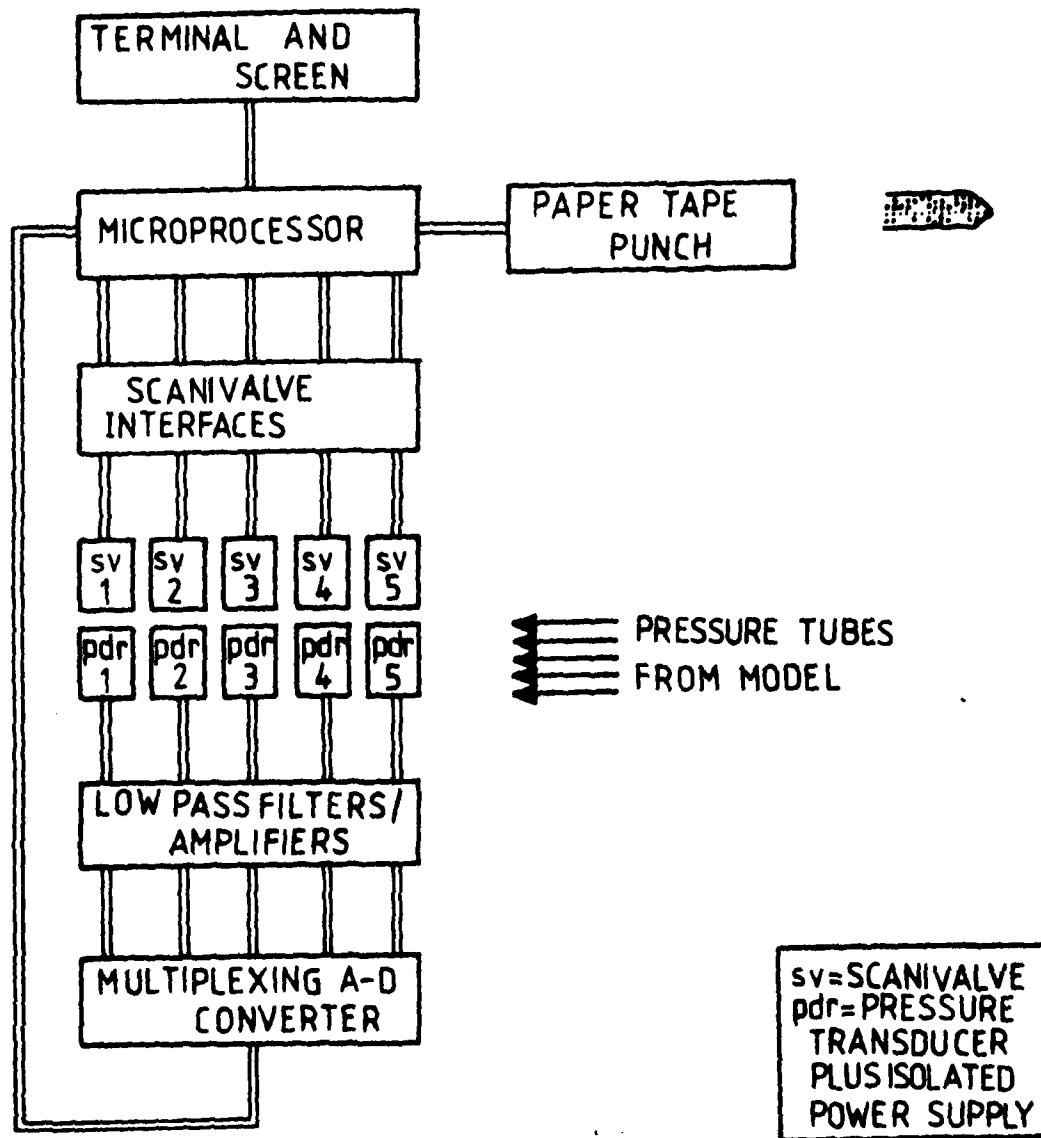
C_n	local normal force coefficient, local normal force/ $(q_x d)$
C_{p_x}	pressure coefficient, $(p - p_\infty)/q_x$
C_y	local side force coefficient, local side force/ $(q_x d)$
$C_{y_{max_1}}$	first peak value of C_y in side force distribution
$C_{y_{max_2}}$	second peak value of C_y in side force distribution
D	body diameter
p	pressure on body surface
P_∞	freestream static pressure
q_x	crossflow dynamic pressure, $\frac{1}{2}\rho V_x^2$
Re	Reynolds number, $(Vd)/(v \sin \alpha)$
V	freestream velocity
V_x	crossflow velocity, $V \sin \alpha$
x	axial distance from nose tip
x_{max_1}	axial distance of $C_{y_{max_1}}$ from nose tip
x_{max_2}	axial distance of $C_{y_{max_2}}$ from nose tip
x_o	axial distance of node point in side force distribution from nose tip
α	incidence angle, degrees
ΔC_p	difference in C_{p_x} between two points symmetrically disposed at $\theta = \pm 75^\circ$
θ	azimuth angle around body circumference from leading body generator, degrees
ϕ	roll angle, degrees

ϕ_{nose} roll angle of nose section of model, degrees
 ϕ_{body} roll angle of model excluding nose section, degrees
 ν kinematic viscosity



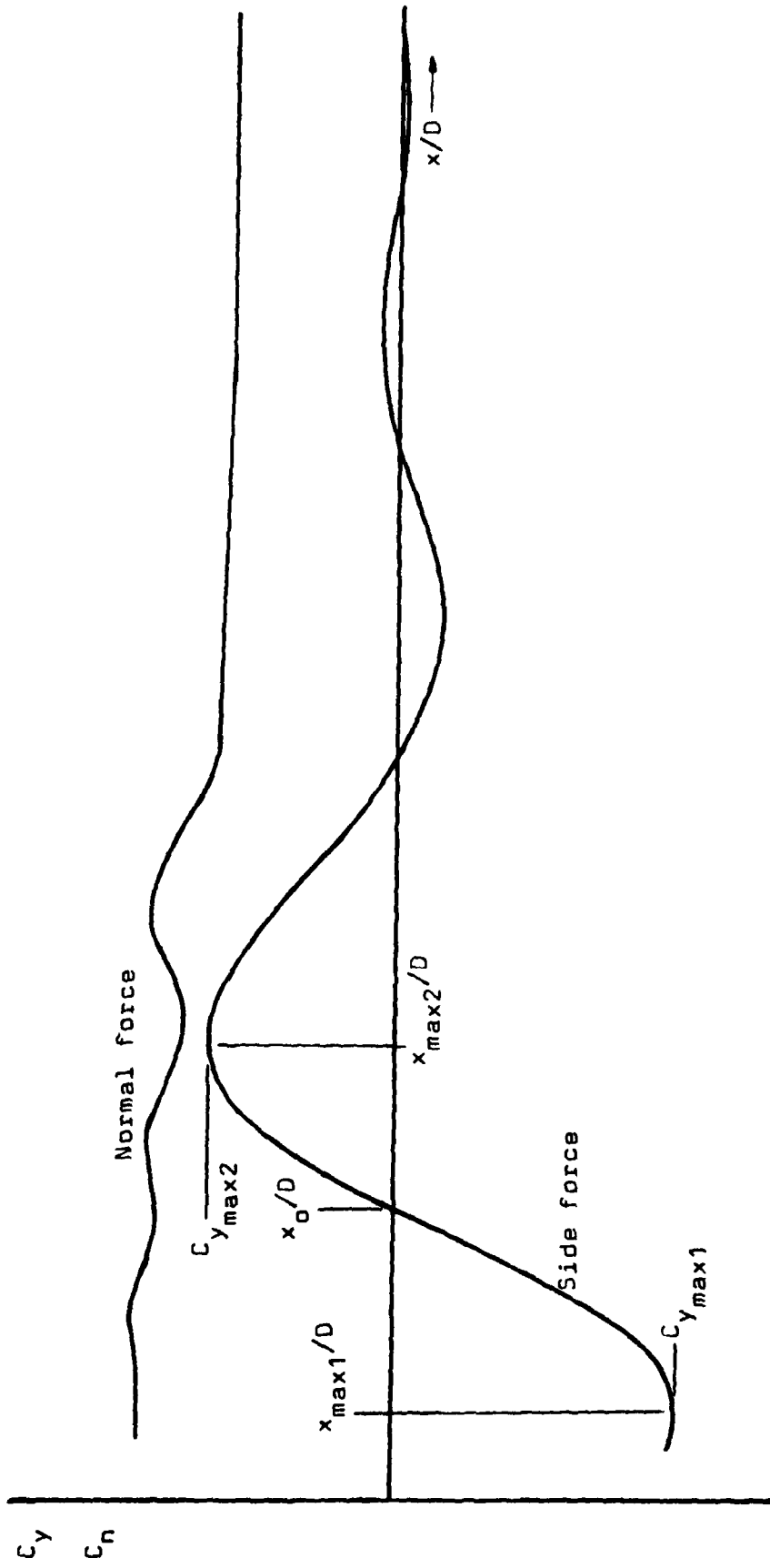
Multi-Pressure Tapped Model

Figure 1



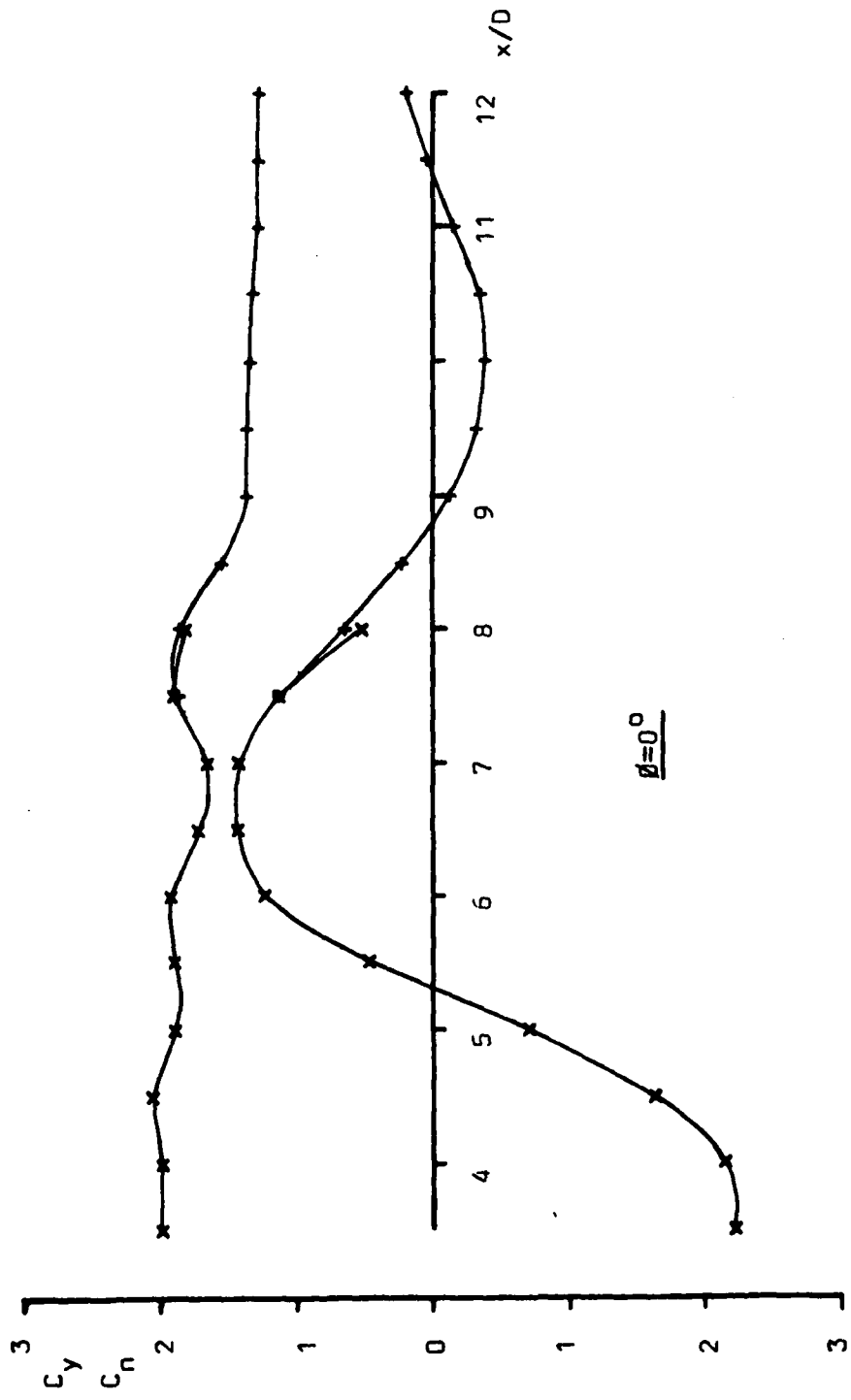
Diagrammatic Representation of the New Data Acquisition System.

Figure 2



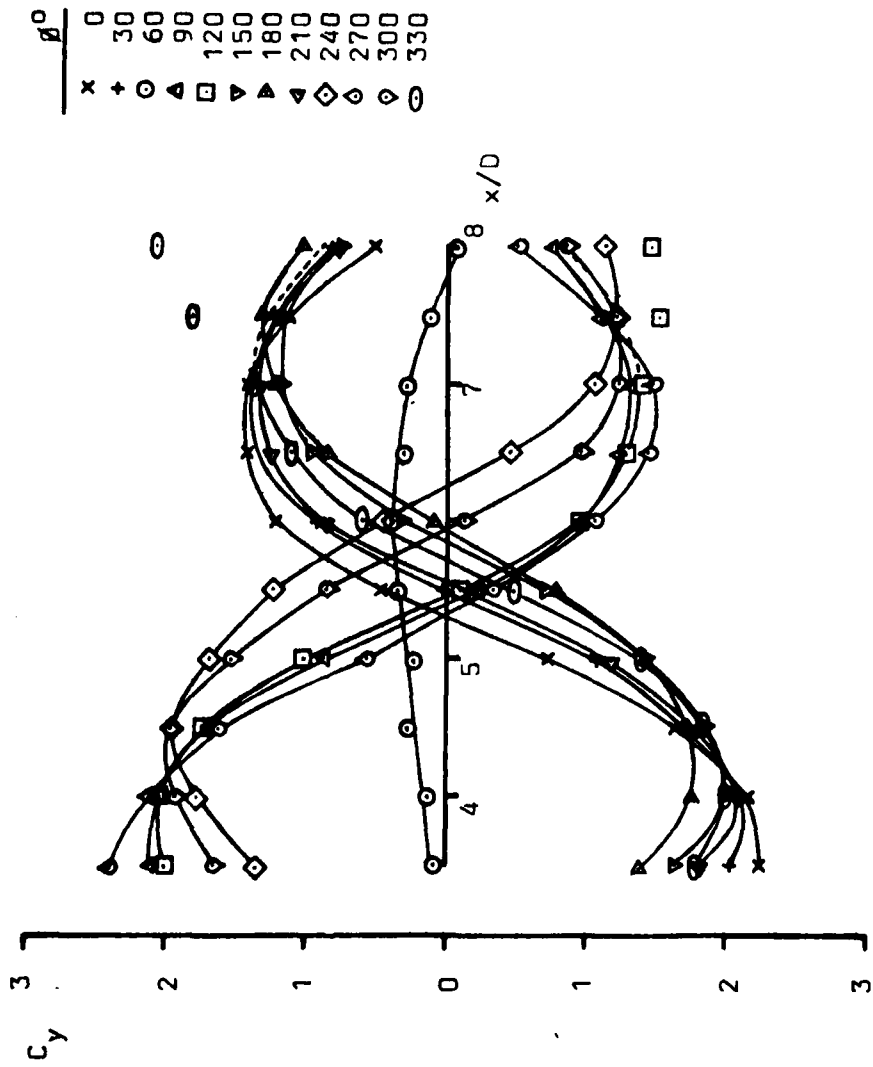
Typical Distribution of Local Force Coefficients

Figure 3



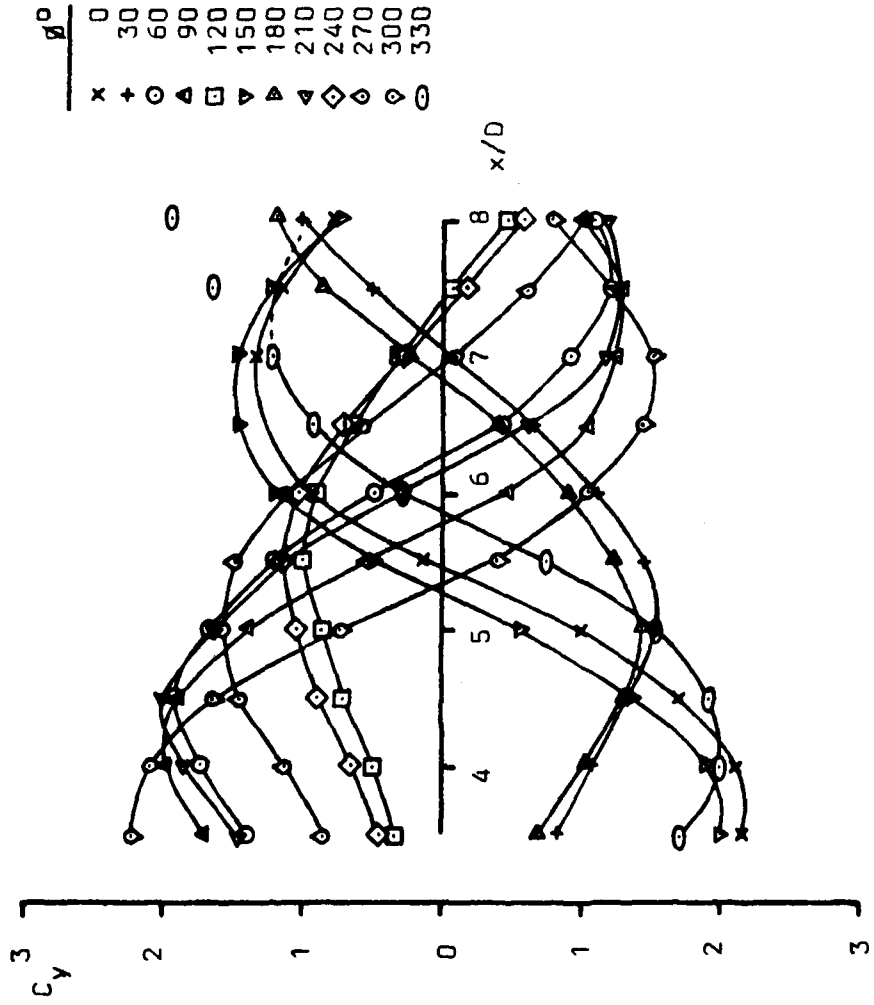
Distribution of Local Side and Normal Force Coefficients.
 Old Nose 50° Incidence Re=105

Figure 4



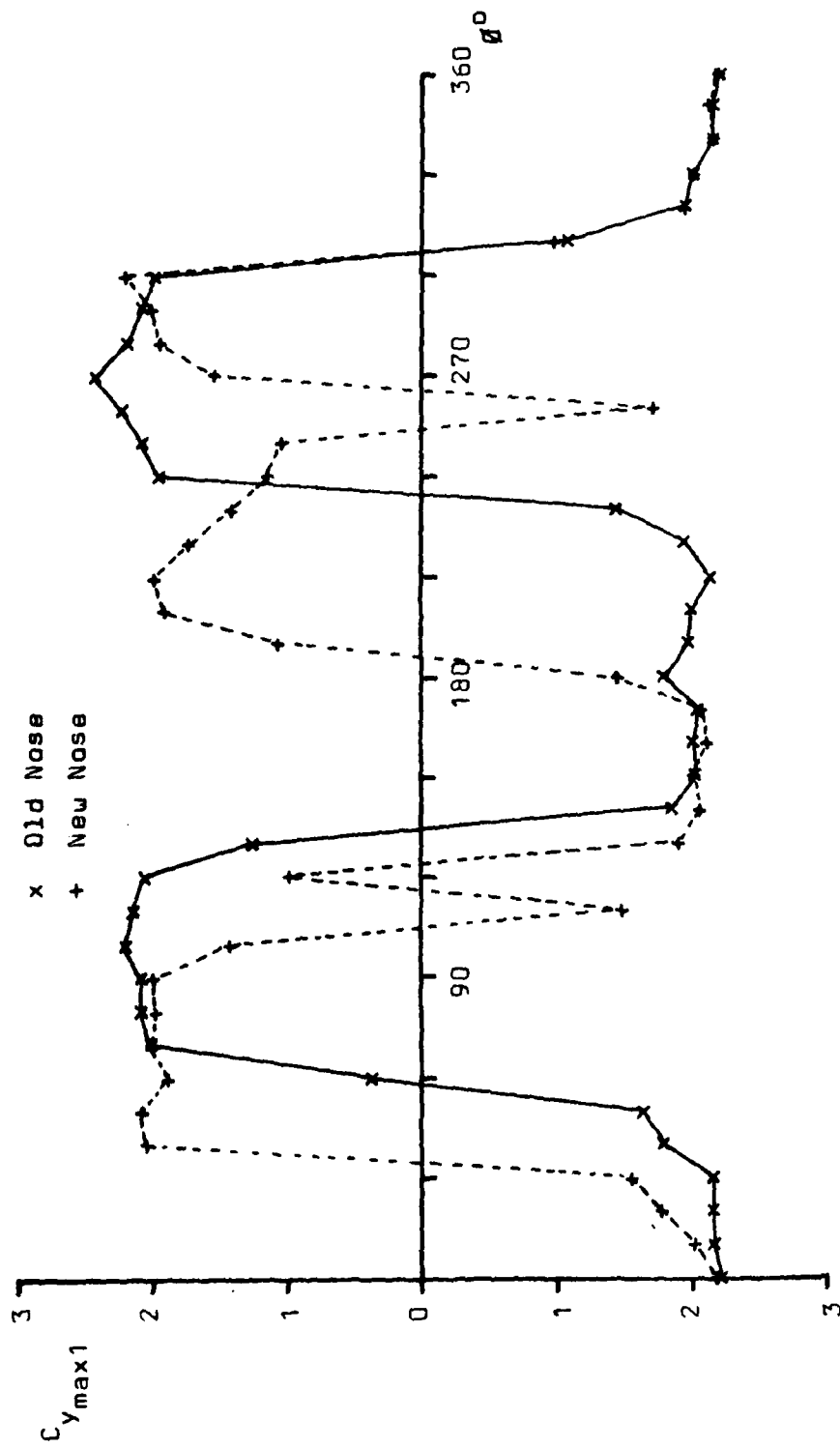
Distribution of Local Side Force Coefficient
 Old Nose 50° Incidence Re=10⁵

Figure 5



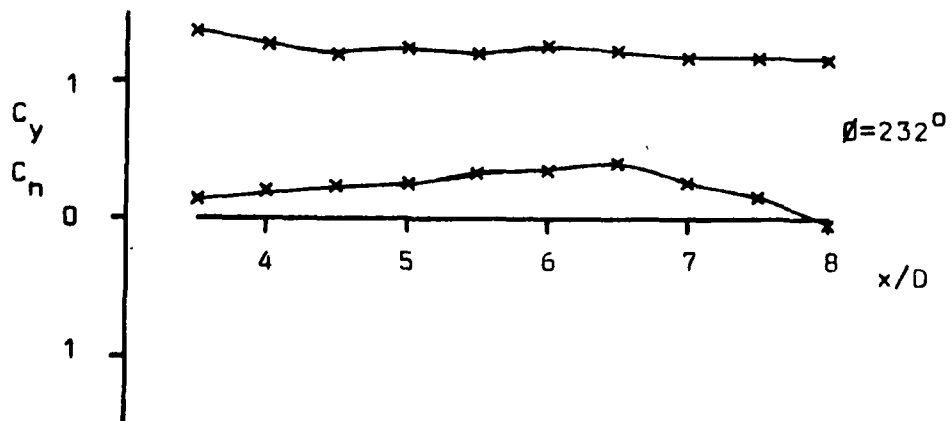
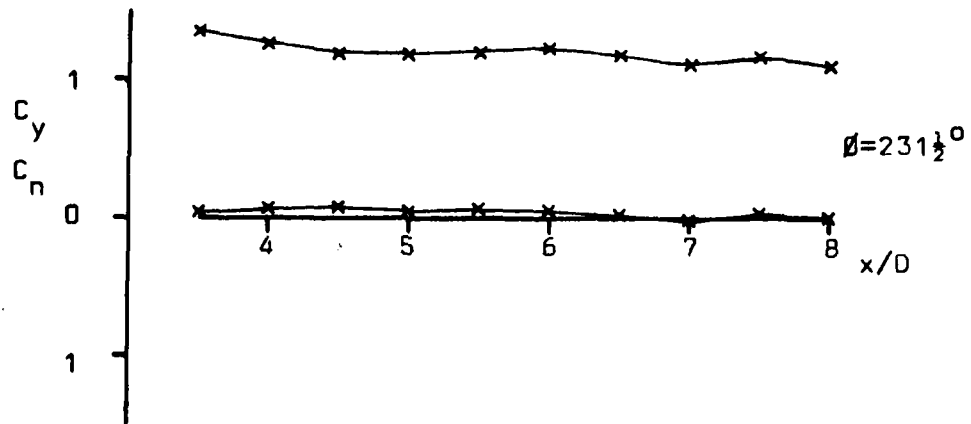
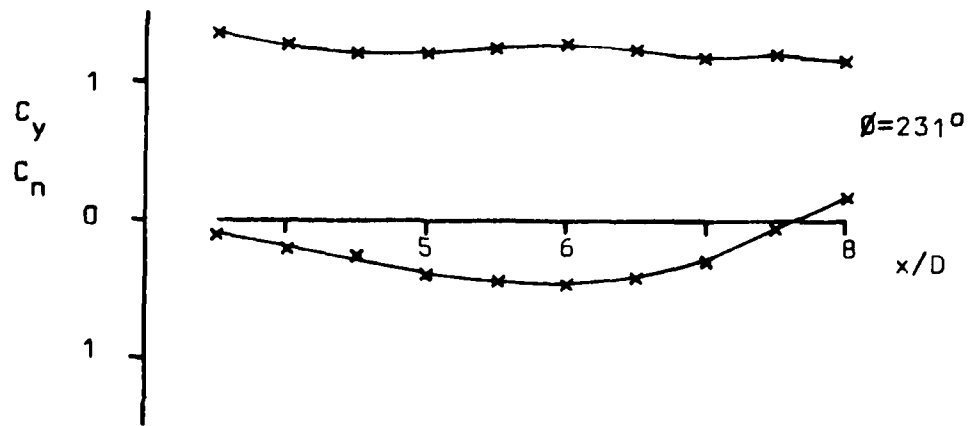
Distribution of Local Side Force Coefficient
 New Nose 50° Incidence $Re=10^5$

Figure 6



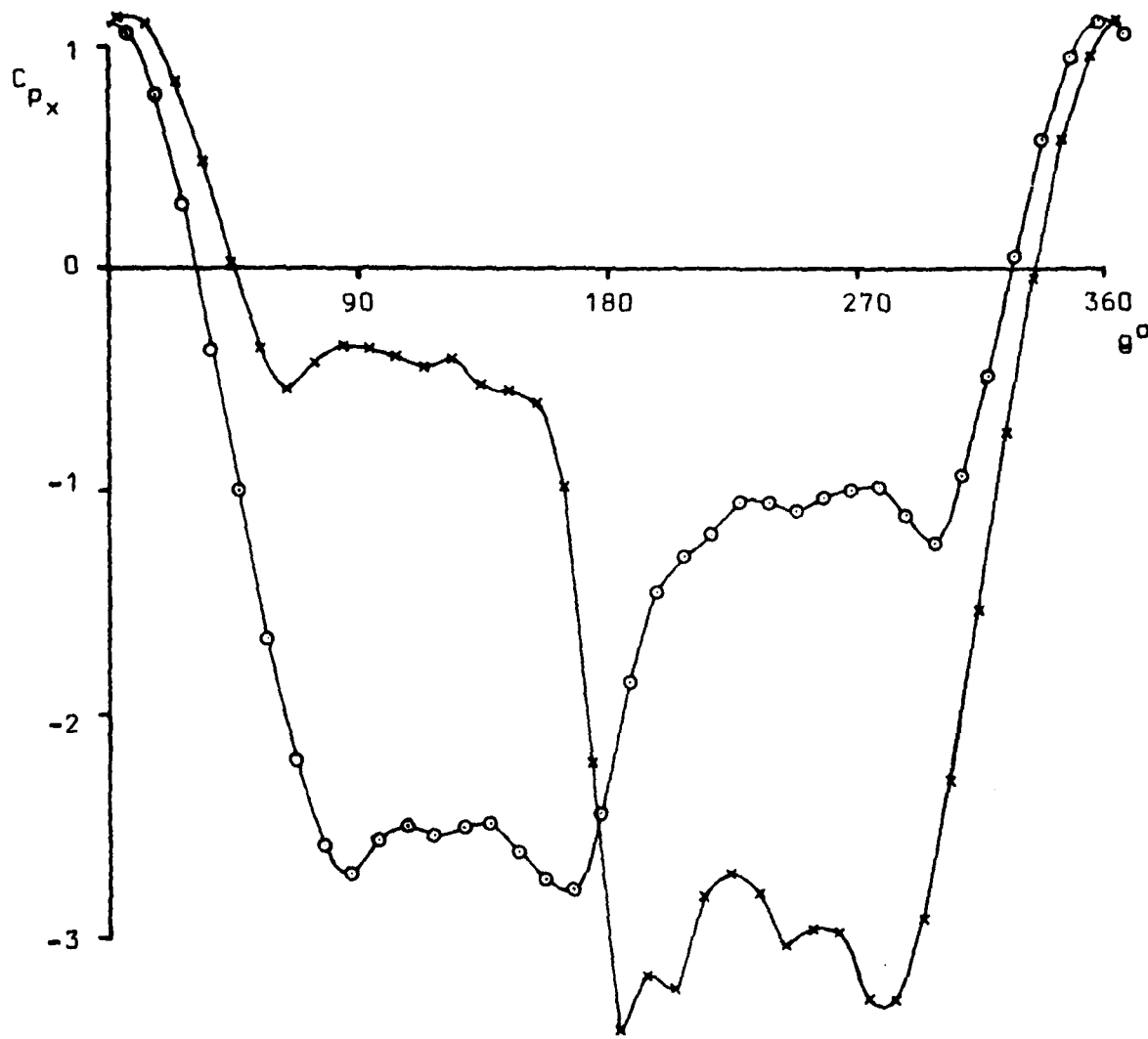
Roll Angle Variation of Maximum Side Forces. 50° Incidence Re=10⁵

Figure 7



Distribution of Local Force Coefficient.
Old Nose 50° Incidence $Re=10^5$

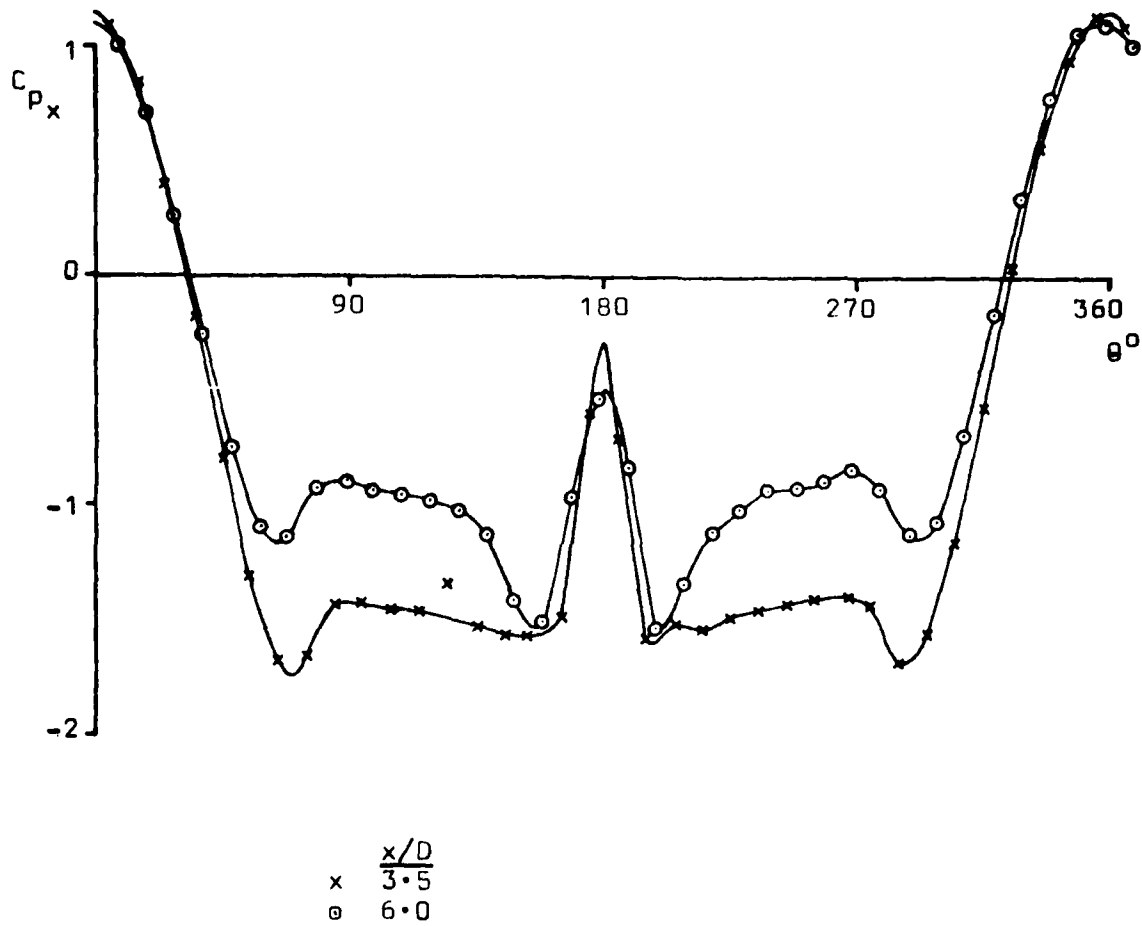
Figure 8



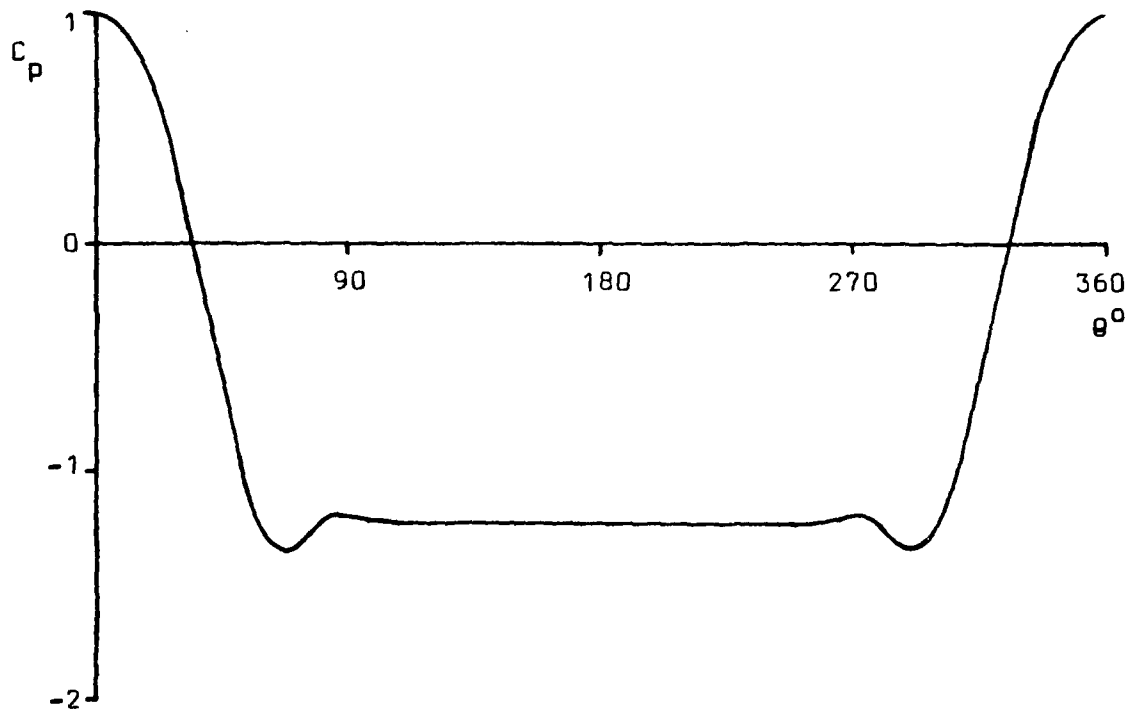
$\frac{x}{D}$
 x 3.5
 o 6.0

Two Circumferential Pressure Distributions
 Old Nose 50° Incidence 0° Roll Angle $Re=10^5$

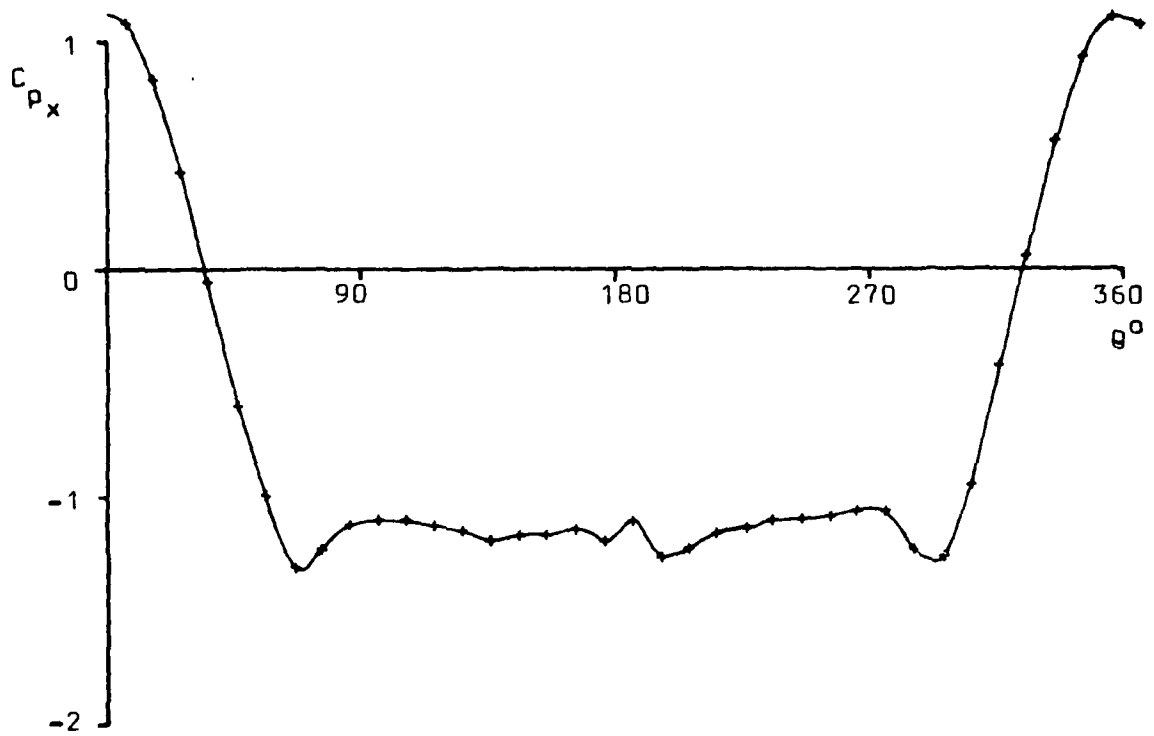
Figure 9



Two Circumferential Pressure Distributions
 Old Nose 50° Incidence $231\frac{1}{2}^\circ$ Roll Angle $Re=10^5$



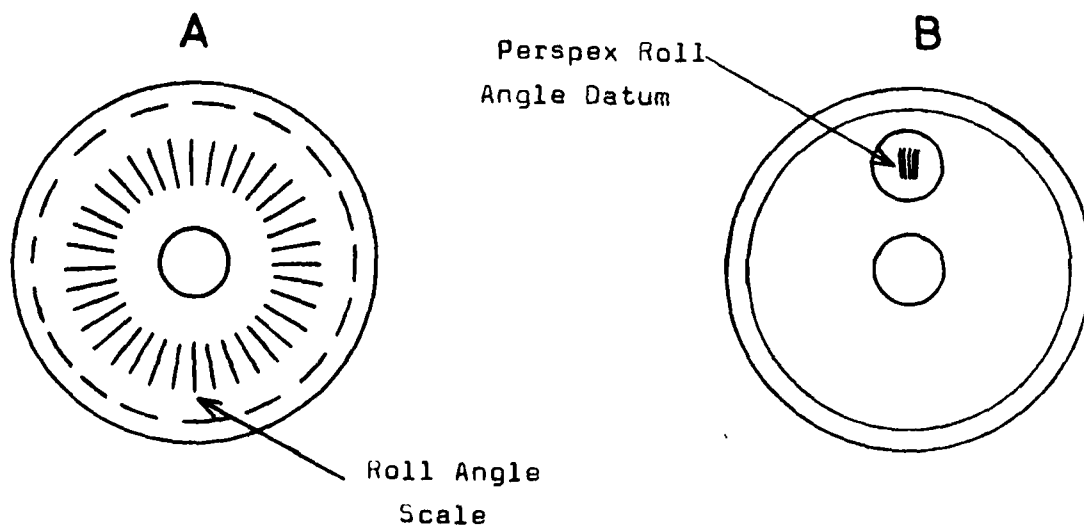
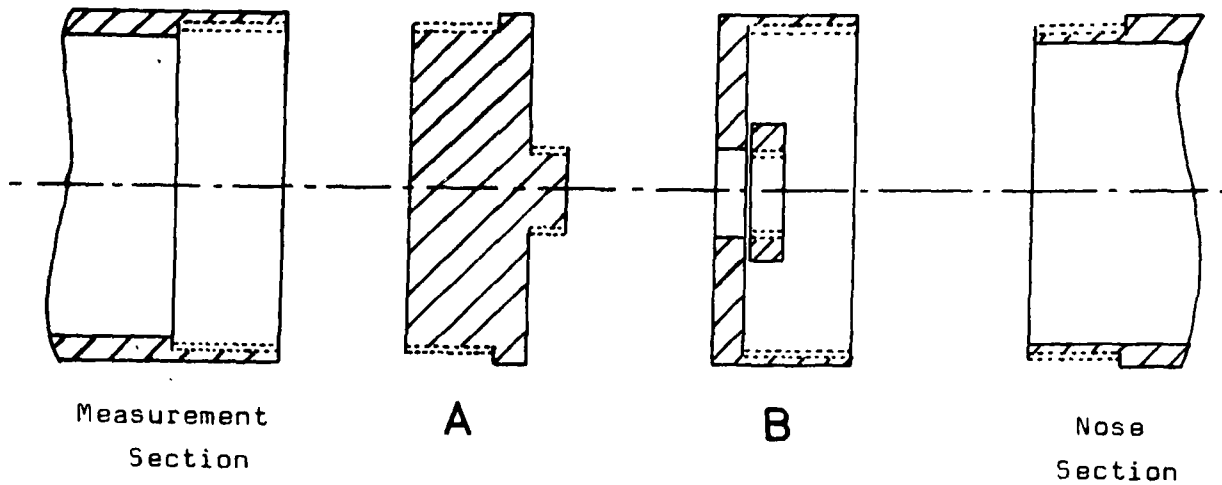
Circumferential Pressure Distribution on a Circular Cylinder at 90° to a Uniform Flow.



$x/D=11.5$

Circumferential Pressure Distribution
Old Nose 50° Incidence 0° Roll Angle $Re=10^5$

Figure 12



Model Section for Independently Rotating Nose.

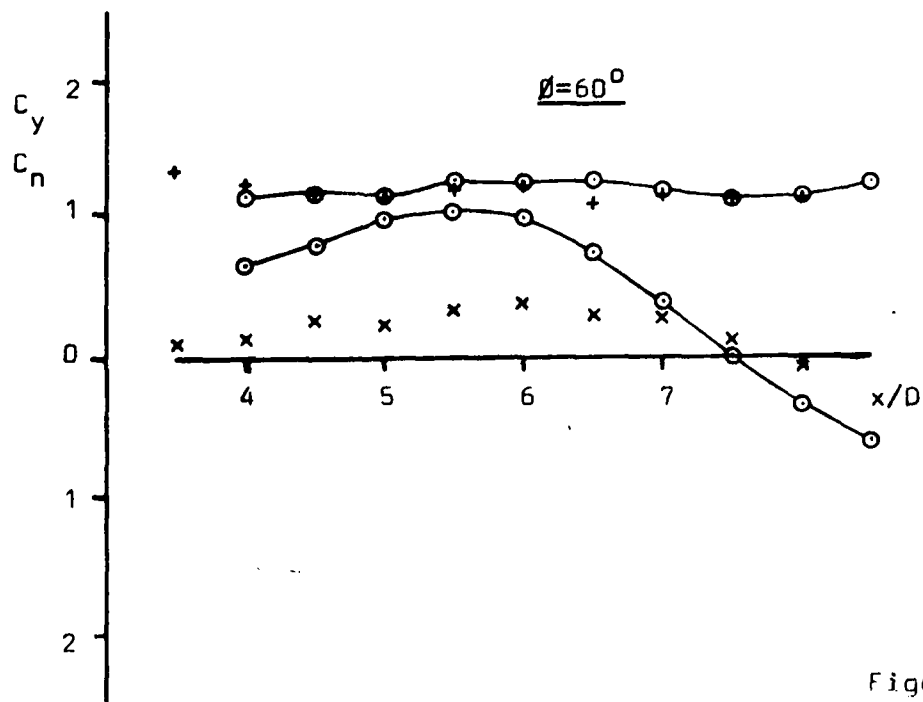
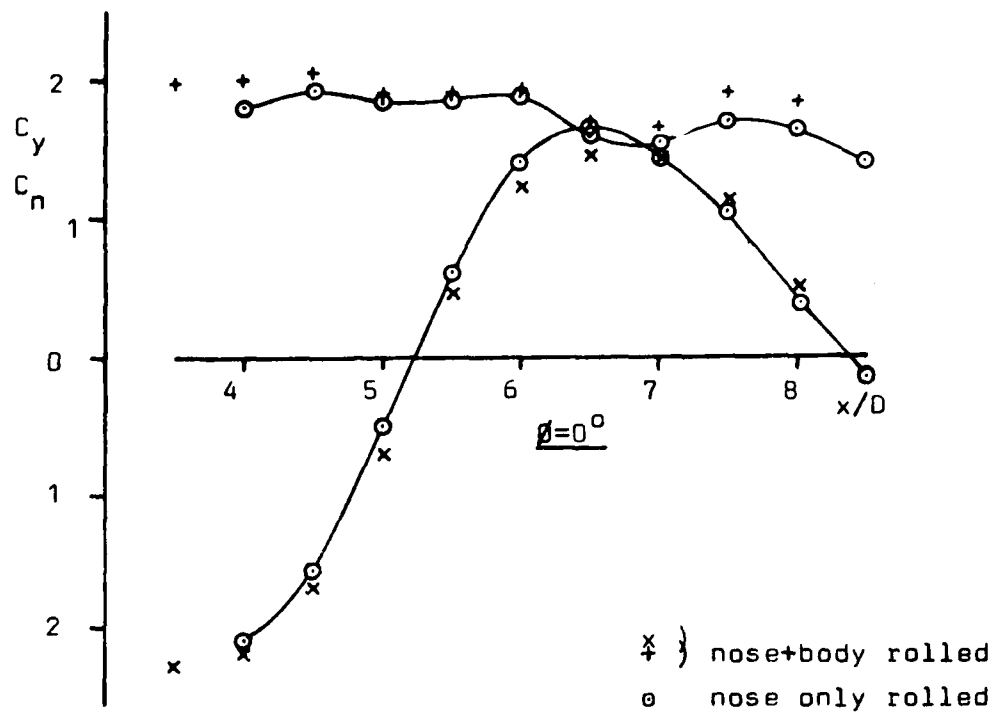
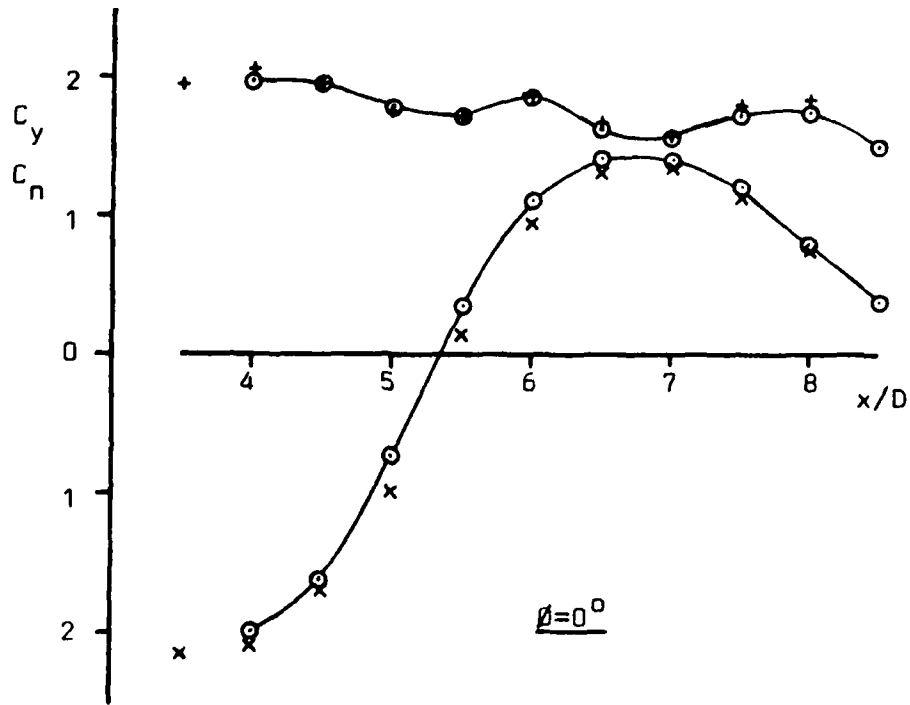


Figure 14
 Comparison of Local Force Distributions With and Without
 Nose Rotator Section. Old Nose 50° Incidence $Re=10^5$



+ } nose+body rolled
 o } nose only rolled

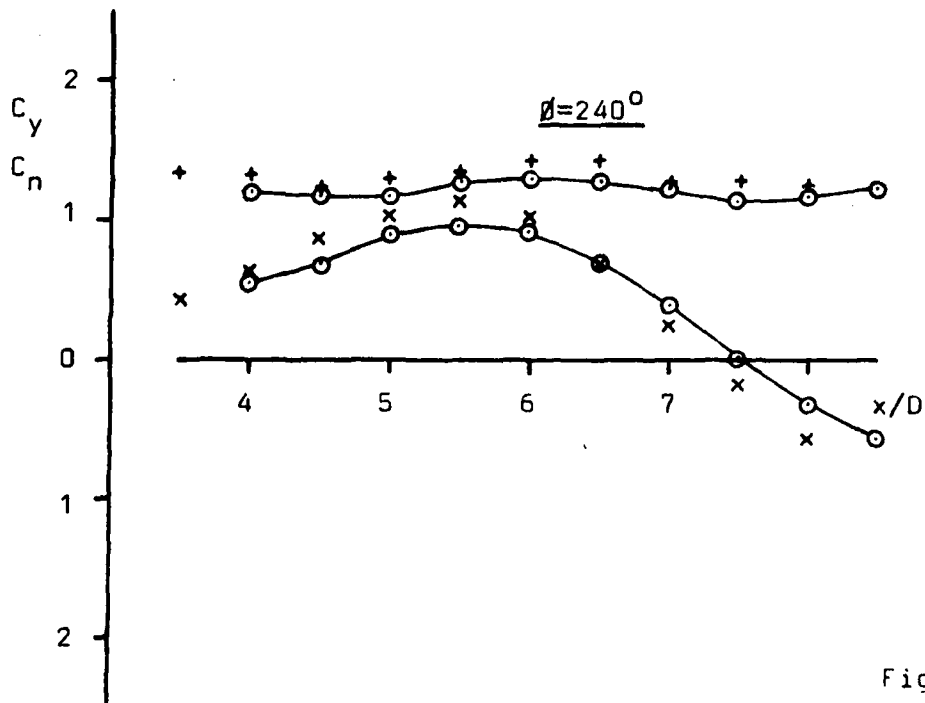
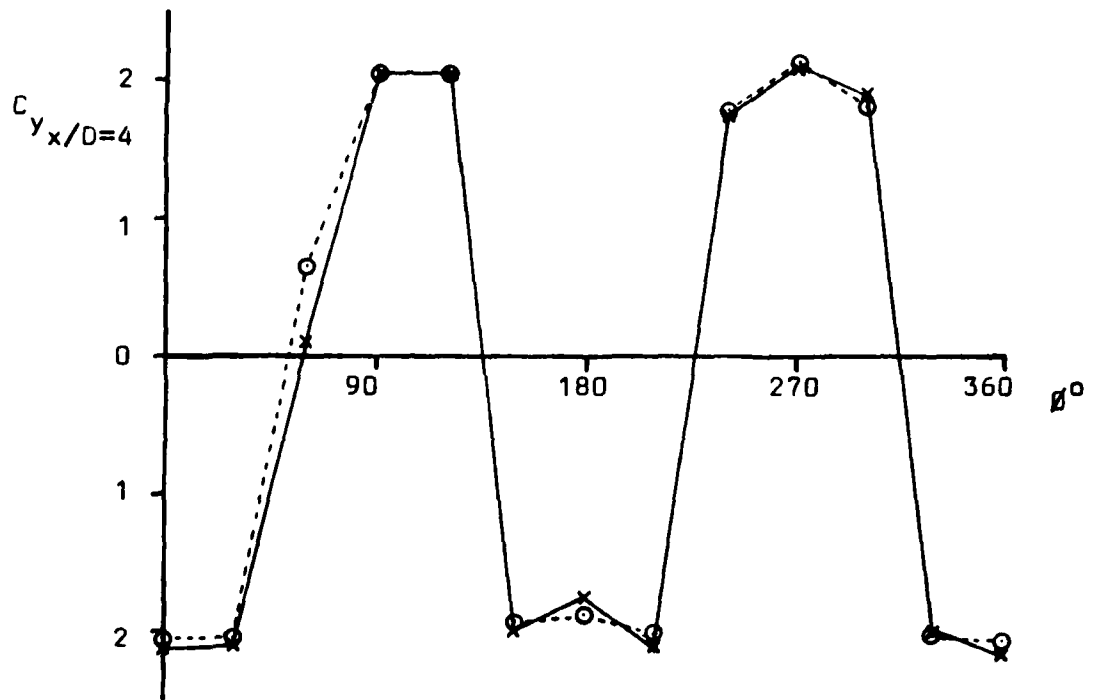


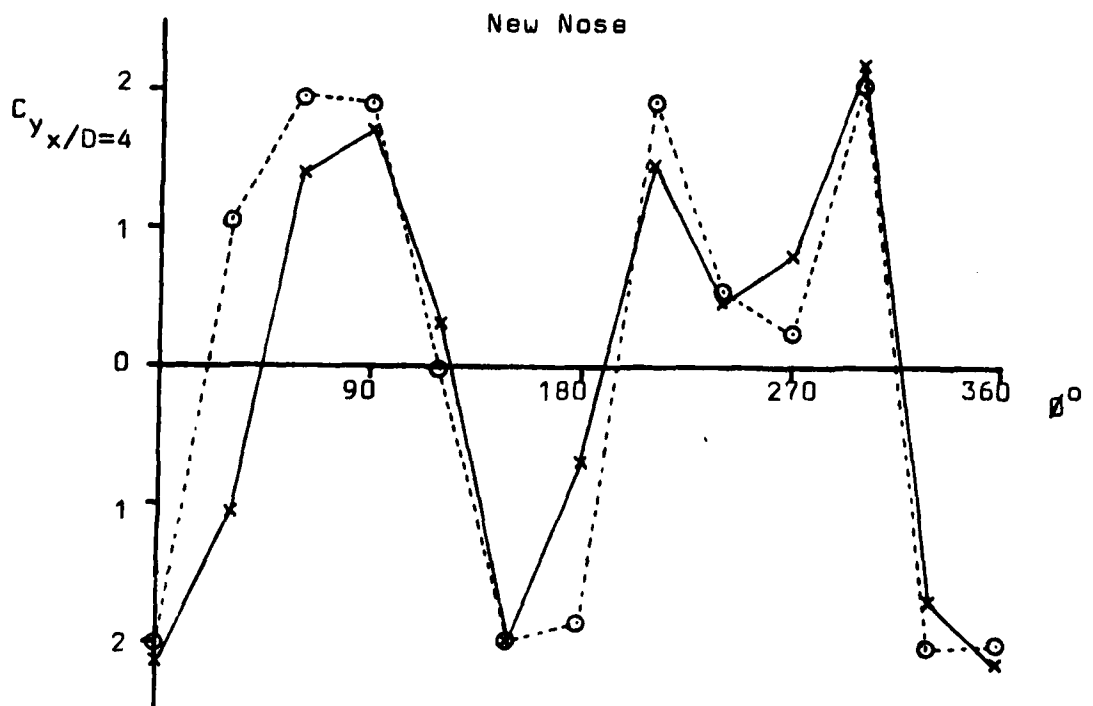
Figure 15

Comparison of Local Force Distributions With and Without
 Nose Rotator Section. New Nose 50° Incidence $Re=10^5$



Old Nose

x nose+body rolled
o nose only rolled

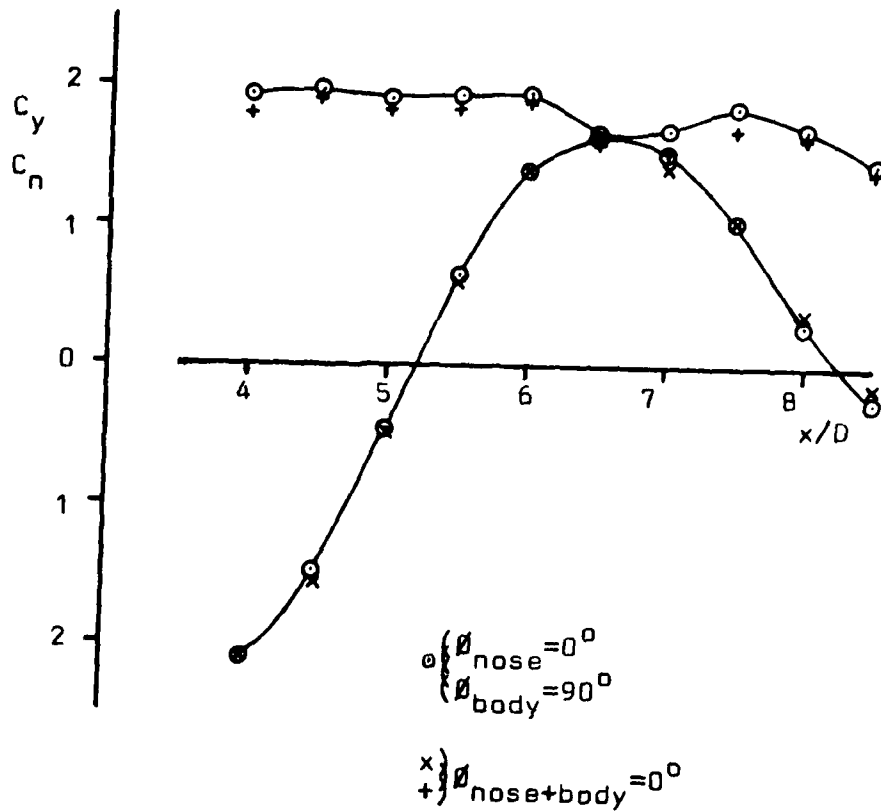


New Nose

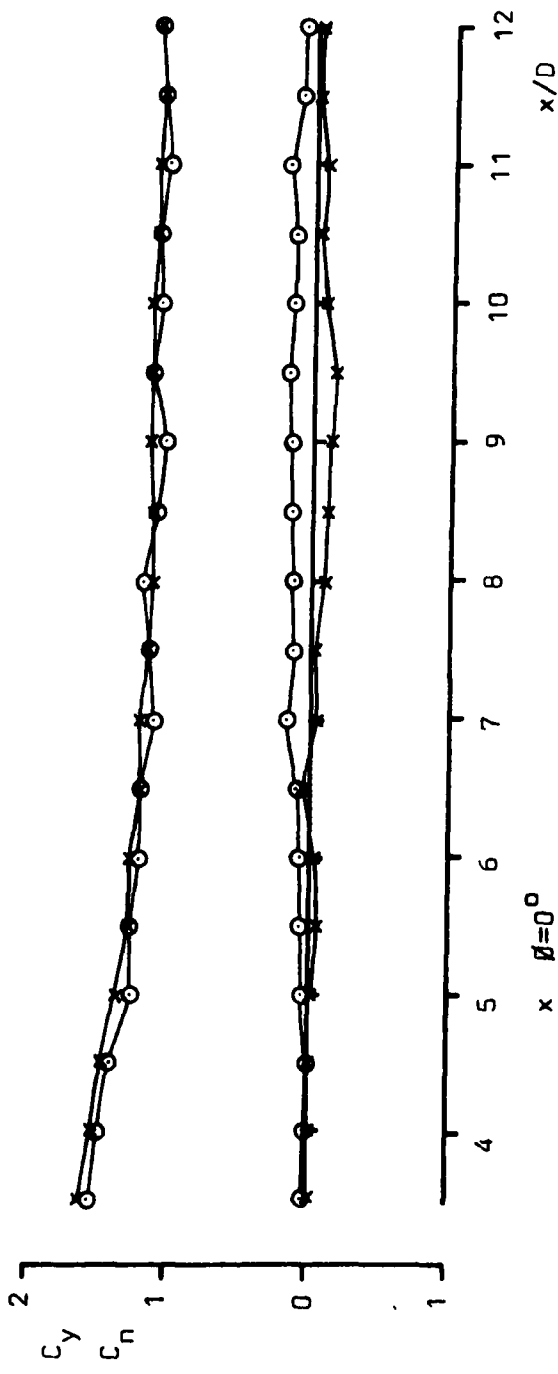
Roll Angle Variation With and Without Nose Rotator Section.

50° Incidence $Re=10^5$

Figure 16



Comparison of Local Force Distributions With and Without
 Nose Rotator Section- Rolling the Body. Old Nose $Re=10^5$
 50° Incidence



Distribution of Local Force Coefficients
 New Nose 30° Incidence $Re=10^5$

Figure 18

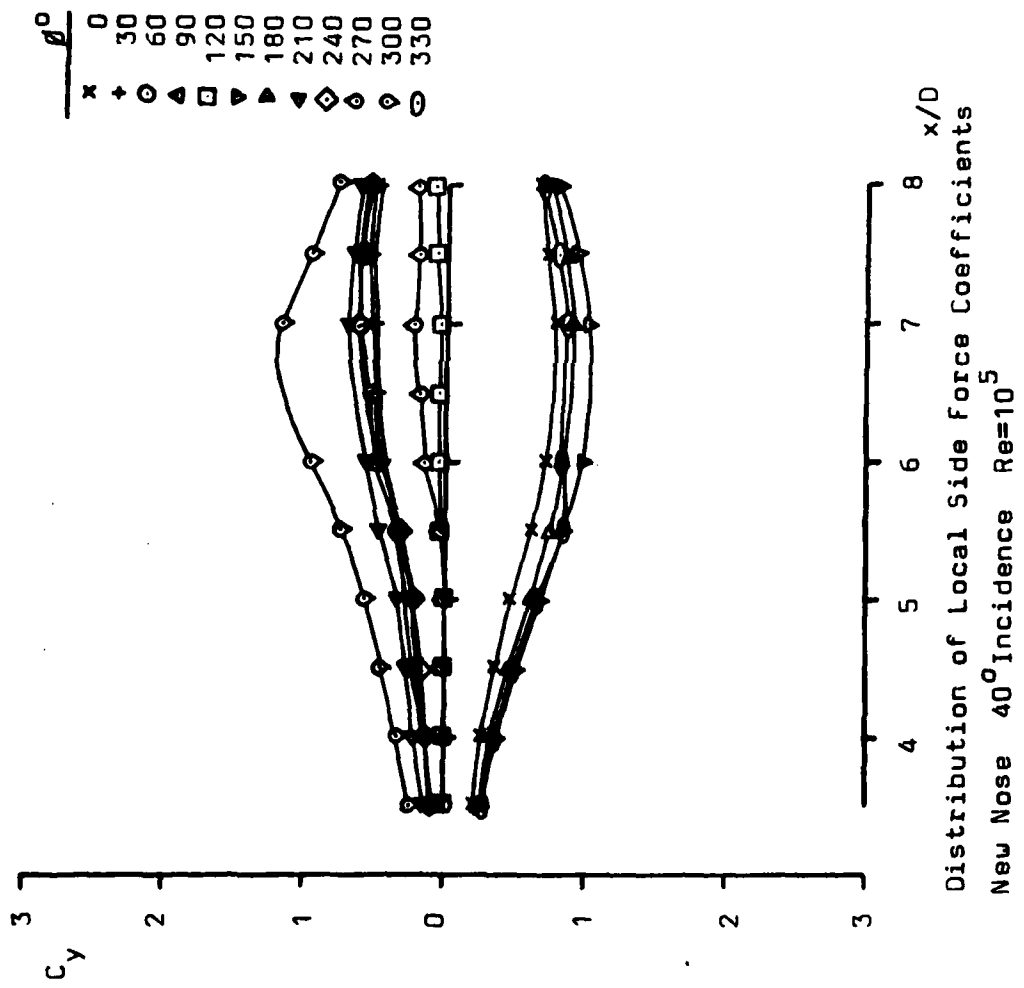
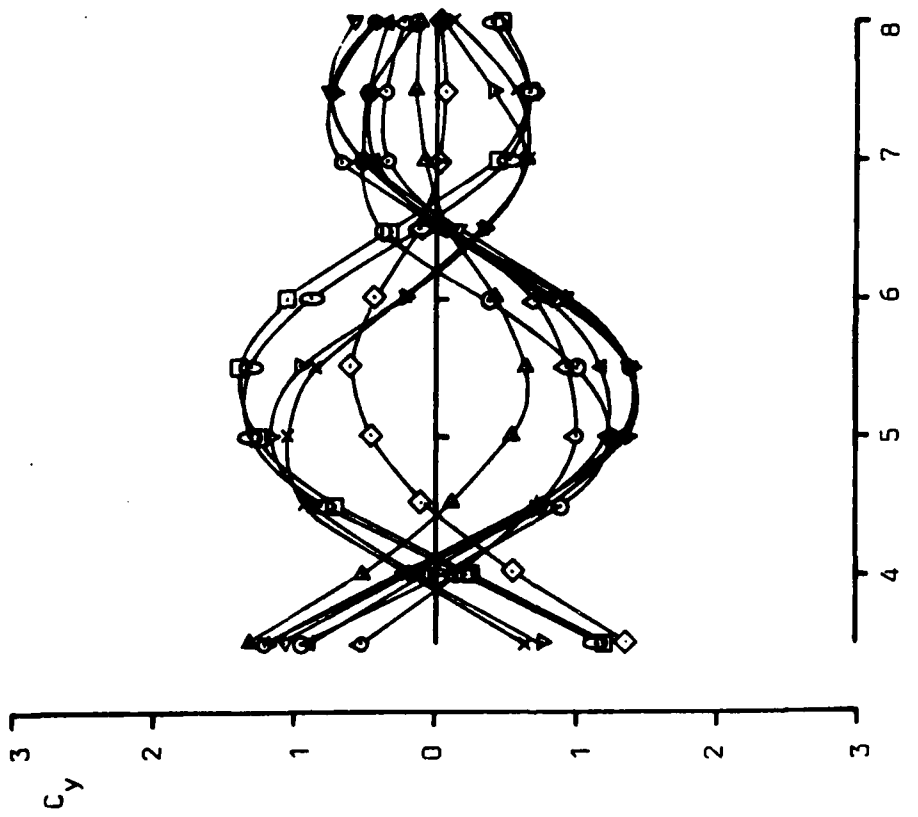


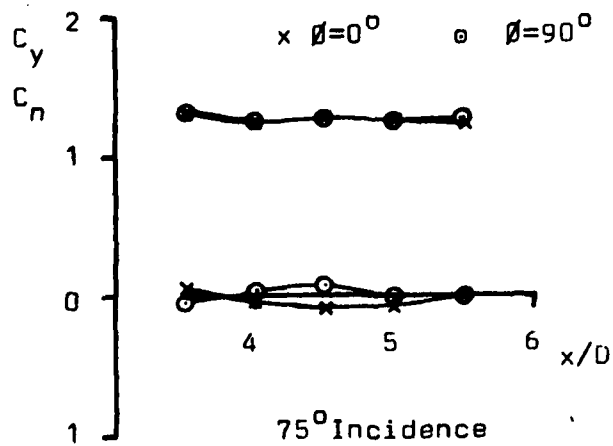
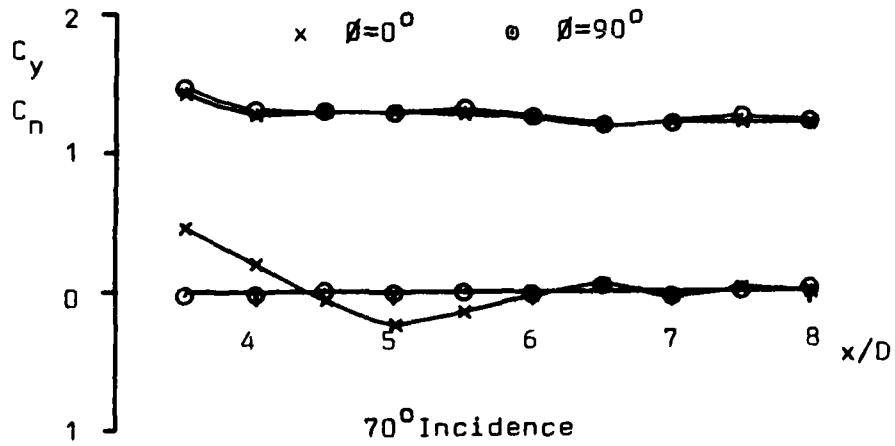
Figure 19

β°	Symbol
0	x
30	+
60	o
90	△
120	□
150	▽
180	▲
210	◀
240	◇
270	◊
300	◐
330	◑

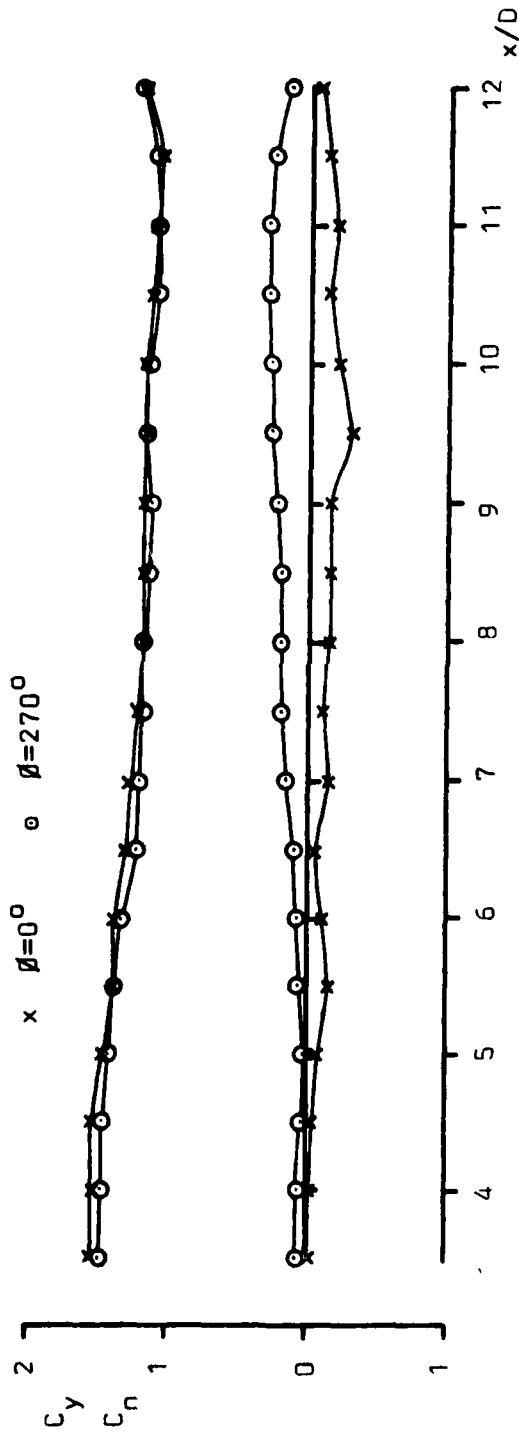


Distribution of Local Side Force Coefficients
 New Nose 60° Incidence $Re=10^5$

Figure 20

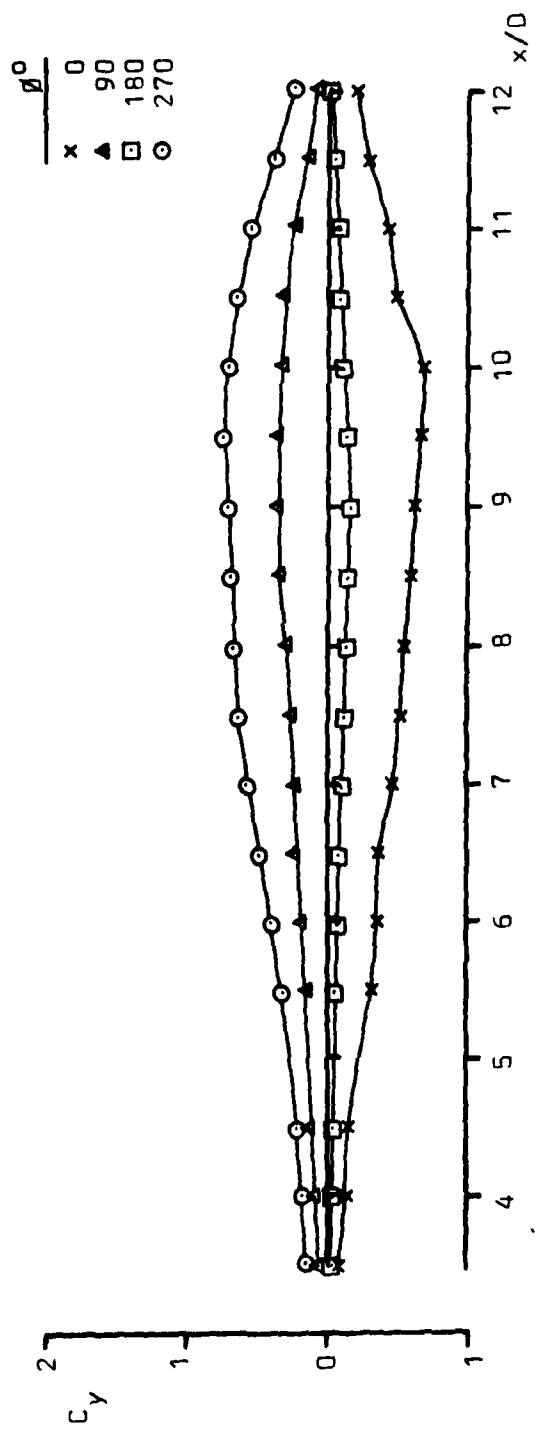


Distribution of Local Force Coefficients
New Nose $Re=10^5$



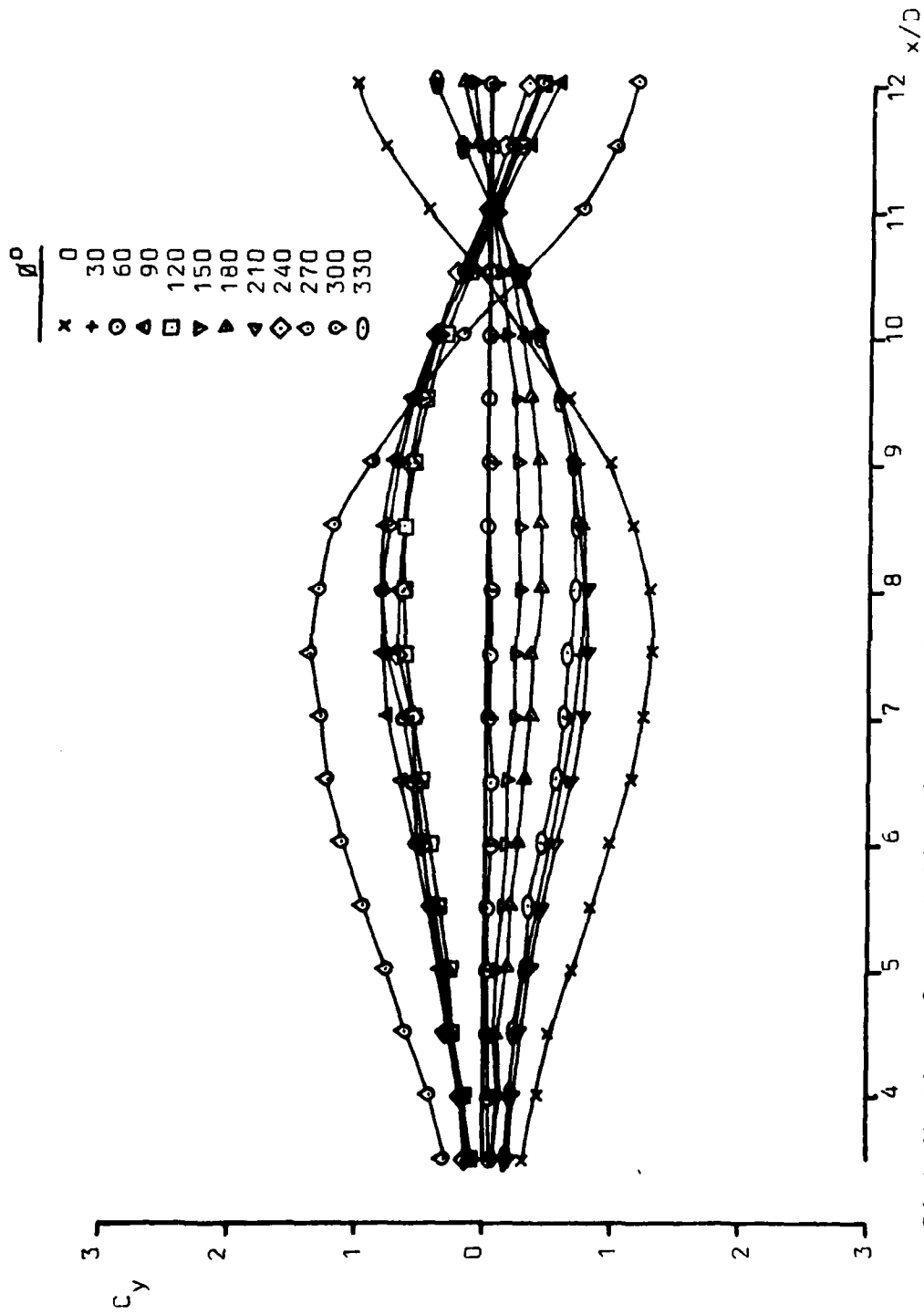
Distribution of Local Side Force Coefficients
 Old Nose 25° Incidence $Re=10^5$

Figure 22



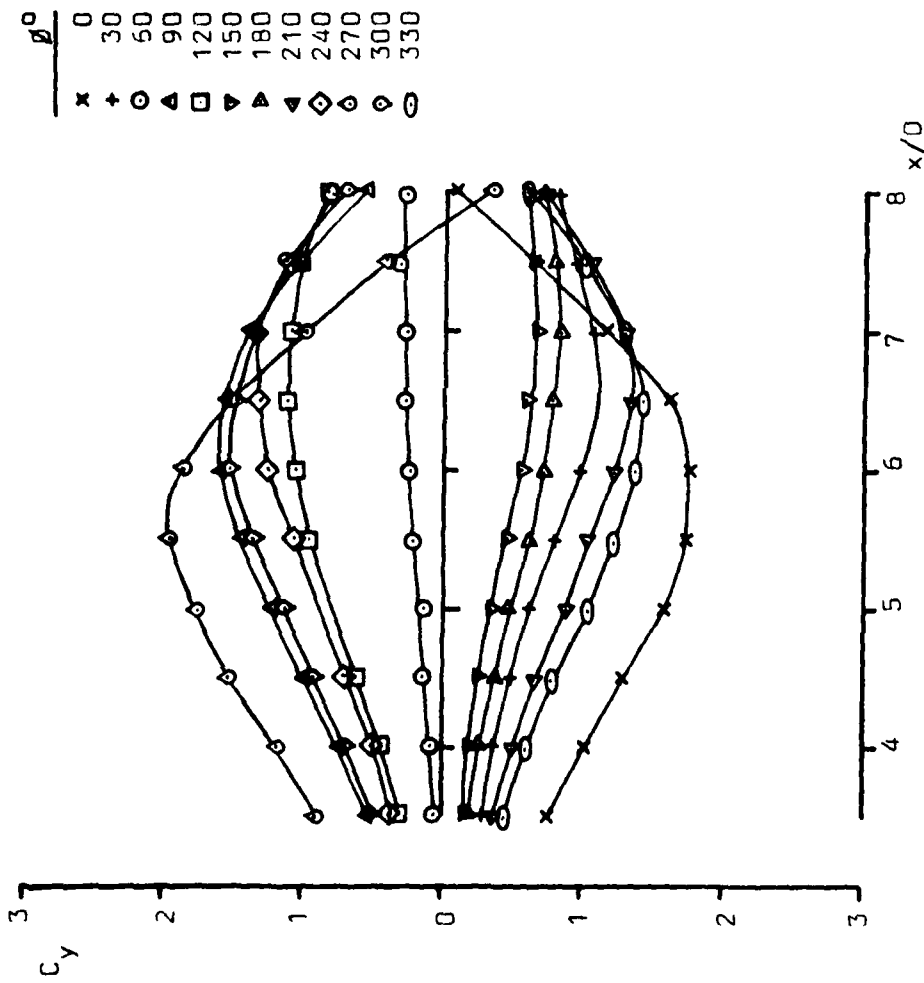
Distribution of Local Side Force Coefficients
 Old Nose 30° Incidence $Re=10^5$

Figure 23



Distribution of Local Side Force Coefficients
Old Nose 35° Incidence $Re=10^5$

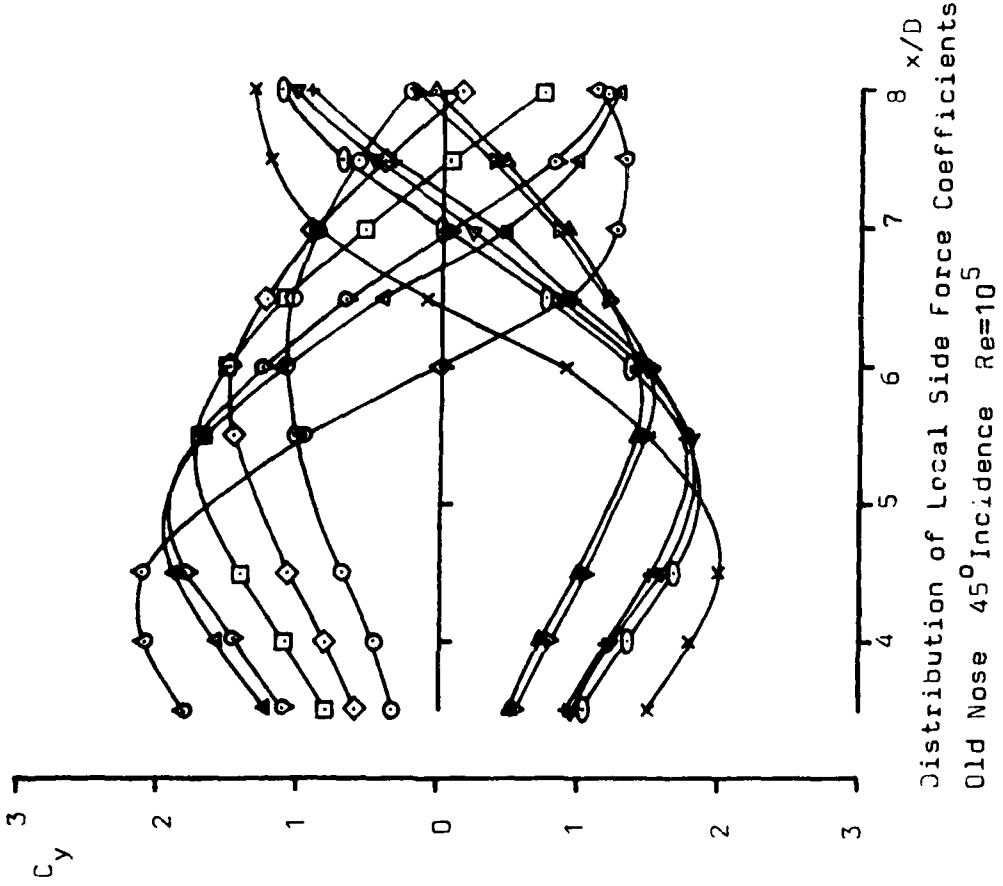
Figure 24



Distribution of Local Side Force Coefficients
Old Nose 40° Incidence $Re=10^5$

Figure 25

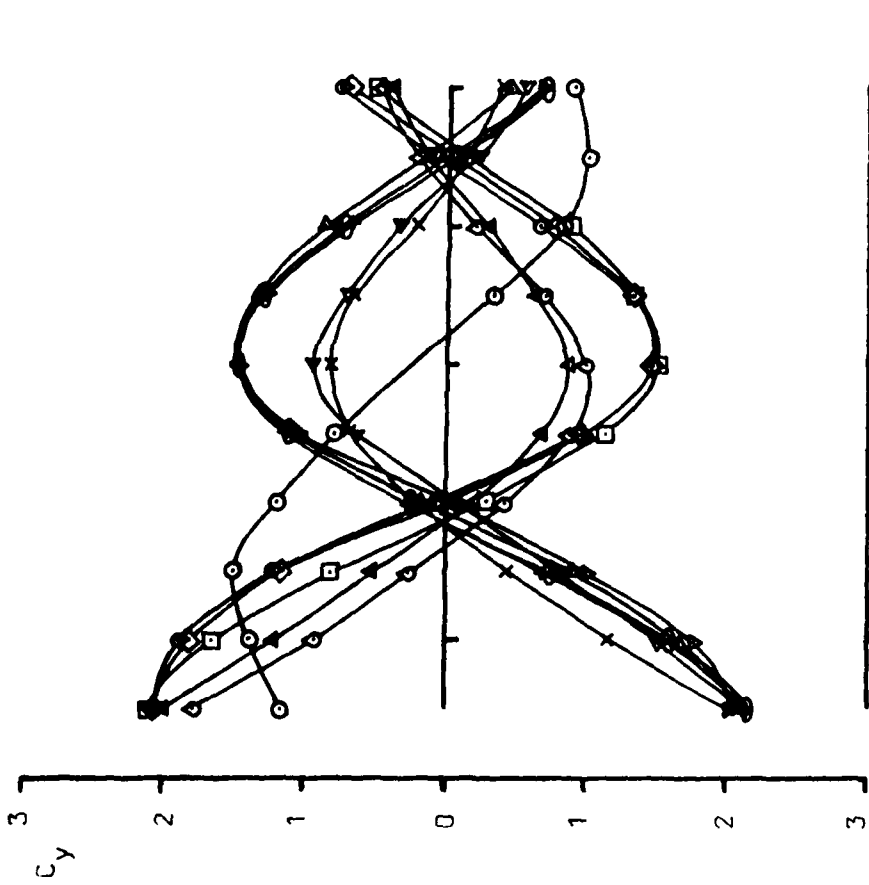
θ°
0
30
60
90
120
150
180
210
240
270
300
330



Distribution of Local Side Force Coefficients
Old Nose 45° Incidence $Re=10^5$

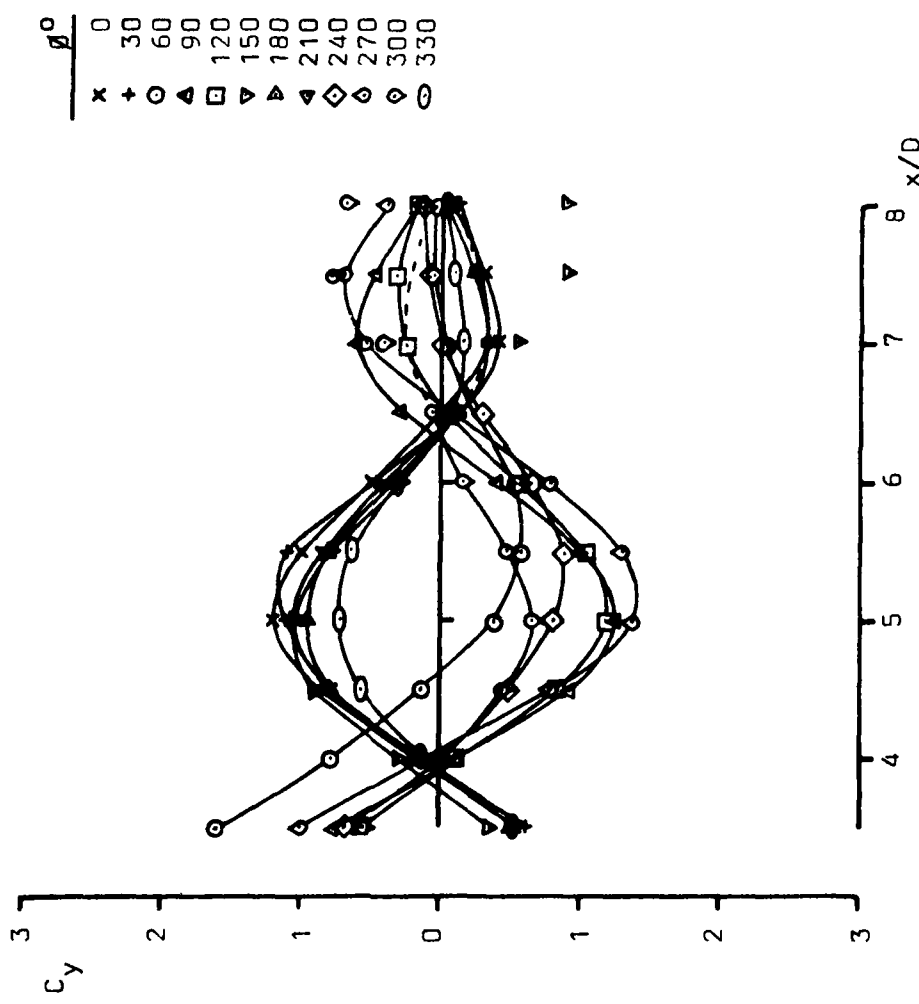
Figure 26

θ°	Symbol
0	x
30	+
60	o
90	△
120	□
150	▽
180	▲
210	▼
240	◇
270	○
300	◊
330	◐



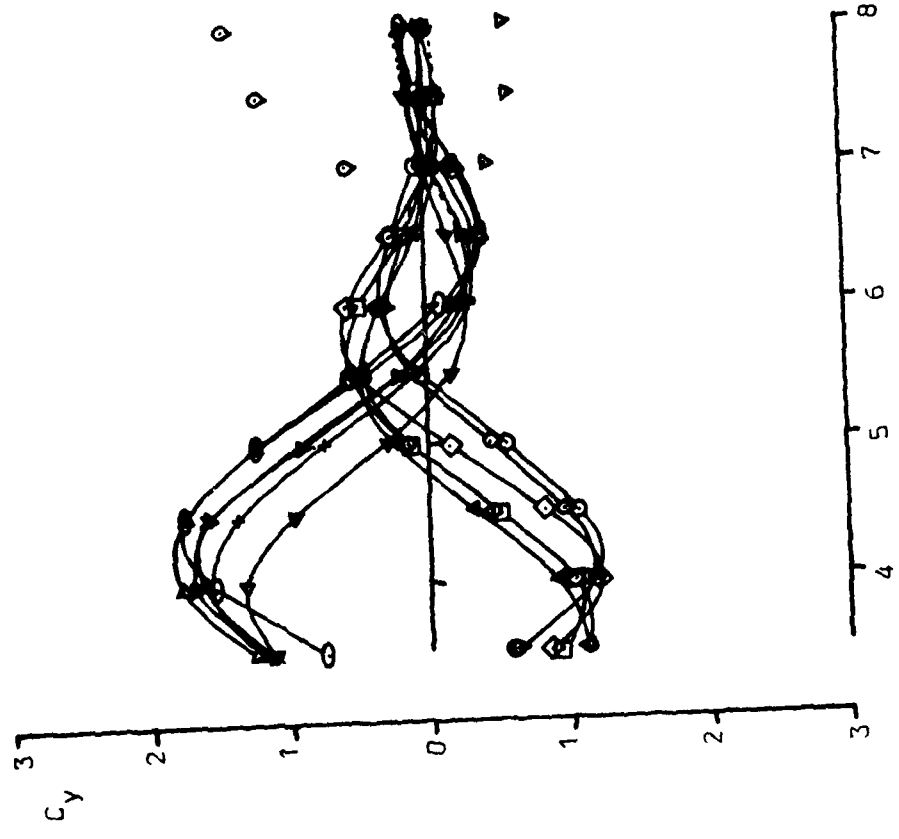
Distribution of Local Side Force Coefficients
Old Nose 55° Incidence $Re=10^5$

Figure 27



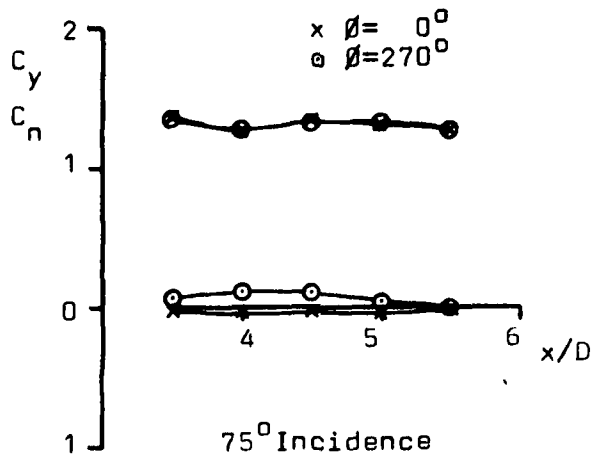
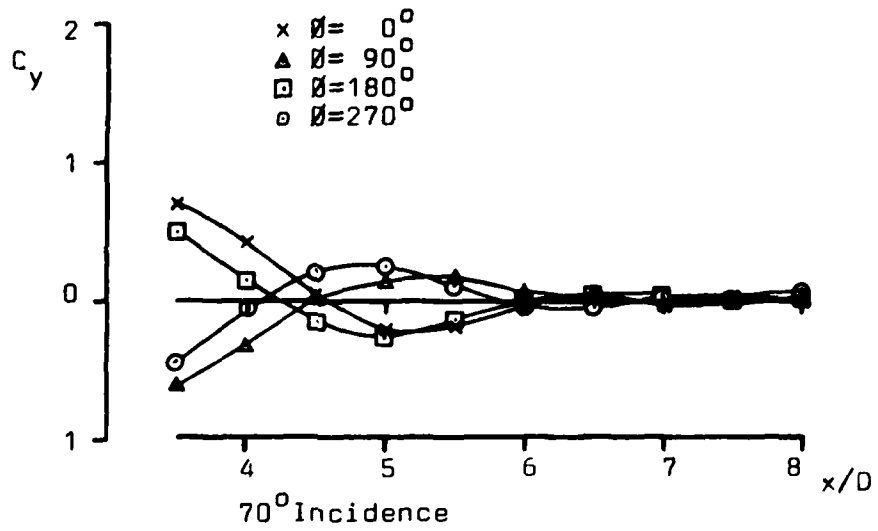
Distribution of Local Side Force Coefficients
Old Nose 60° Incidence $Re=10^5$

θ°
0
30
60
90
120
150
180
210
240
270
300
330

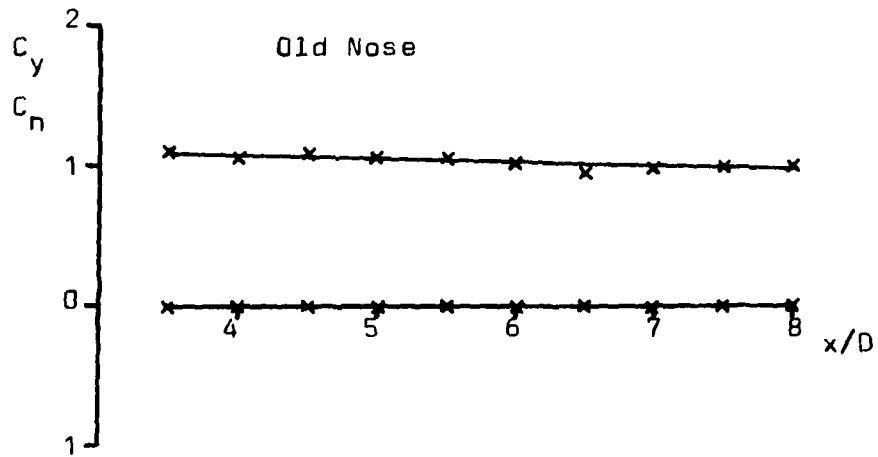
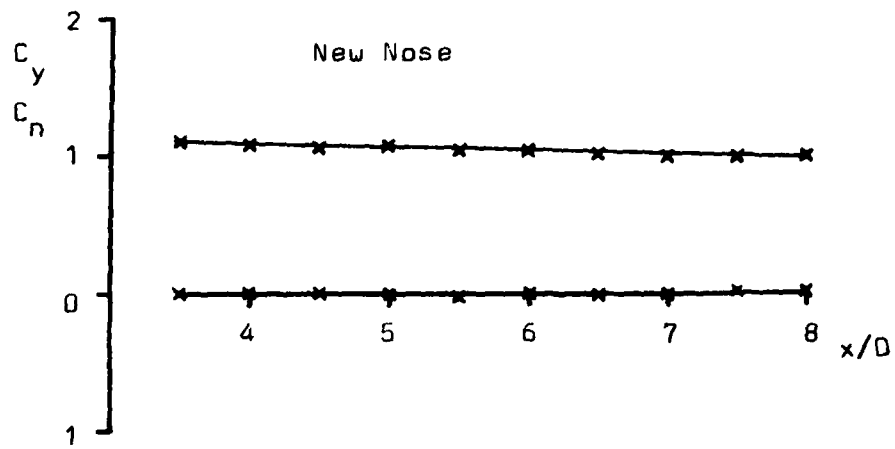


Distribution of Local Side Force Coefficients
Old Nose 65° Incidence $Re=10^5$

Figure 29



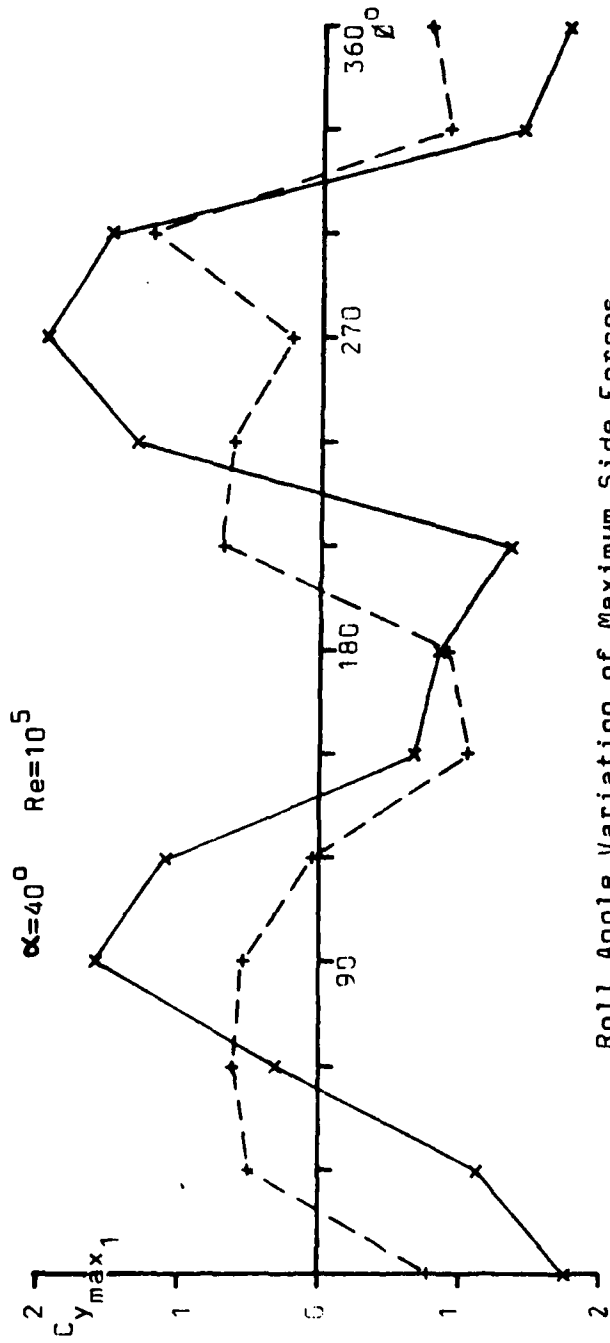
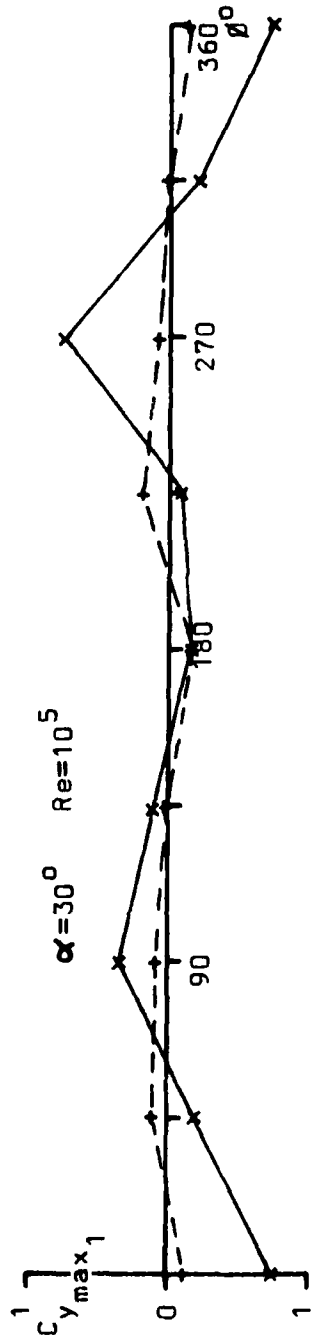
Distribution of Local Force Coefficients
 Old Nose $Re=10^5$



Distribution of Local Force Coefficients.
 0° Roll 90° Incidence $Re=10^5$

Figure 31

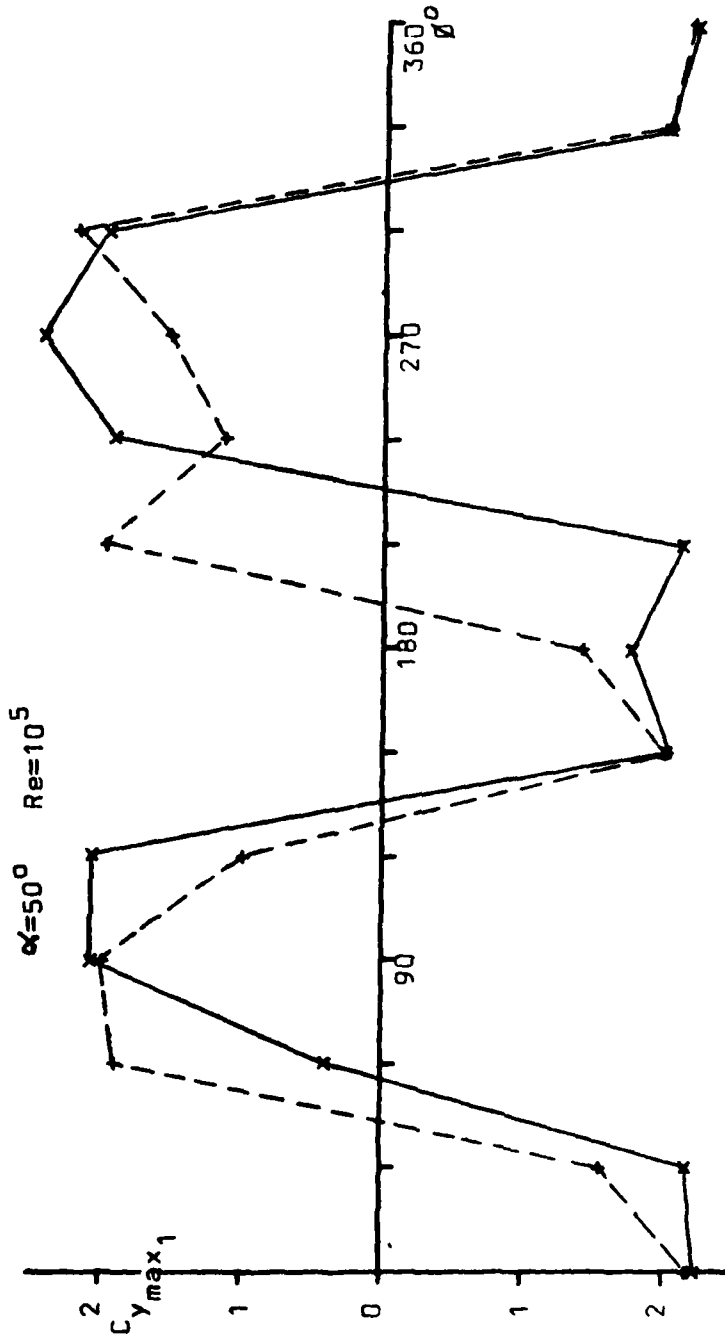
x Old Nose + New Nose



Roll Angle Variation of Maximum Side Forces.

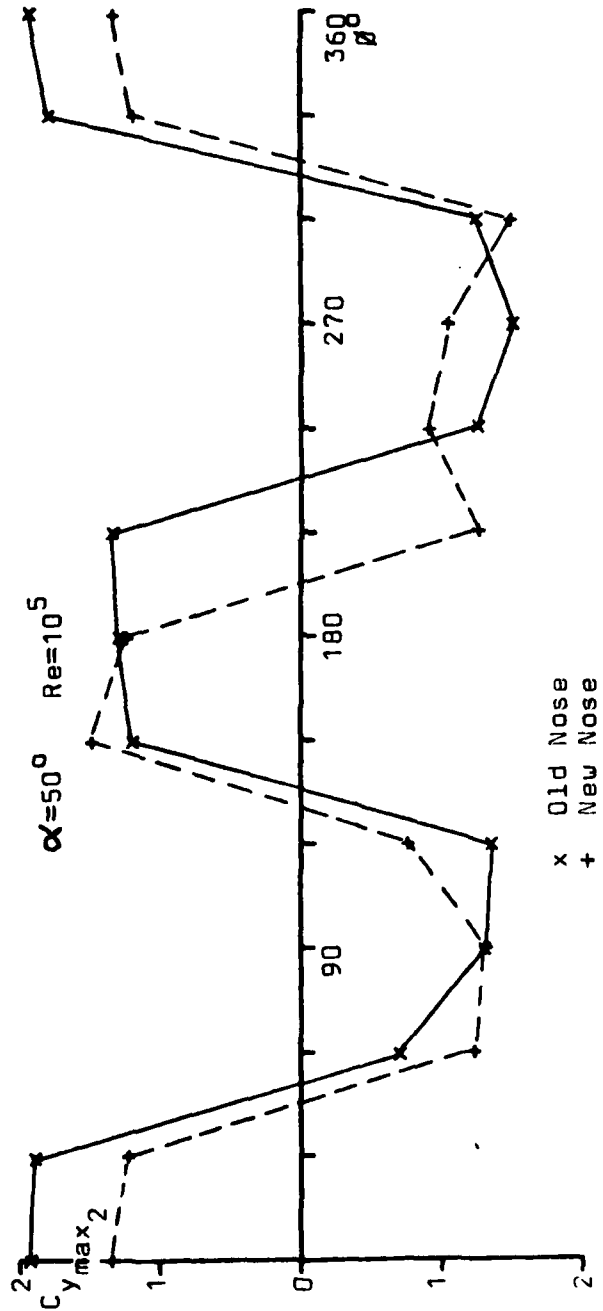
Figure 32

x Old Nose
+ New Nose



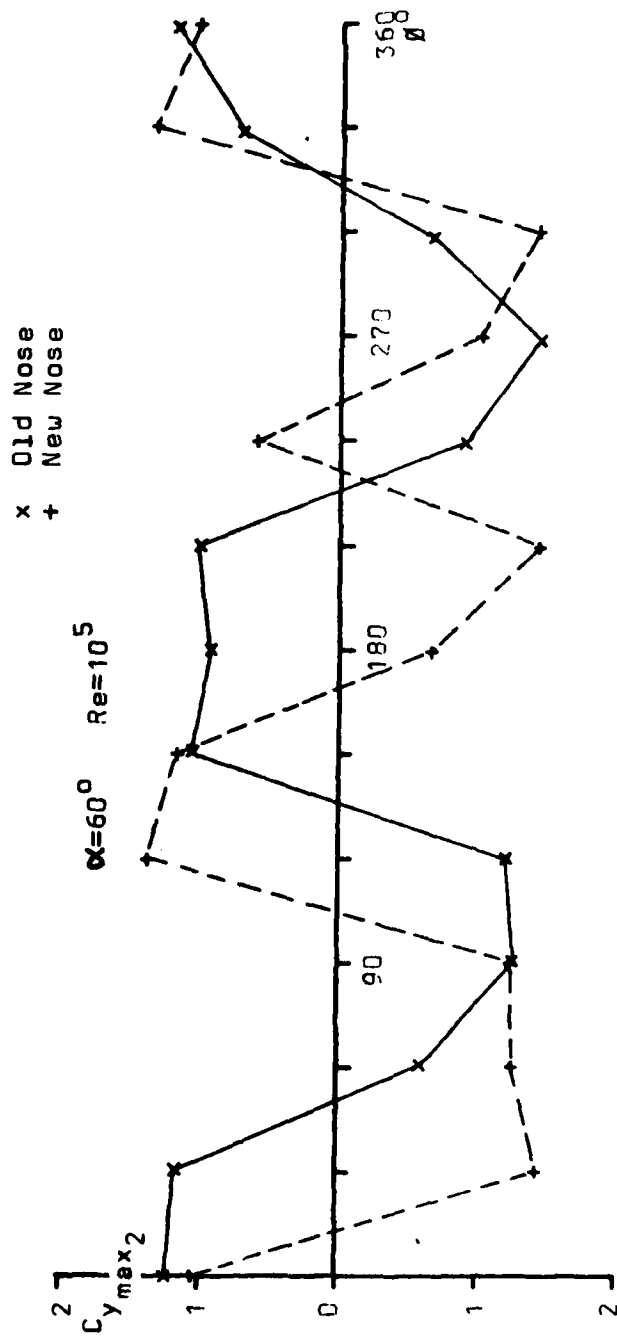
Roll Angle Variation of Maximum Side Forces.

Figure 33



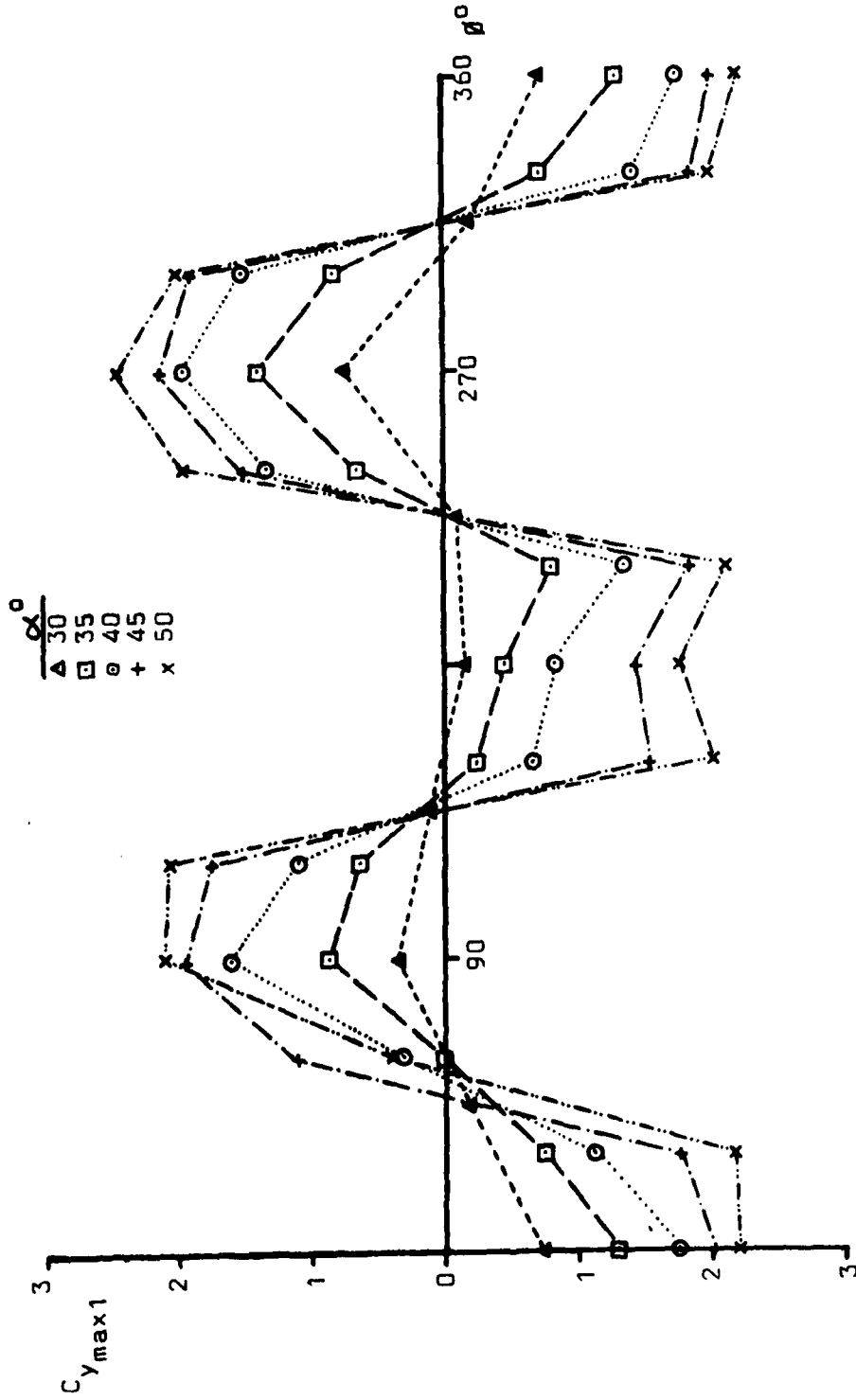
Roll Angle Variation of Maximum Side Forces:-Second Half-Cycle.

Figure 34



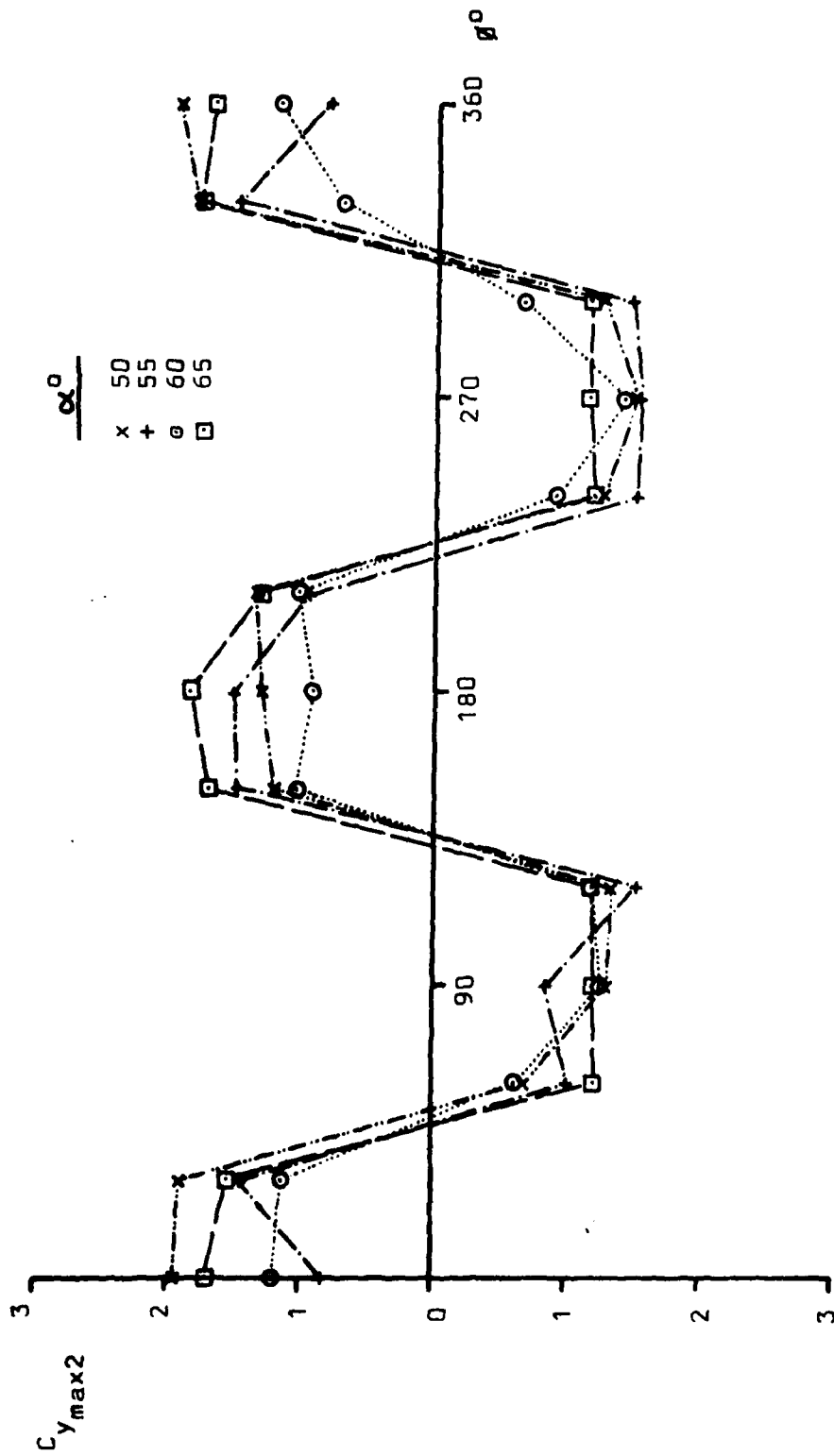
Roll Angle Variation of Maximum Side Forces:--Second Half-Cycle.

Figure 35



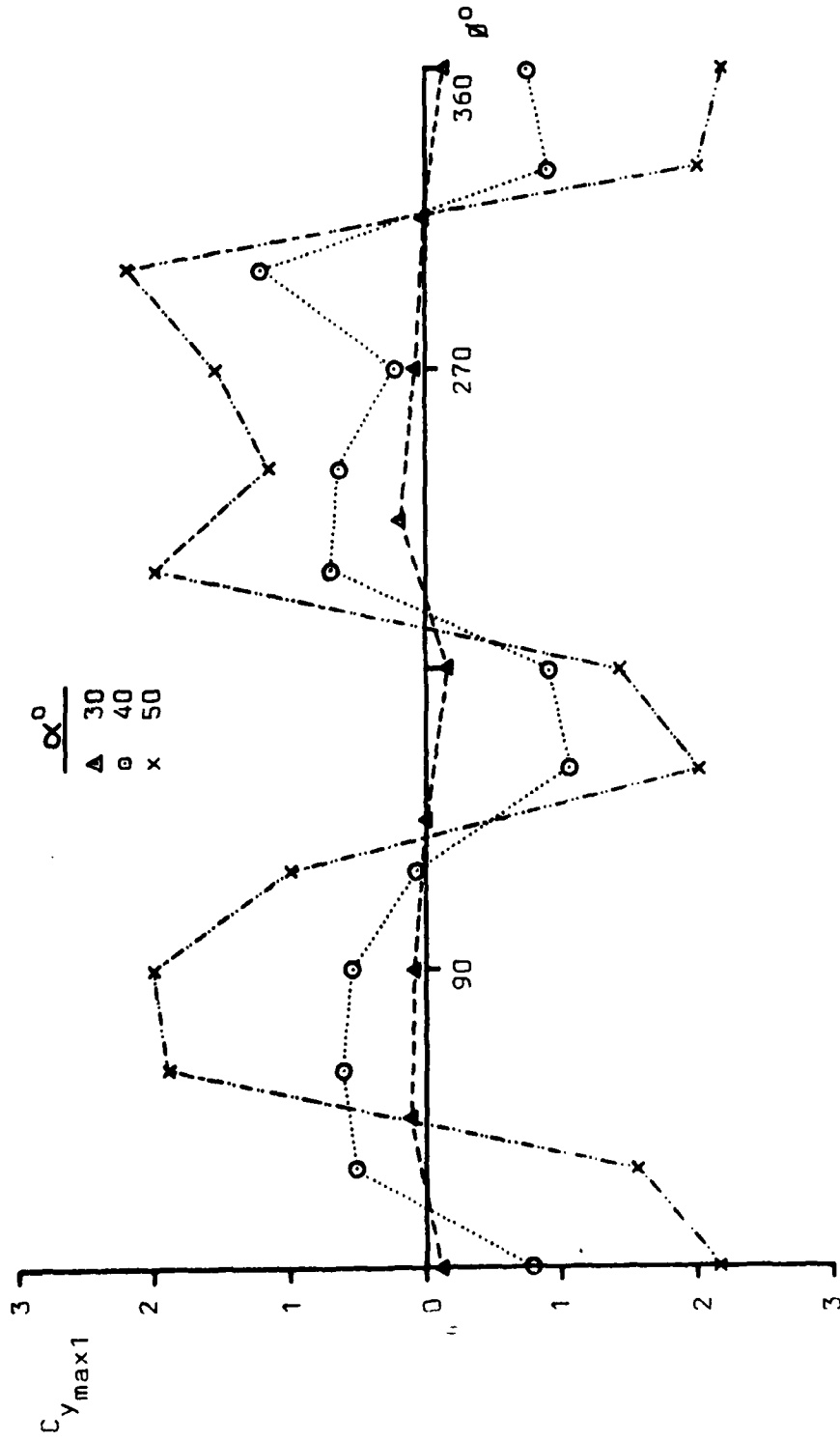
Roll Angle Variation of Maximum Side Forces:-First Half-Cycle.
Old Nose $Re=10^5$

Figure 36

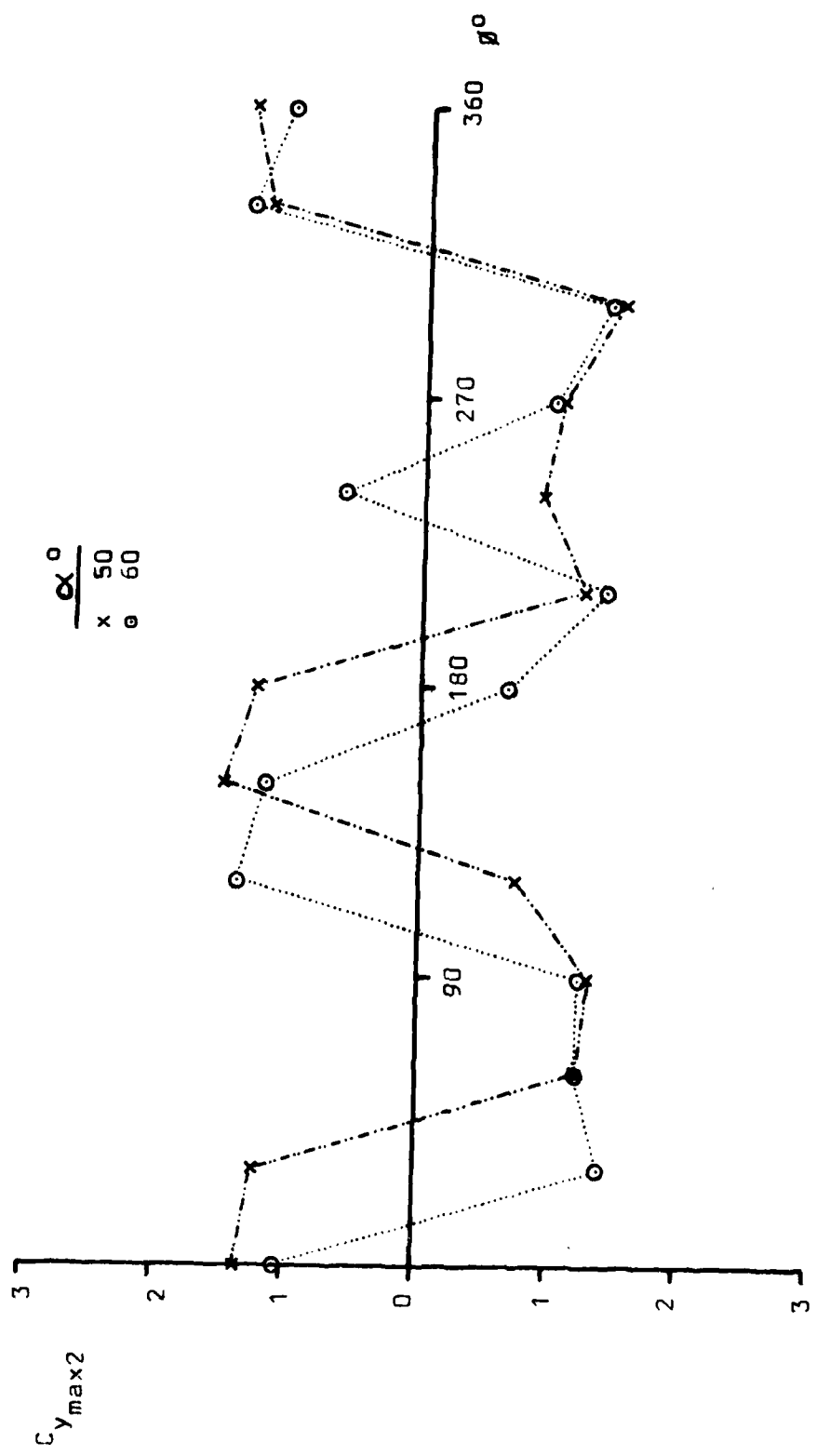


Roll Angle Variation of Maximum Side Forces:-Second Half-Cycle.
Old Nose $Re=10^5$

Figure 37

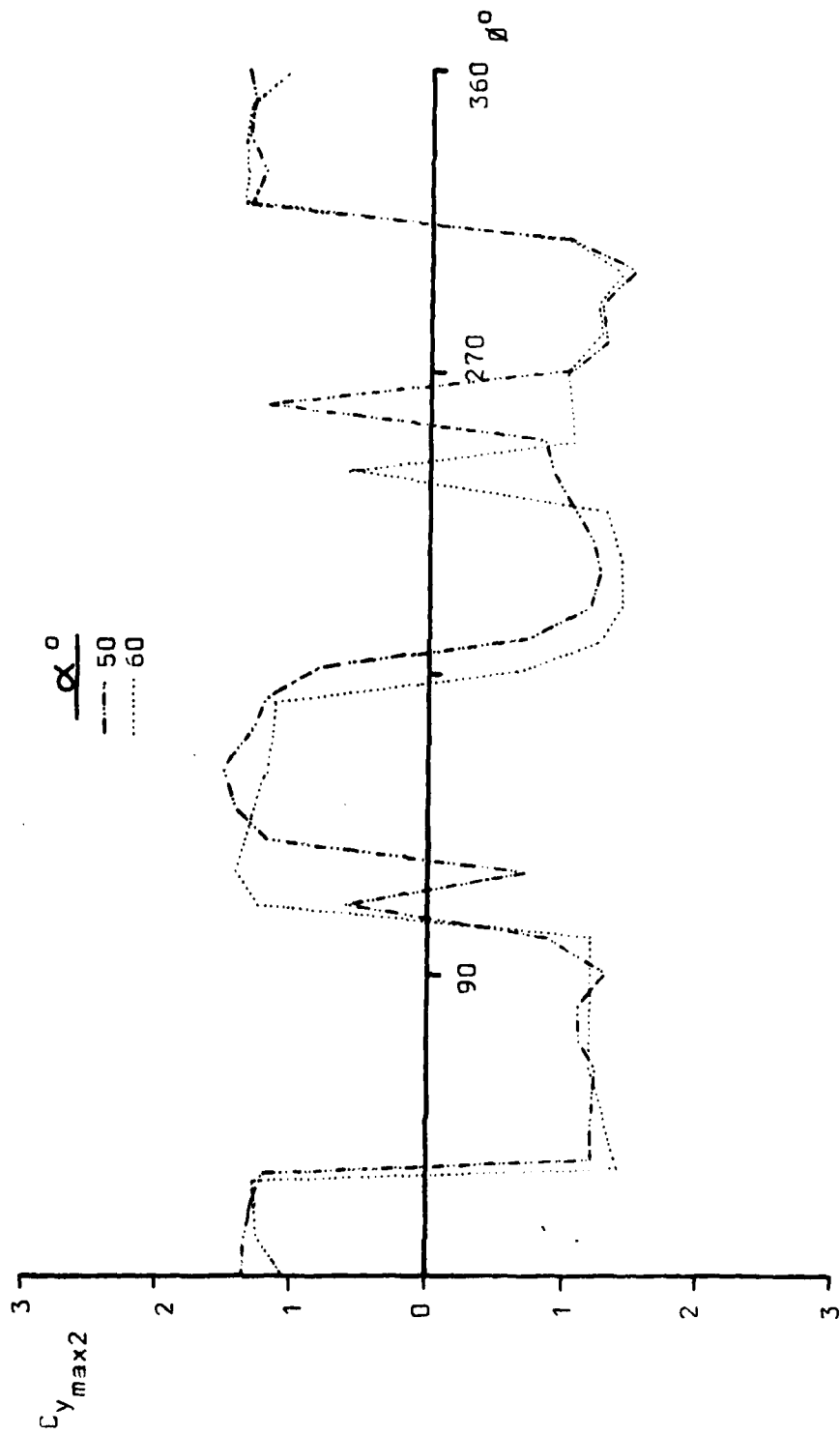


Roll Angle Variation of Maximum Side Forces:-first Half-Cycle.
 New Nose $Re=10^5$



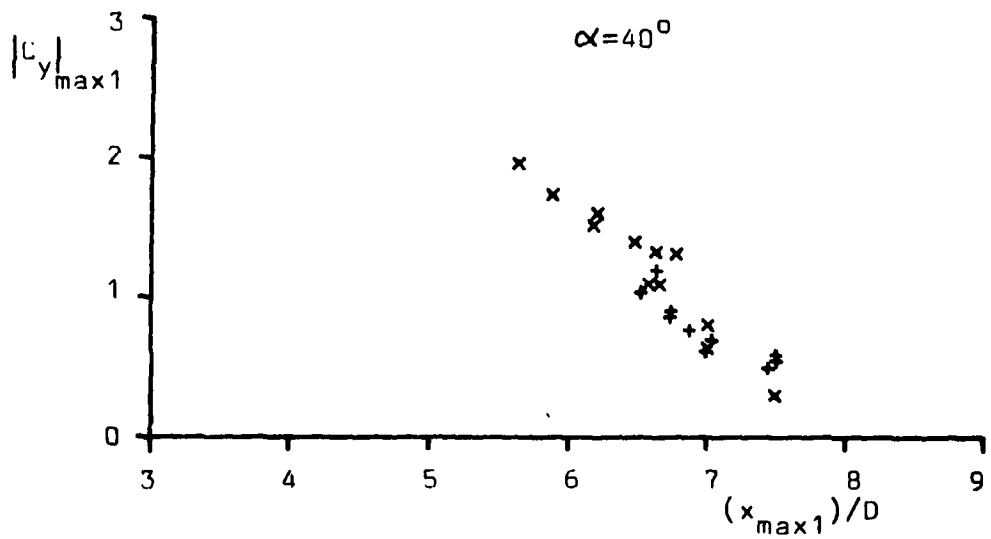
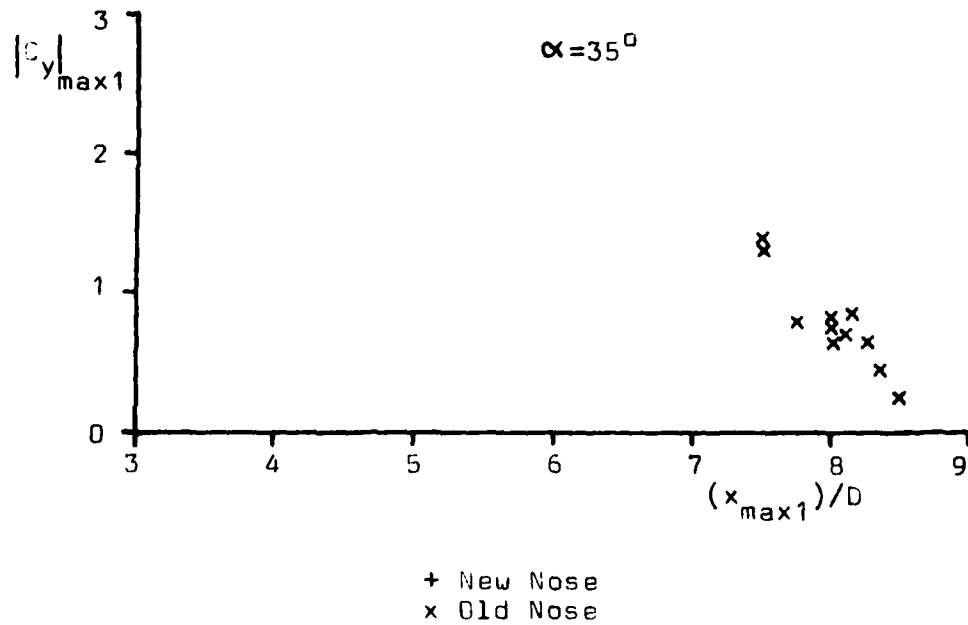
Roll Angle Variation of Maximum Side Forces:--Second Half-Cycle.
 New Nose Re=10⁵

Figure 39

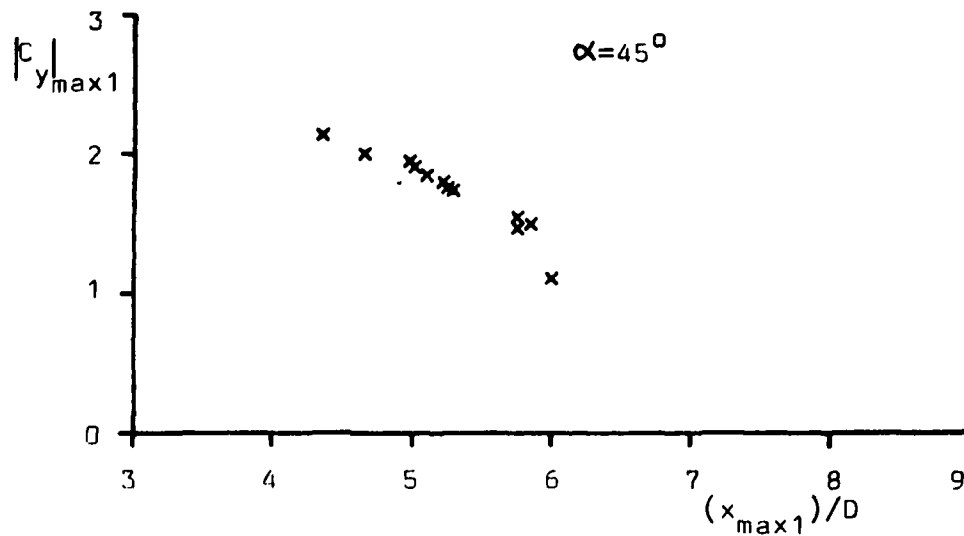


Suggested Roll Angle Variation of Maximum Side Forces:-Second Half-Cycle.
 New Nose $Re=10^5$

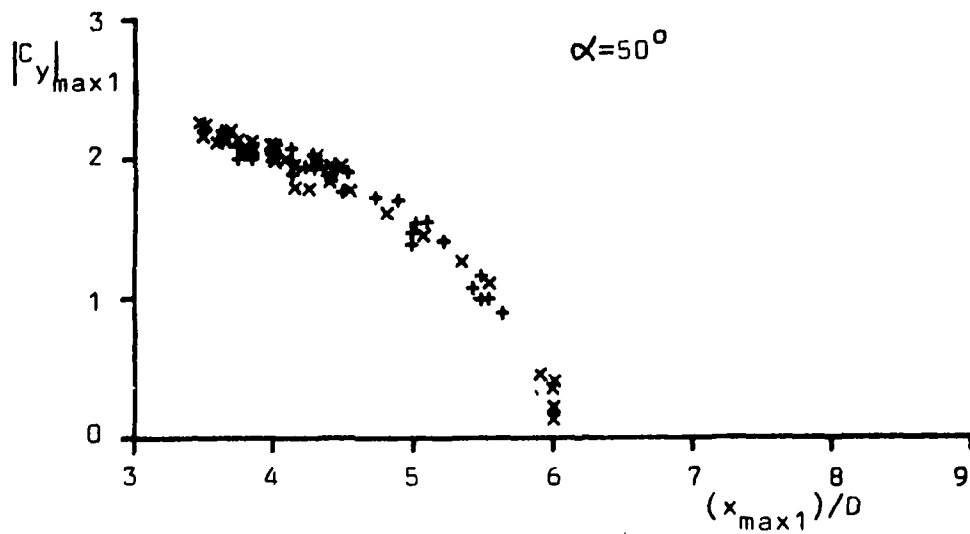
Figure 40



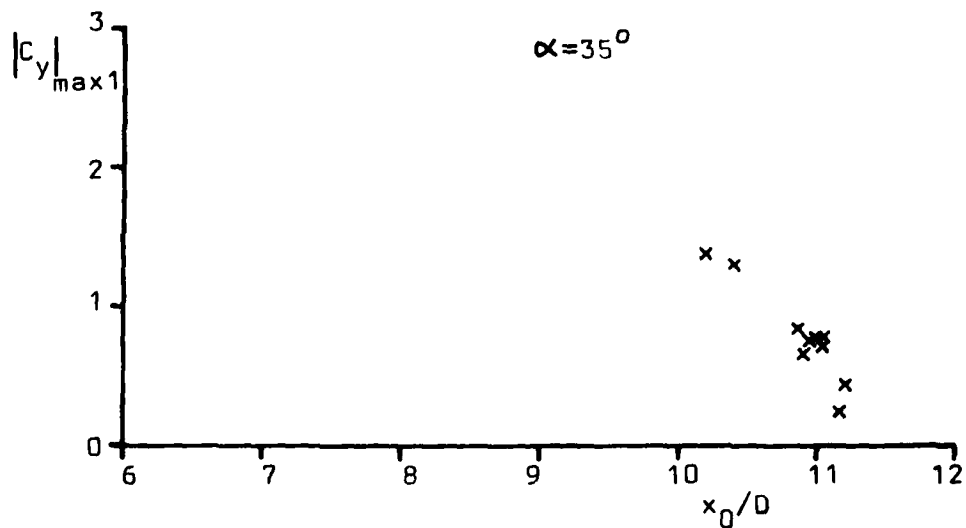
Correlation of Magnitude and Position of Maximum Side Force Coefficients.



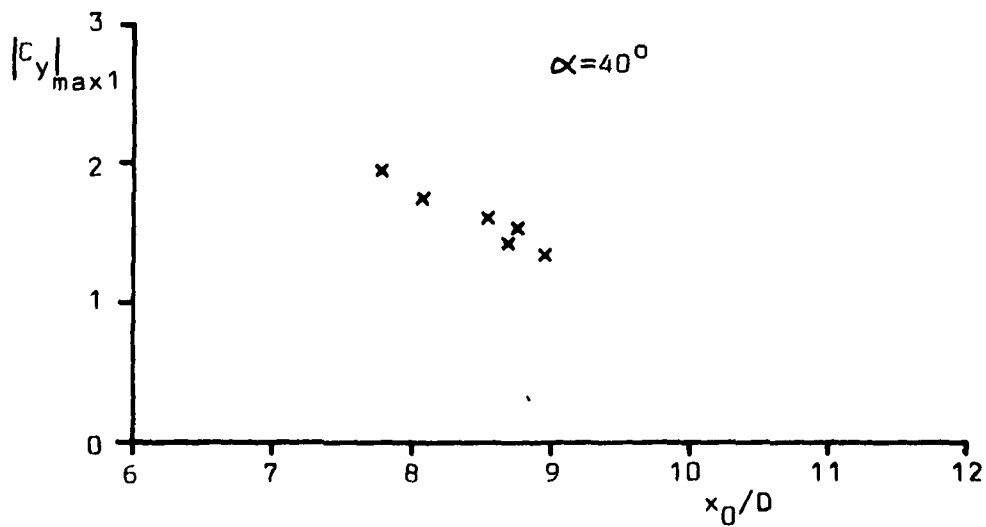
+ New Nose
x Old Nose



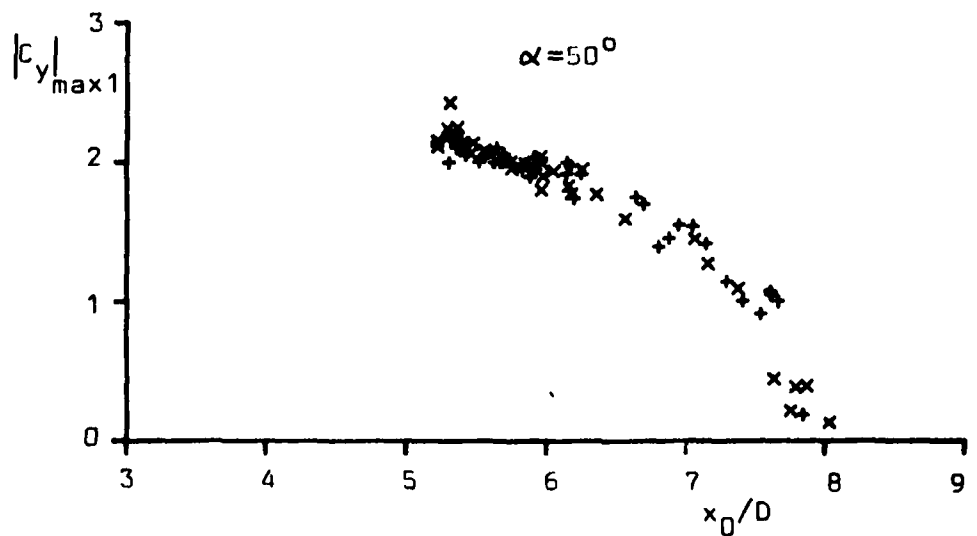
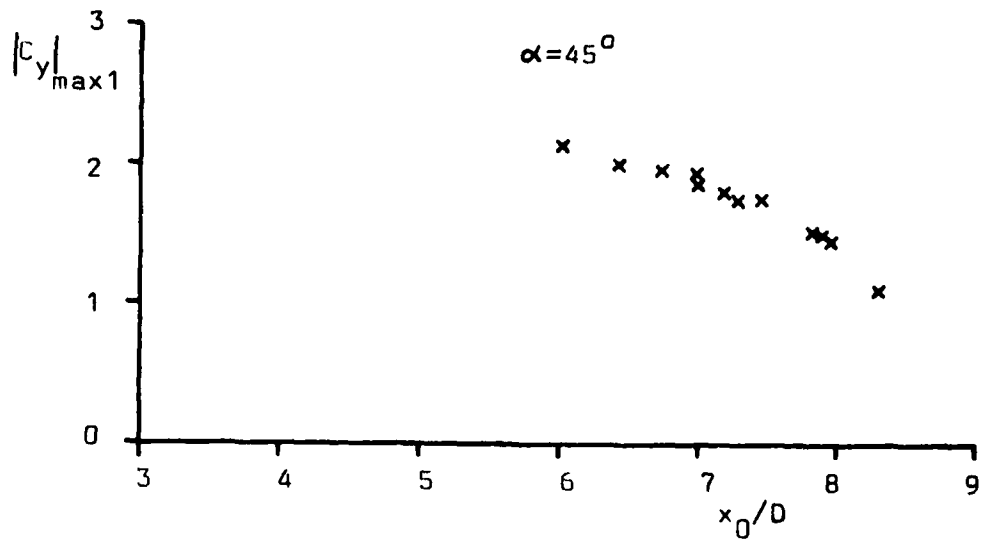
Correlation of Magnitude and Position of Maximum Side Force Coefficients.



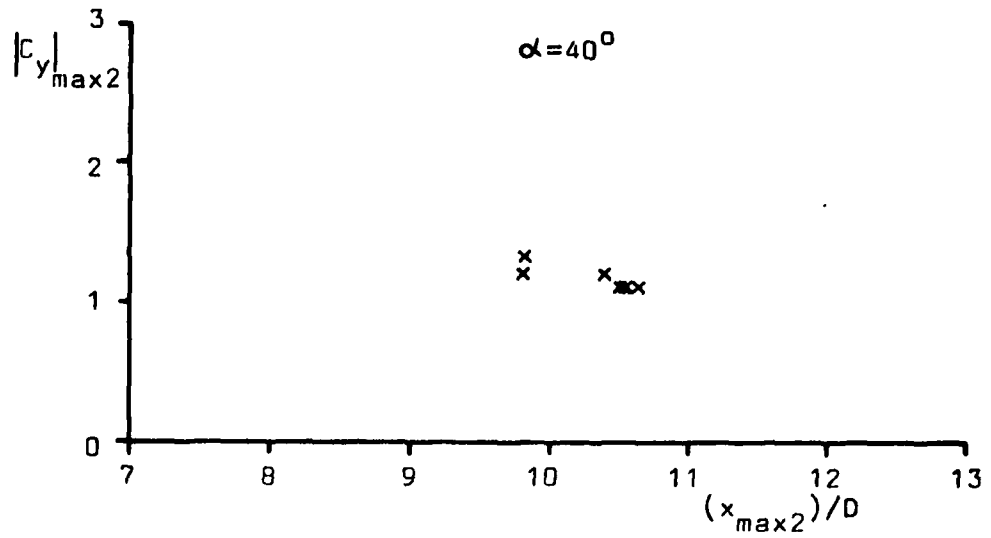
x Old Nose



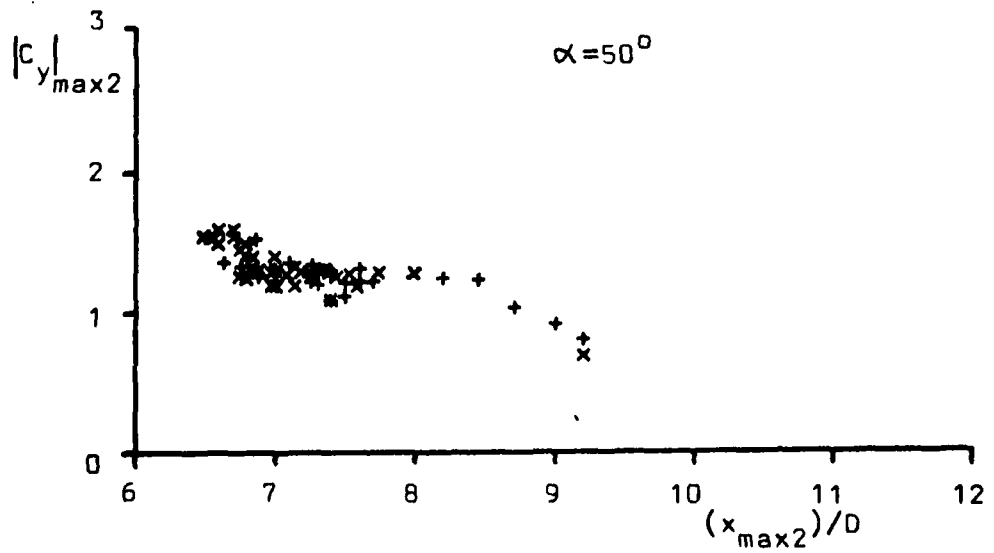
Correlation of Node Position with Magnitude of Maximum Side Force Coefficients.



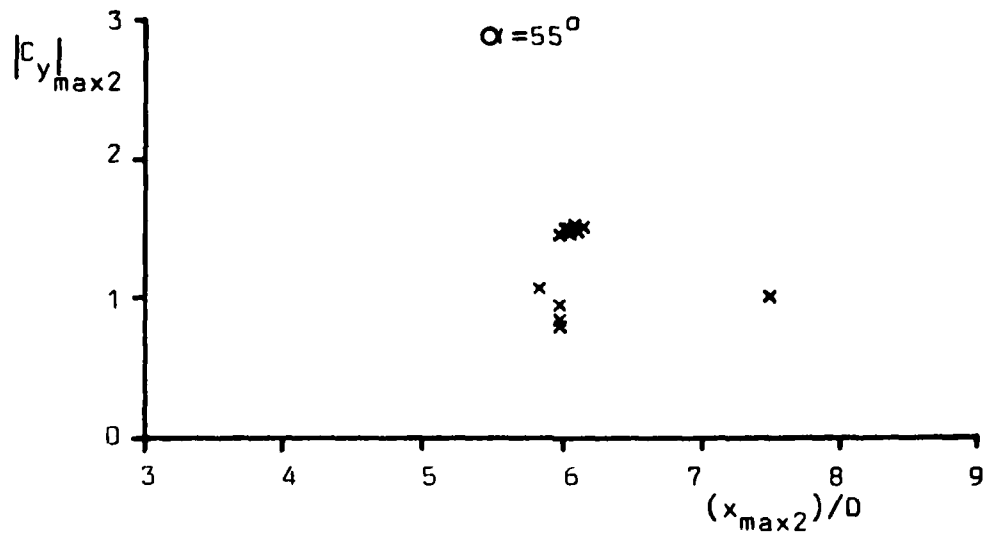
Correlation of Node Positions with Magnitudes of Maximum Side Force Coefficients.



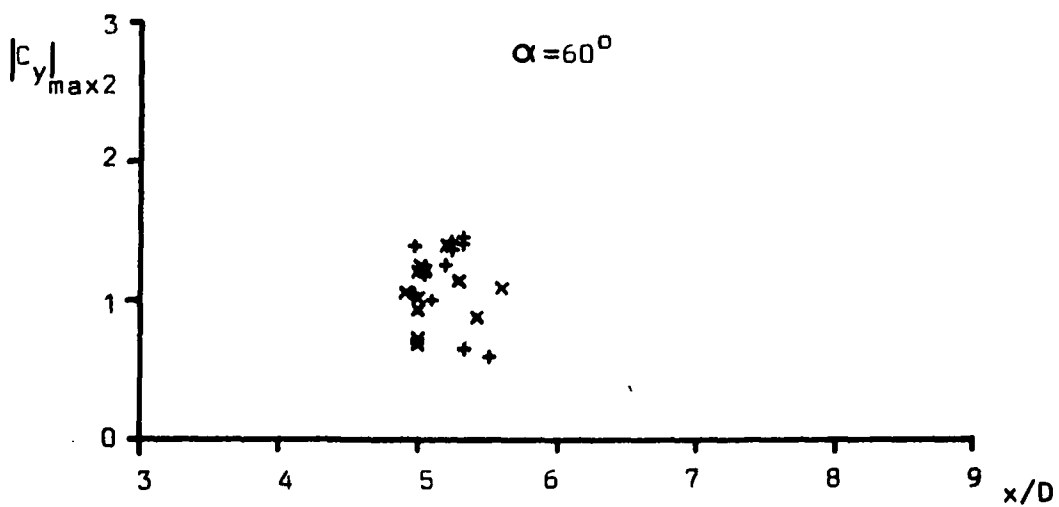
+ New Nose
x Old Nose



Correlation of Magnitude and Position of Maximum Side Force Coefficients:-Second Half-Cycle.

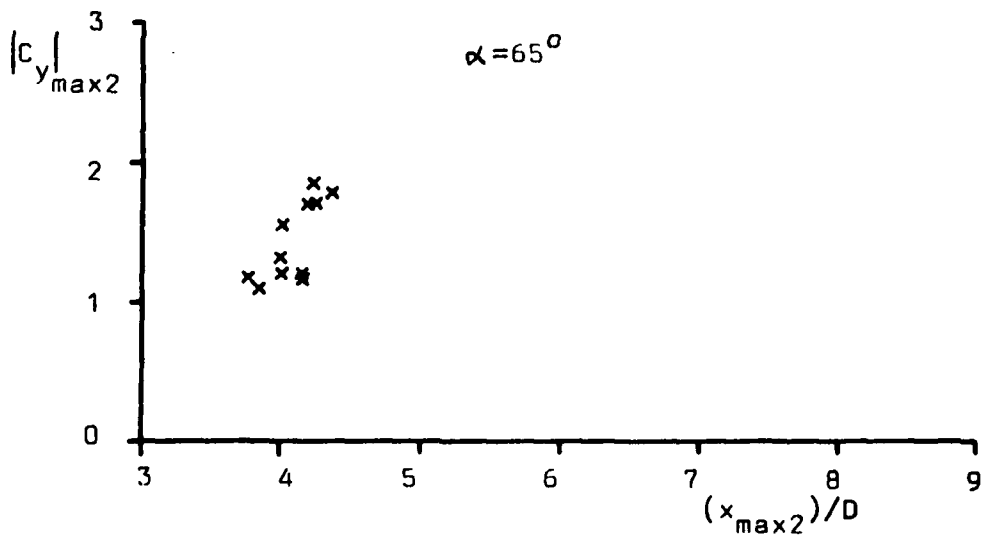


+ New Nose
x Old Nose

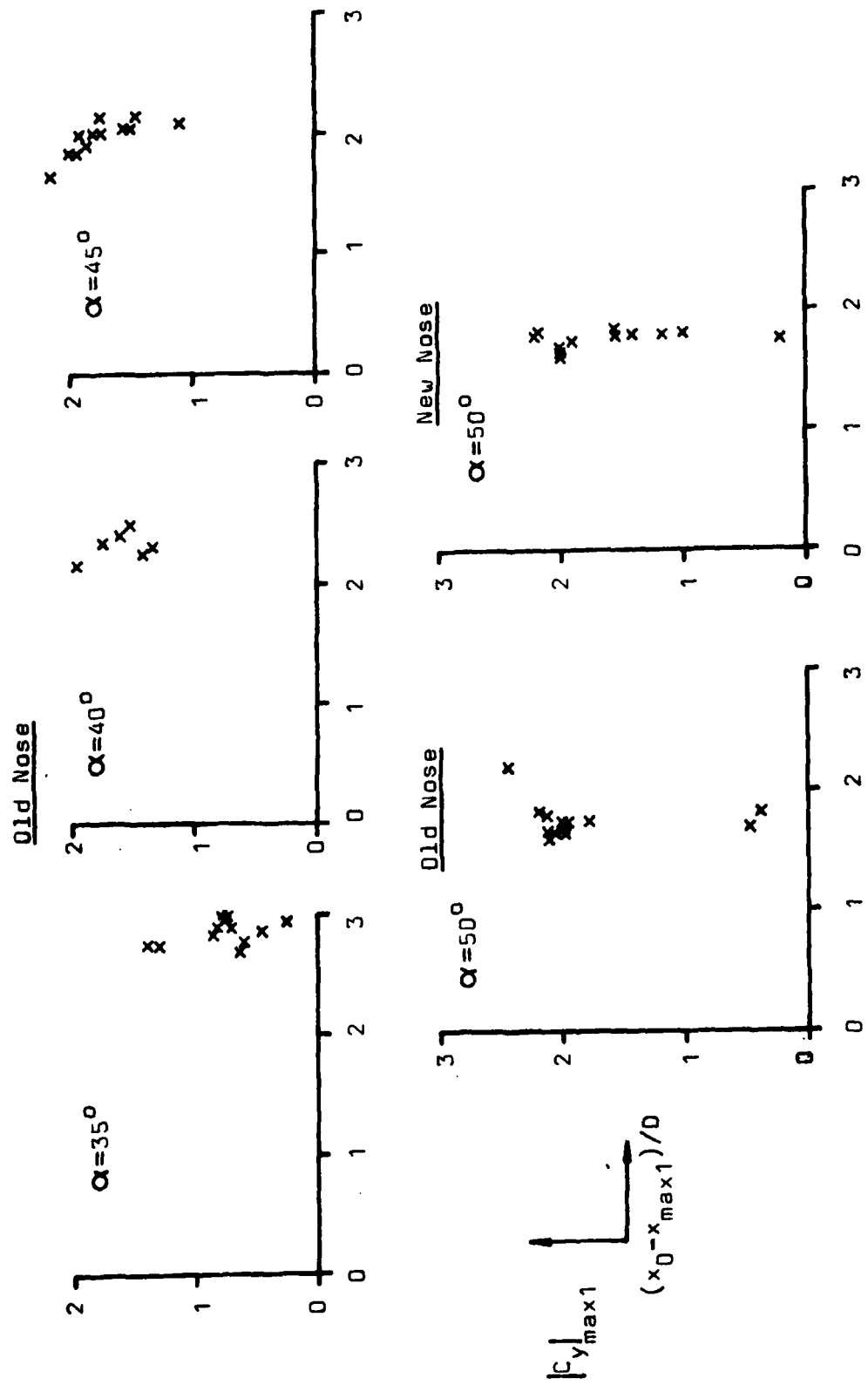


Correlation of Magnitude and Position of Maximum Side Force Coefficients:-Second Half-Cycle.

Figure 46

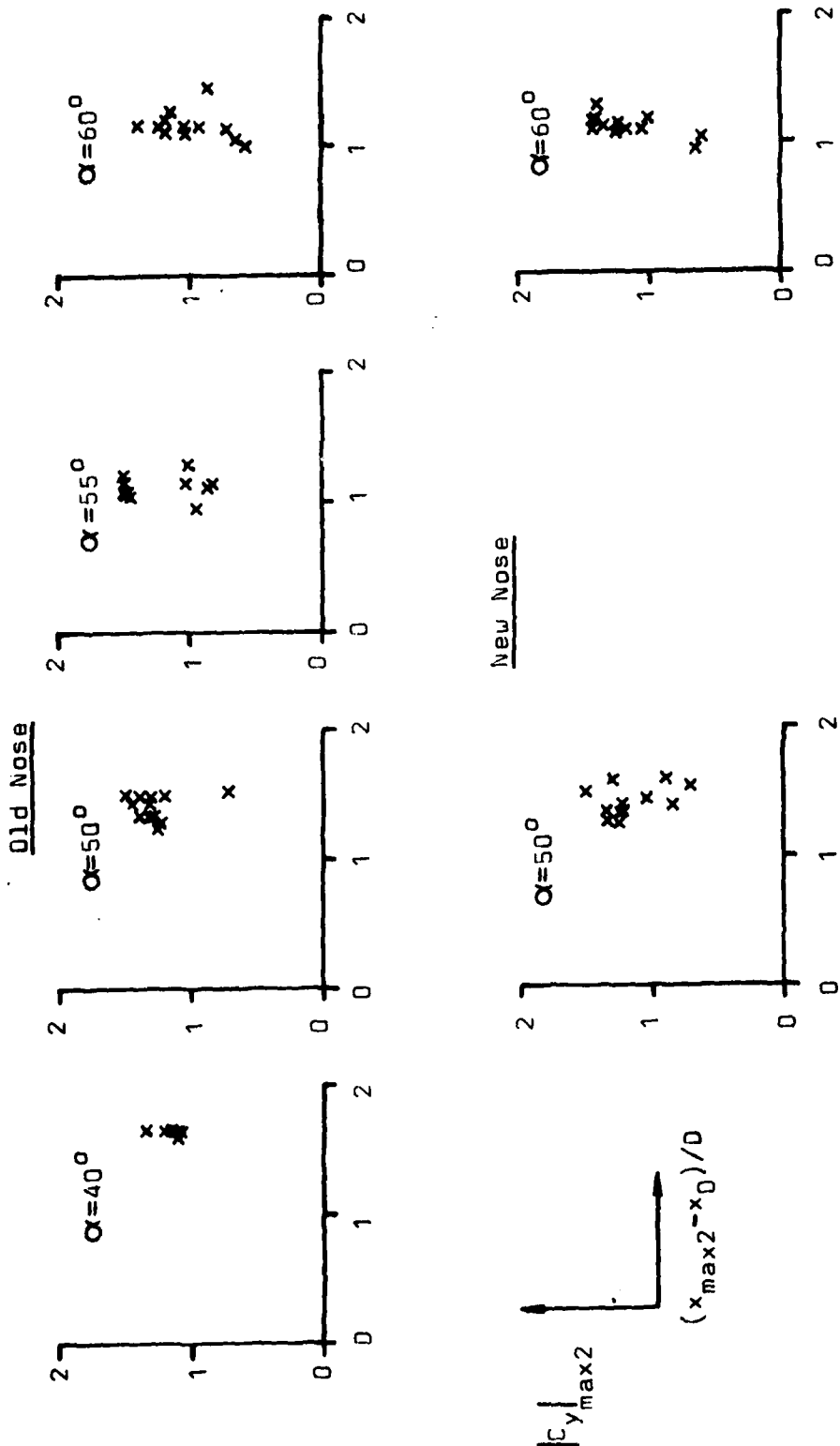


Correlation of Magnitude and Position of Maximum Side Force Coefficients:-Second Half-Cycle.



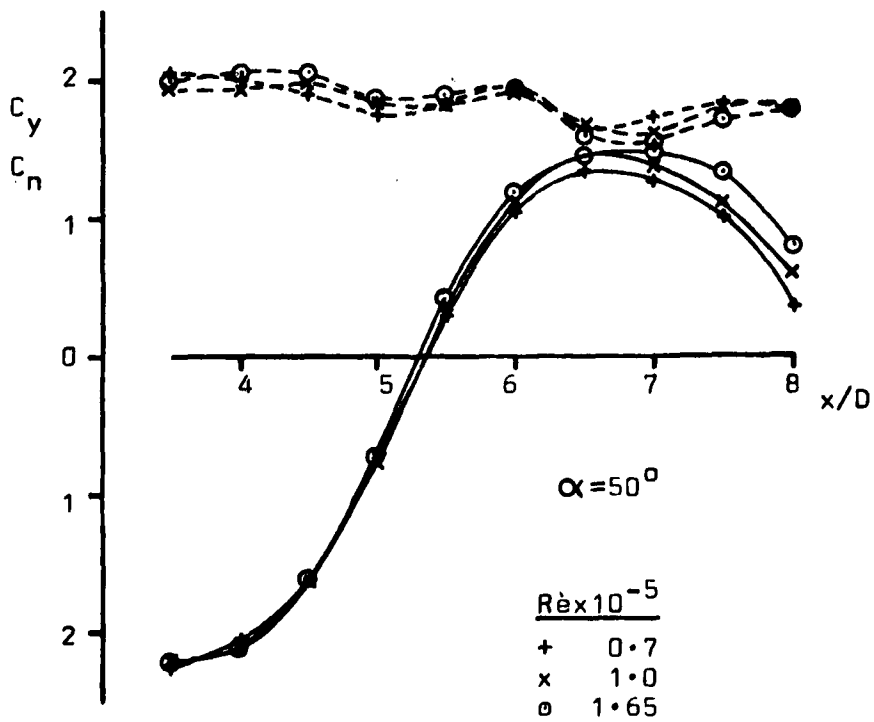
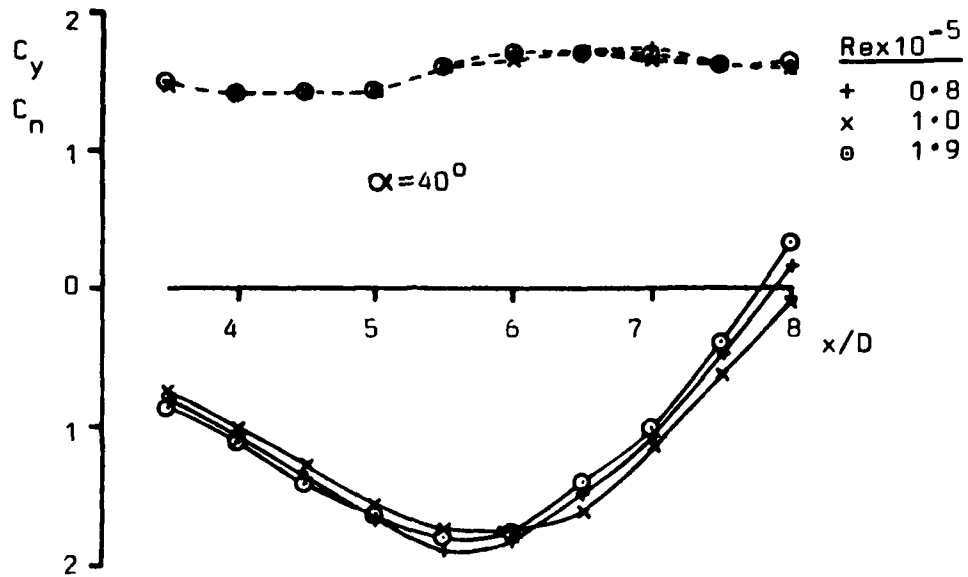
Correlation of Local Side Force First Peak Magnitudes with Distance Between the First Peaks and the Node Points.

Figure 48



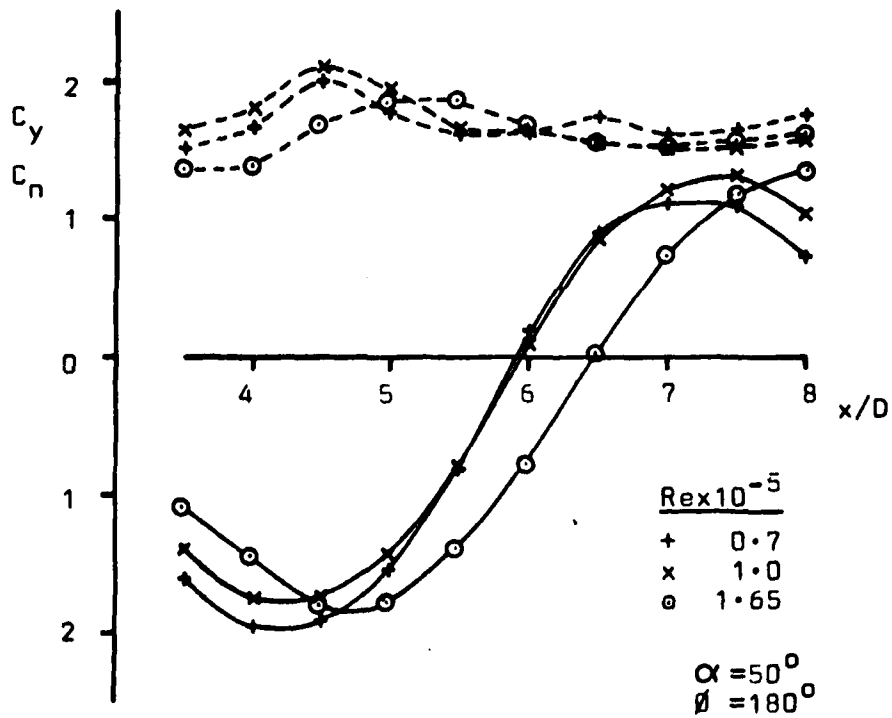
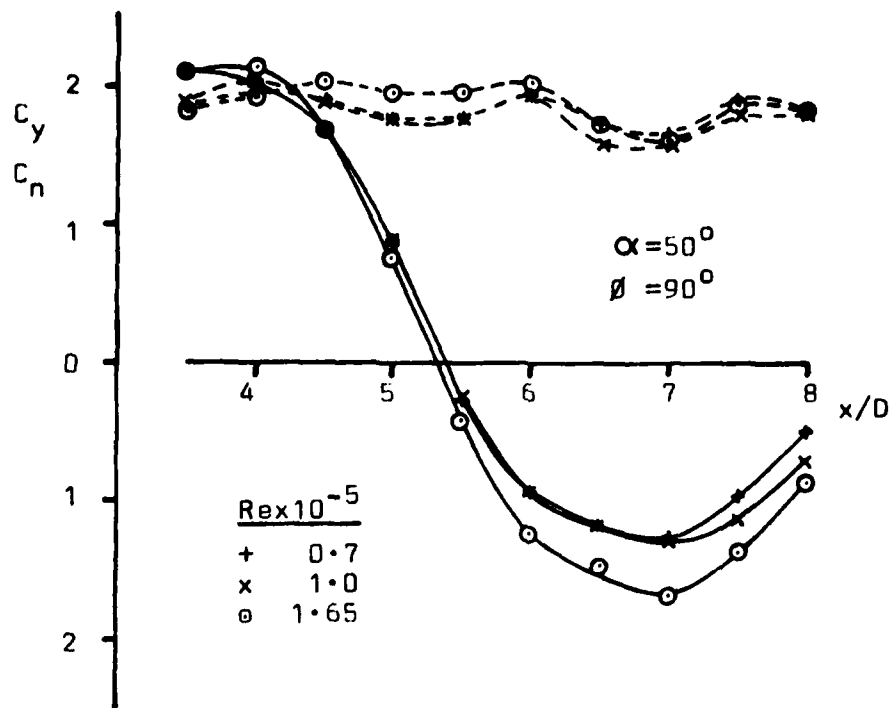
Correlation of Local Side Force Second Peak Magnitudes with Distance Between the Second Peaks and the Node Points.

Figure 49



Effect of Reynolds Number on Local Force Coefficients.
Old Nose 0° Roll Angle.

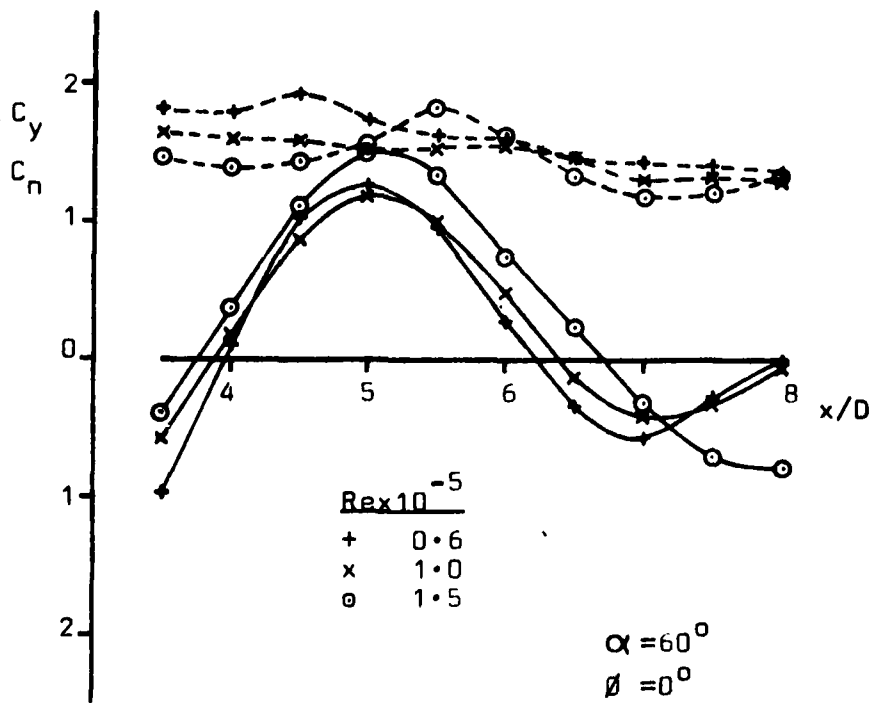
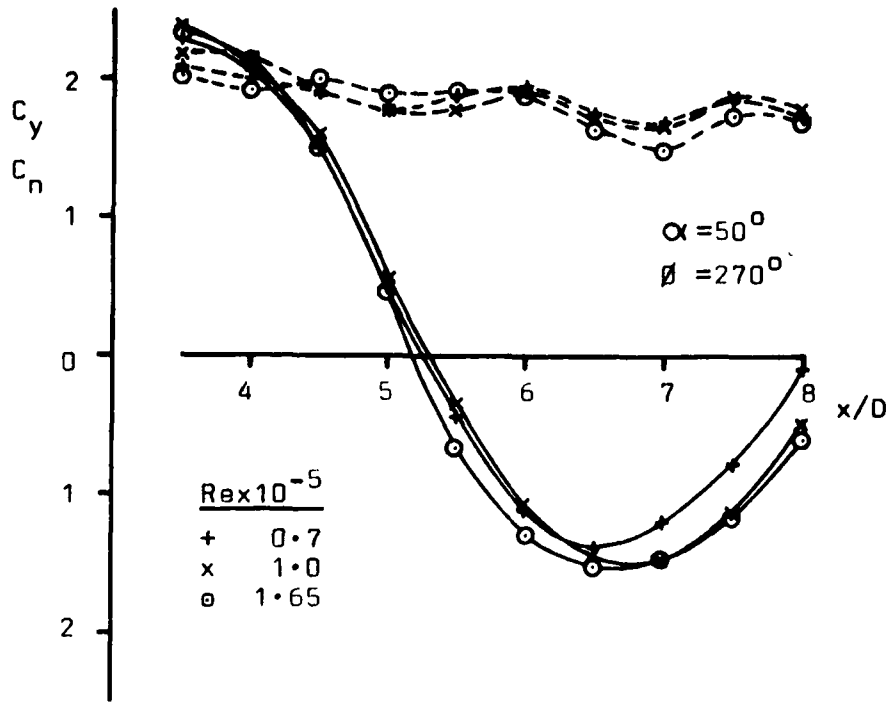
Figure 50



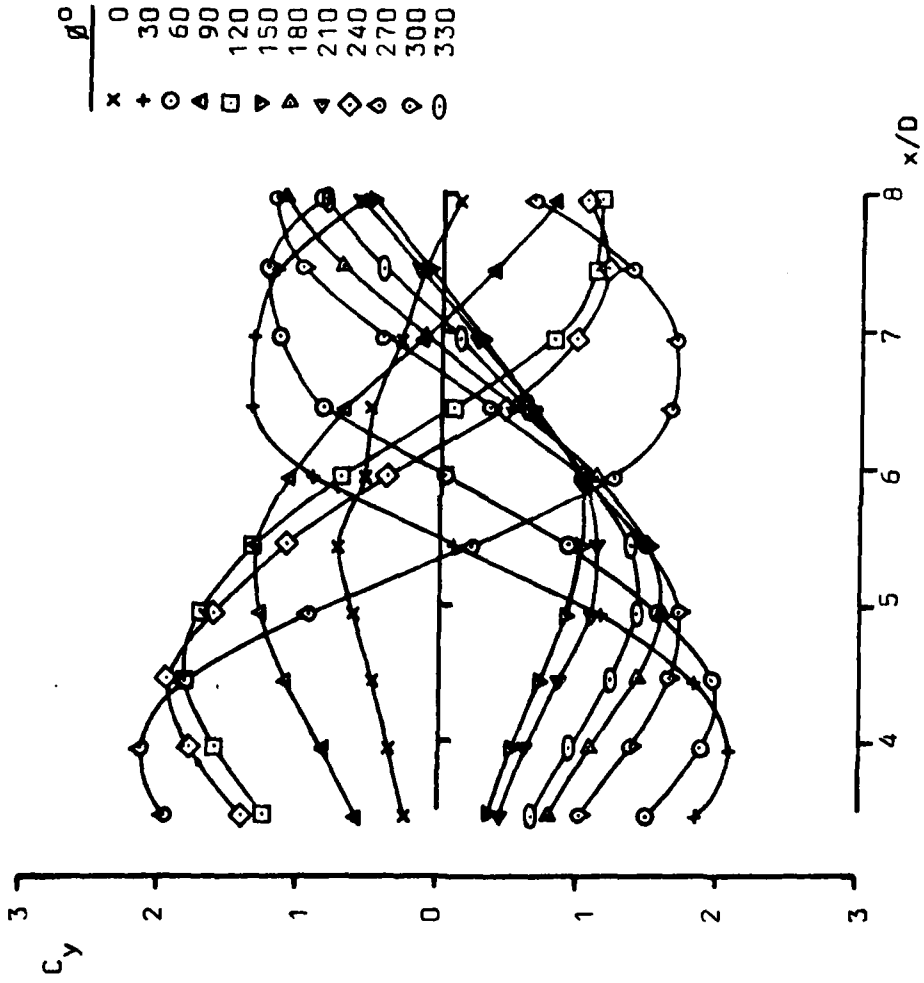
Effect of Reynolds Number on Local Force Coefficients.

Old Nose

Figure 51

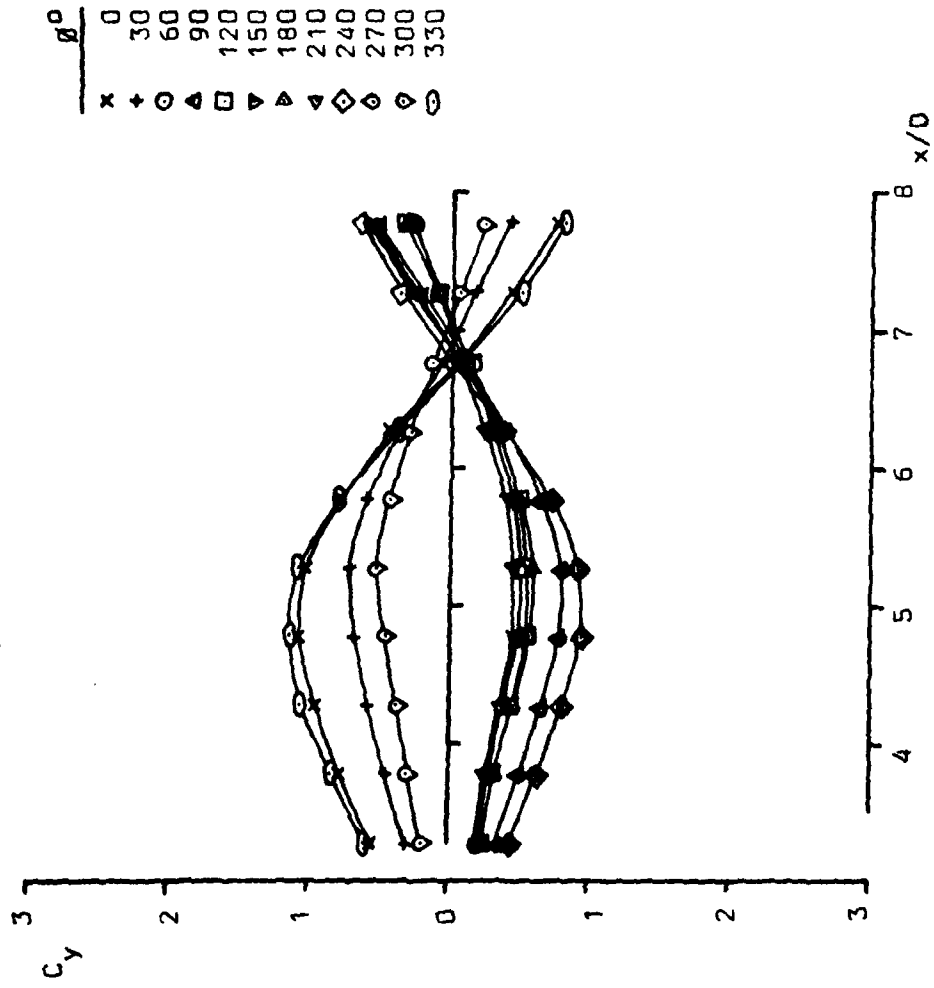


Effect of Reynolds Number on Local Force Coefficients.
 Old Nose



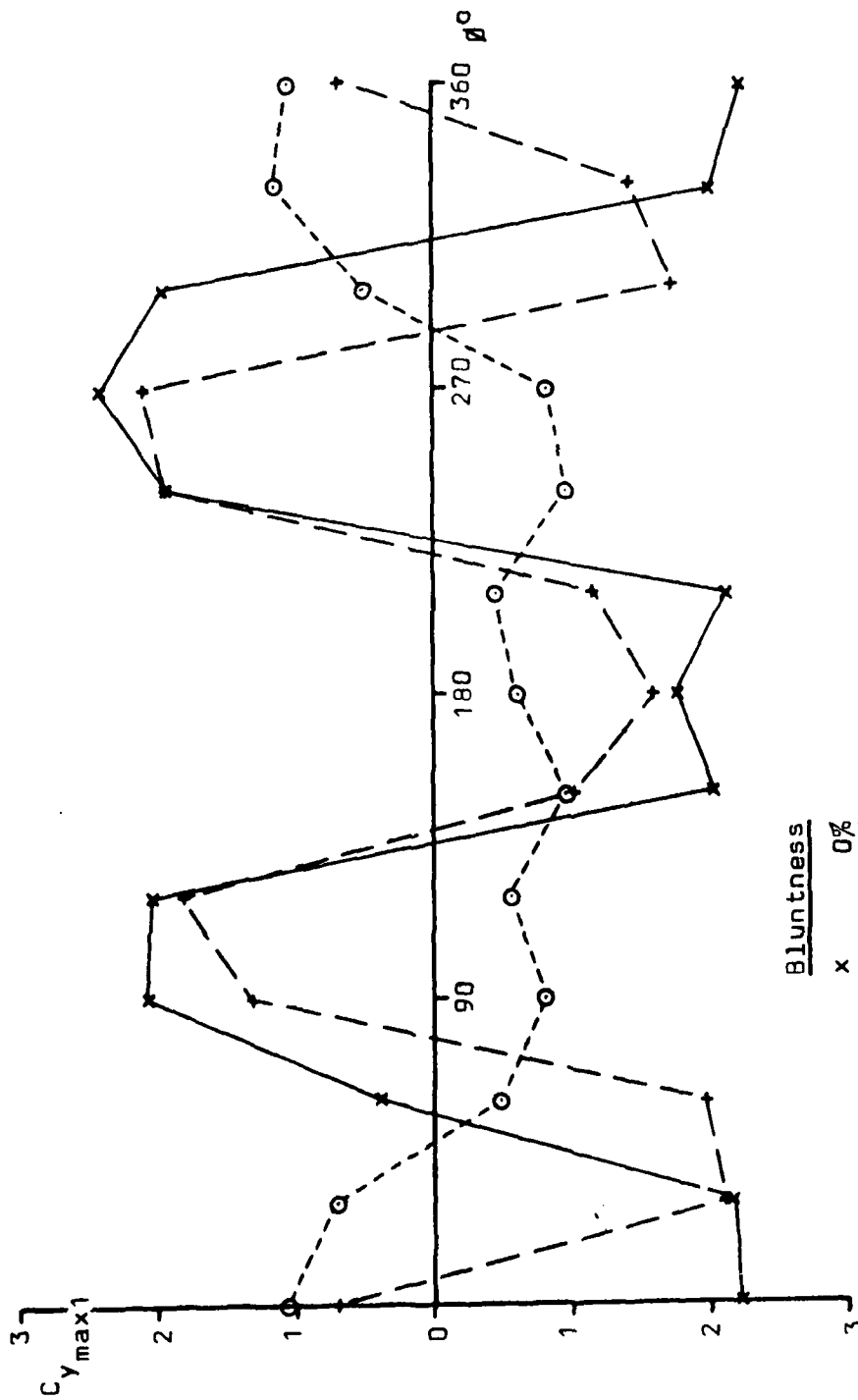
Distribution of Local Side Force Coefficients
 5% Blunted Three Calibre Ogive Nose 50° Incidence $Re=10^5$

Figure 53



Distribution of Local Side Force Coefficients
 20%-Blunted Three Calibre Ogive Nose 50° Incidence $Re=10^5$

Figure 54



Bluntness

- x 0%
- + 5%
- o 20%

Roll Angle Variation of Maximum Side Forces. 50° Incidence $Re=10^5$

Basic Three Calibre Ogive Nose

AD-A113 183

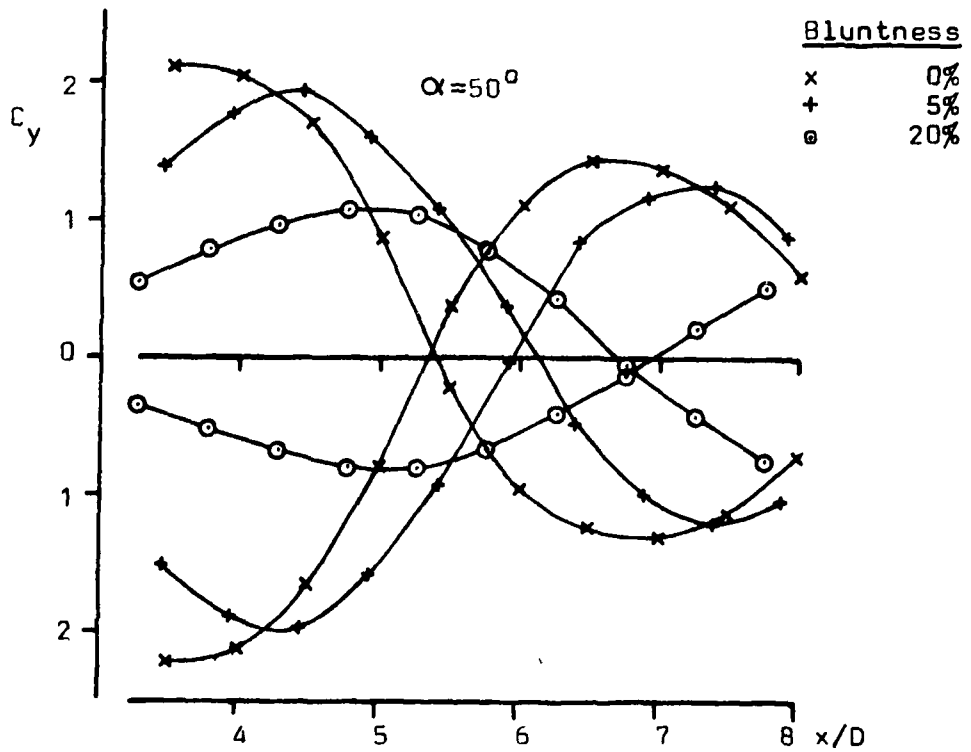
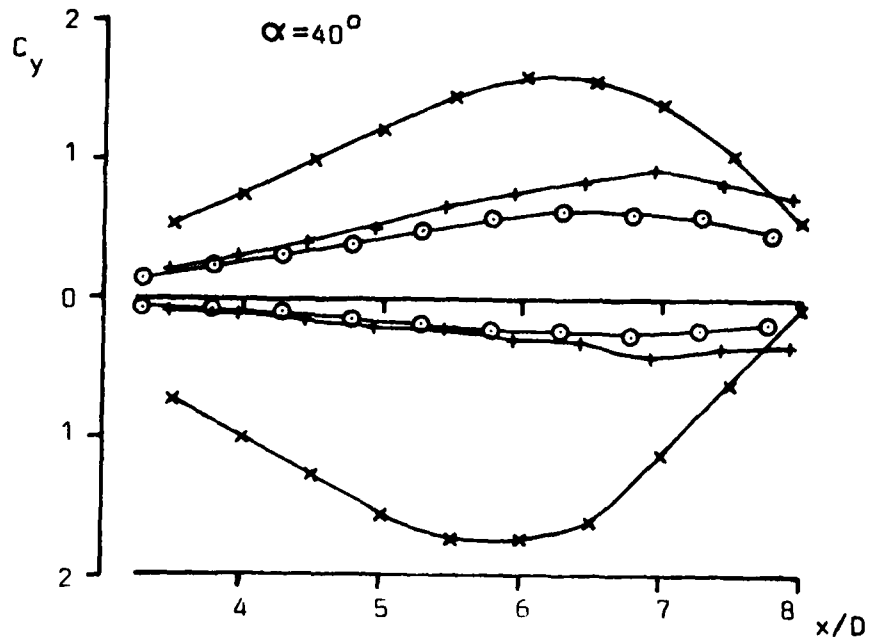
BRISTOL UNIV (ENGLAND) DEPT OF AERONAUTICAL ENGINEERING F/6 28/4
PRESSURES ON A SLENDER, AXISYMMETRIC BODY AT HIGH ANGLE OF ATTA--ETC(U)
JAN 82 P C DEXTER, J W FLOWER DAJAS7-81-C-0082
BLH/PCD8201 NL

UNCLASSIFIED

2 of 2
2000

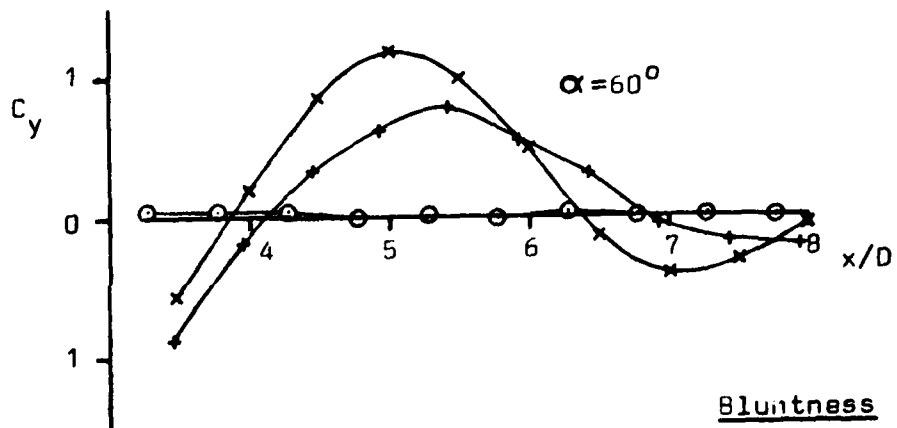
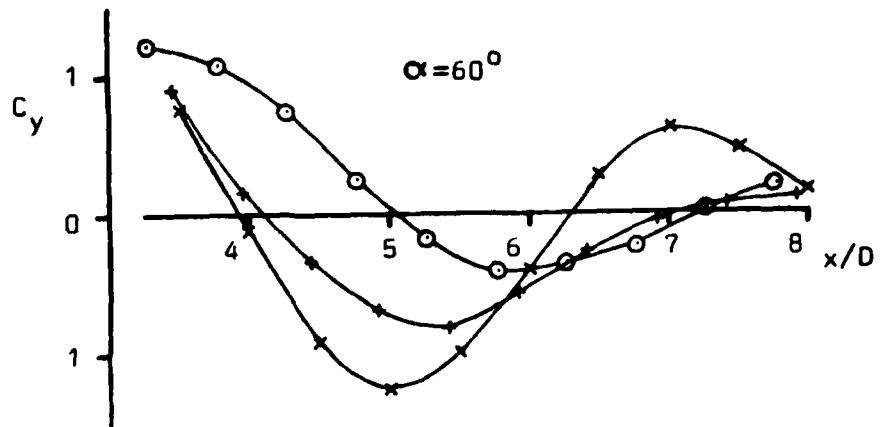


END
DATE
FILMED
5-82
DTIC



Distribution of Local Side Force Coefficients $Re=10^5$
 Basic Three Calibre Ogive Nose

Figure 56



Bluntness	
x	0%
+	5%
o	20%

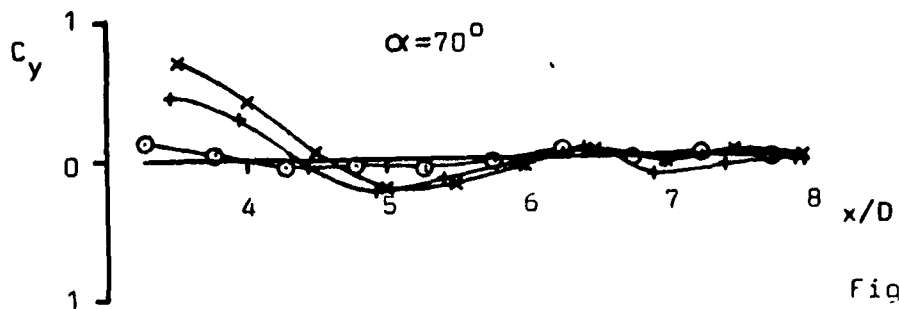
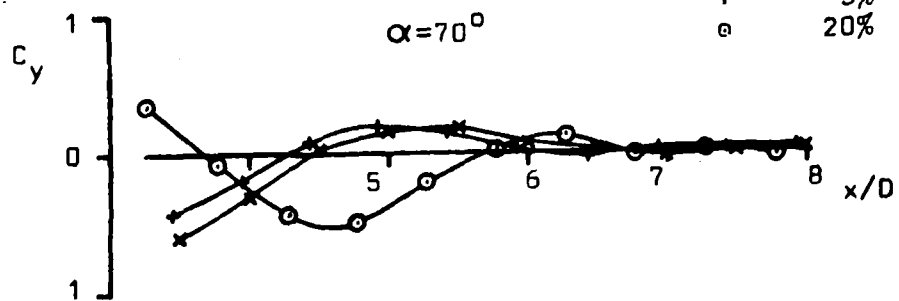
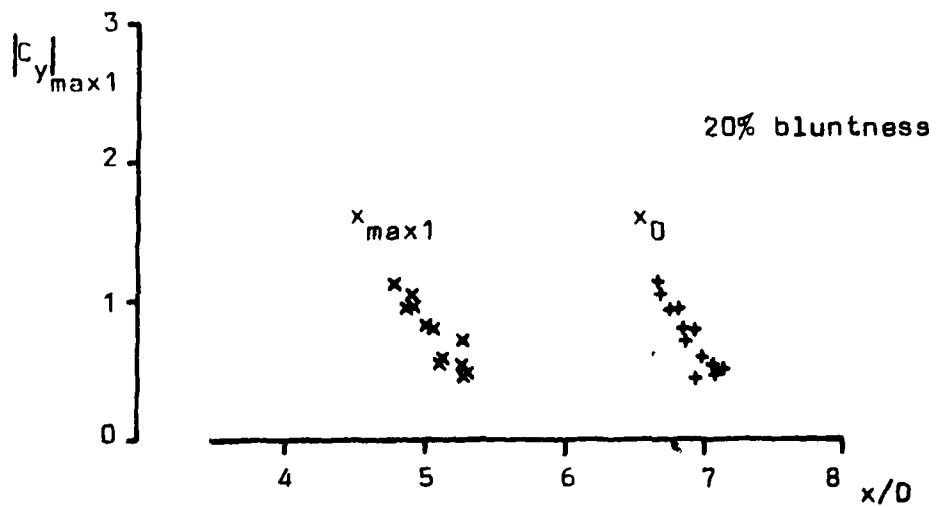
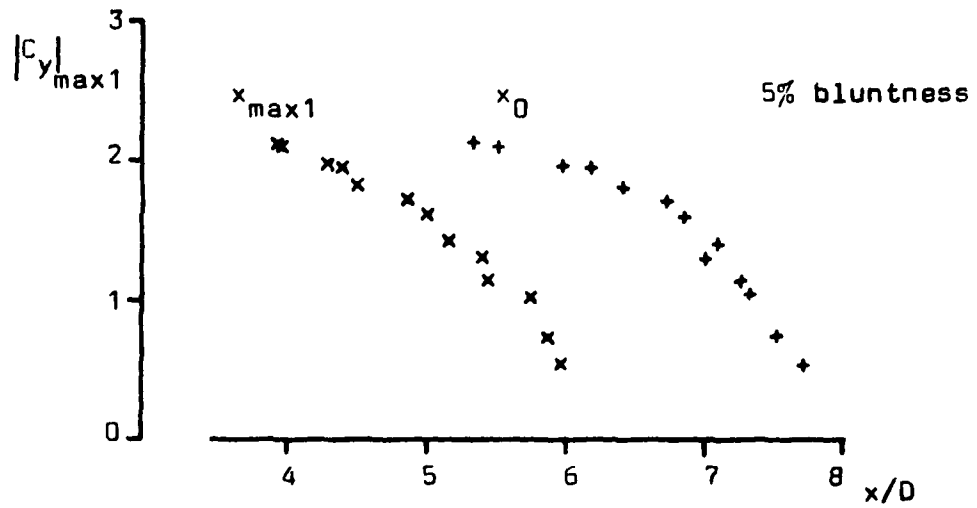
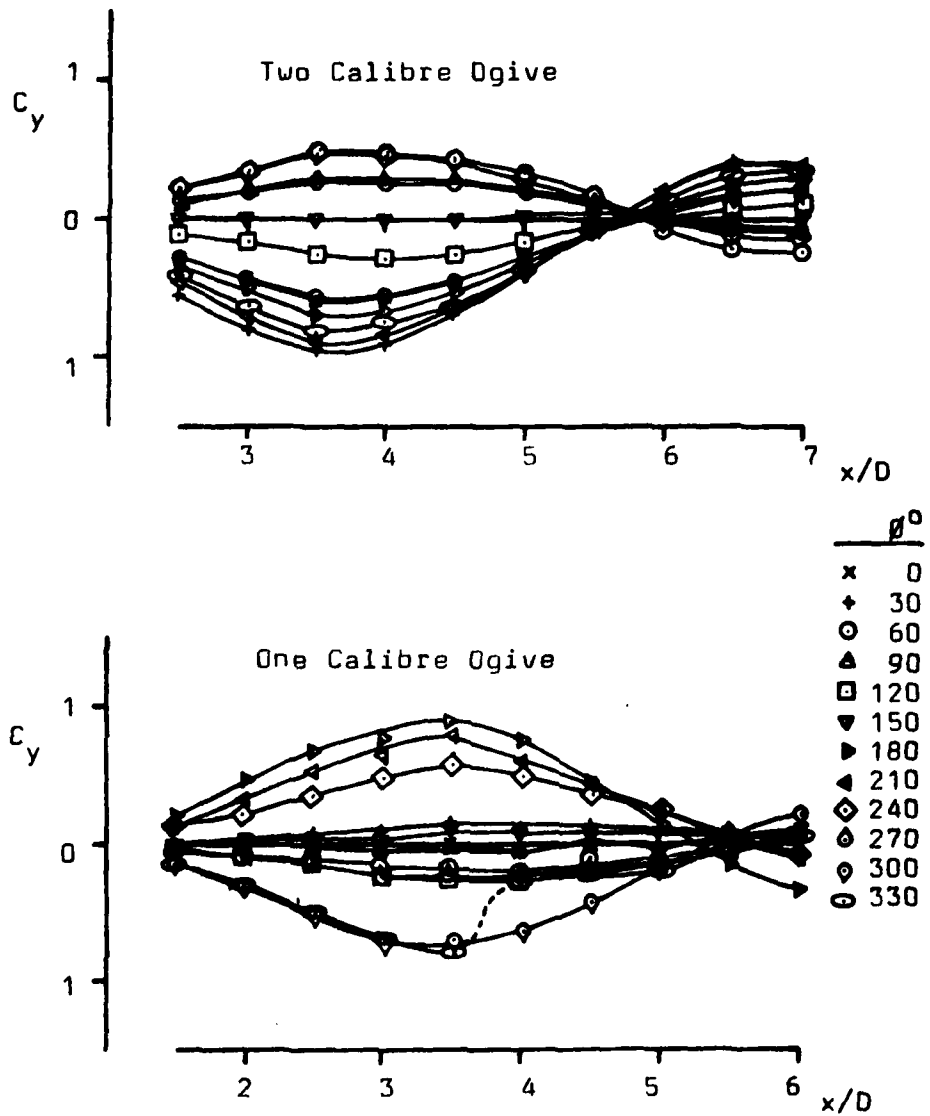


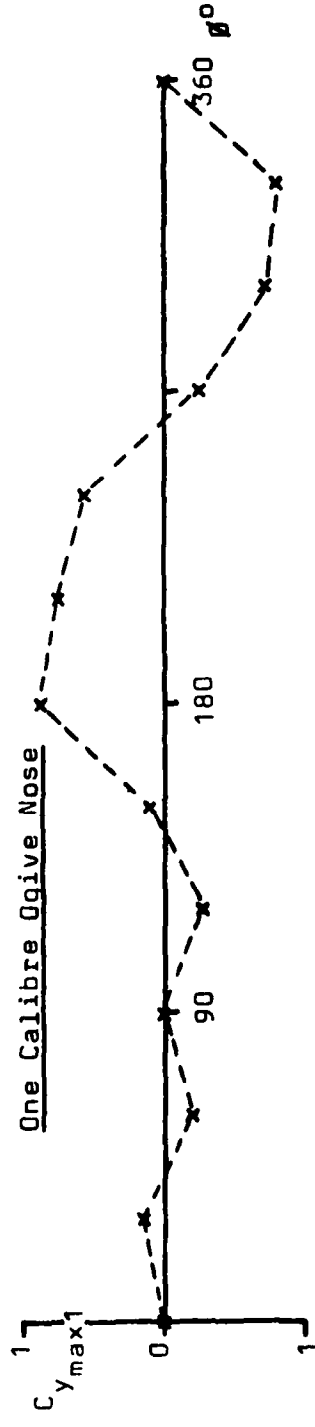
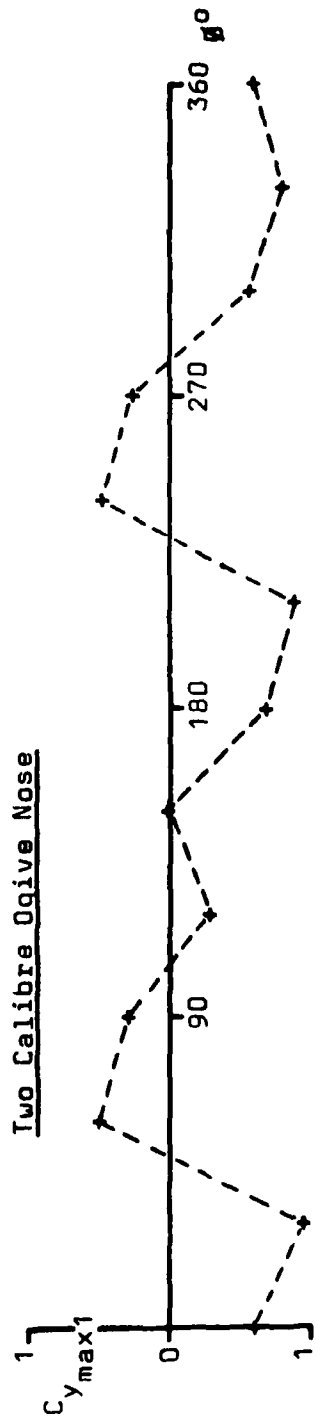
Figure 57
 Distribution of Local Side Force Coefficients
 Basic Three Calibre Ogive Nose $Re=10^5$



Correlation of Local Side Force First Peak Magnitudes
with Positions of Peaks and with Node Point Positions
Basic Three Calibre Ogive Nose 50° Incidence $Re=10^5$

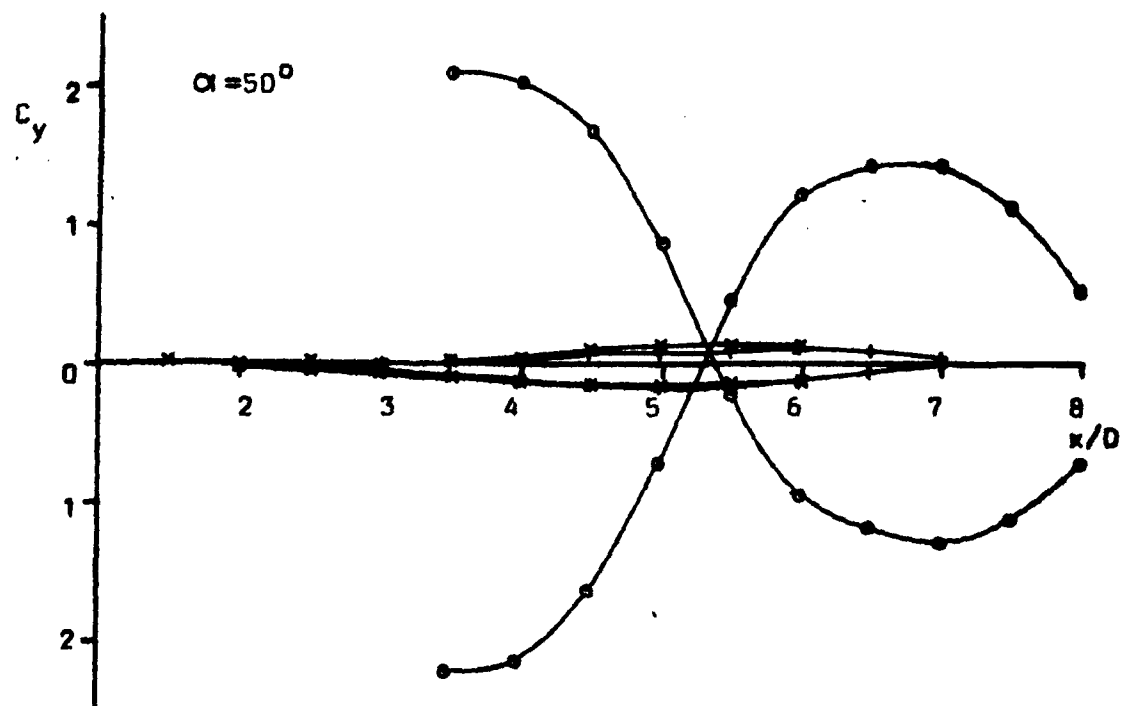
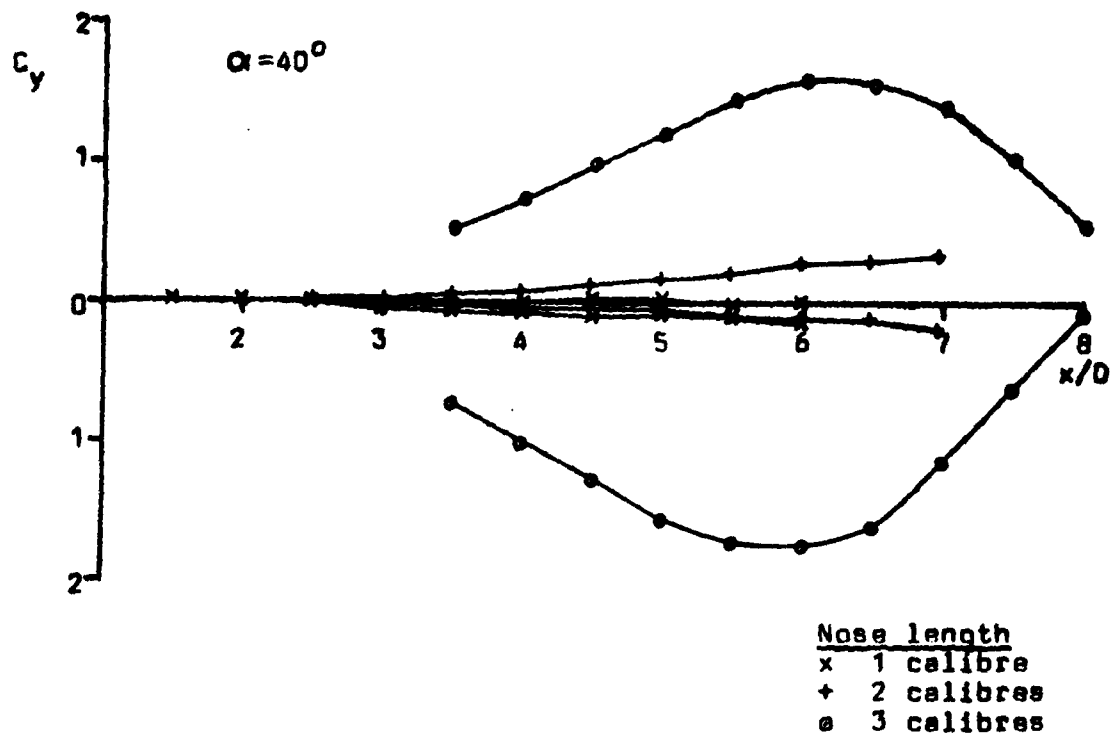


Distribution of Local Side Force Coefficients
 Ogive Noses 60° Incidence $Re=10^5$



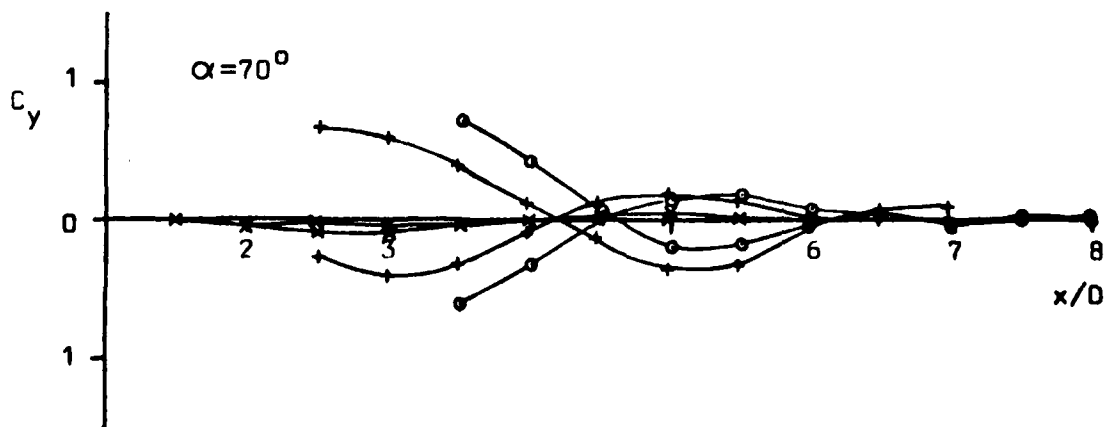
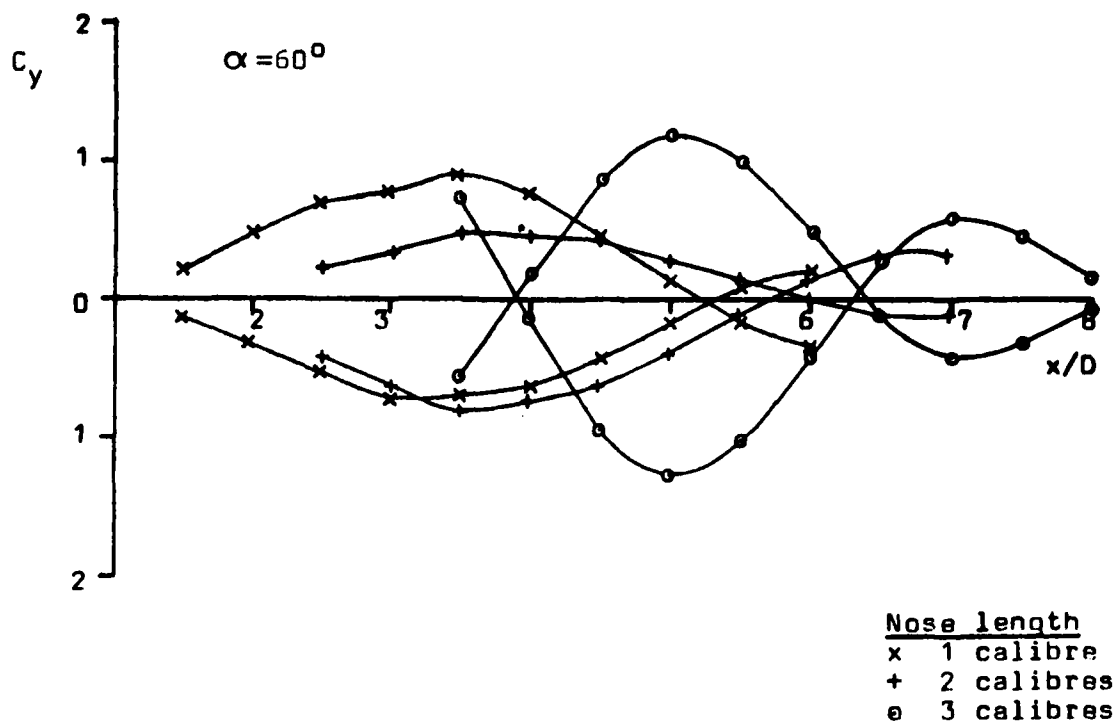
Roll Angle Variation of Maximum Side Forces 60° Incidence $Re=10^5$

Figure 60

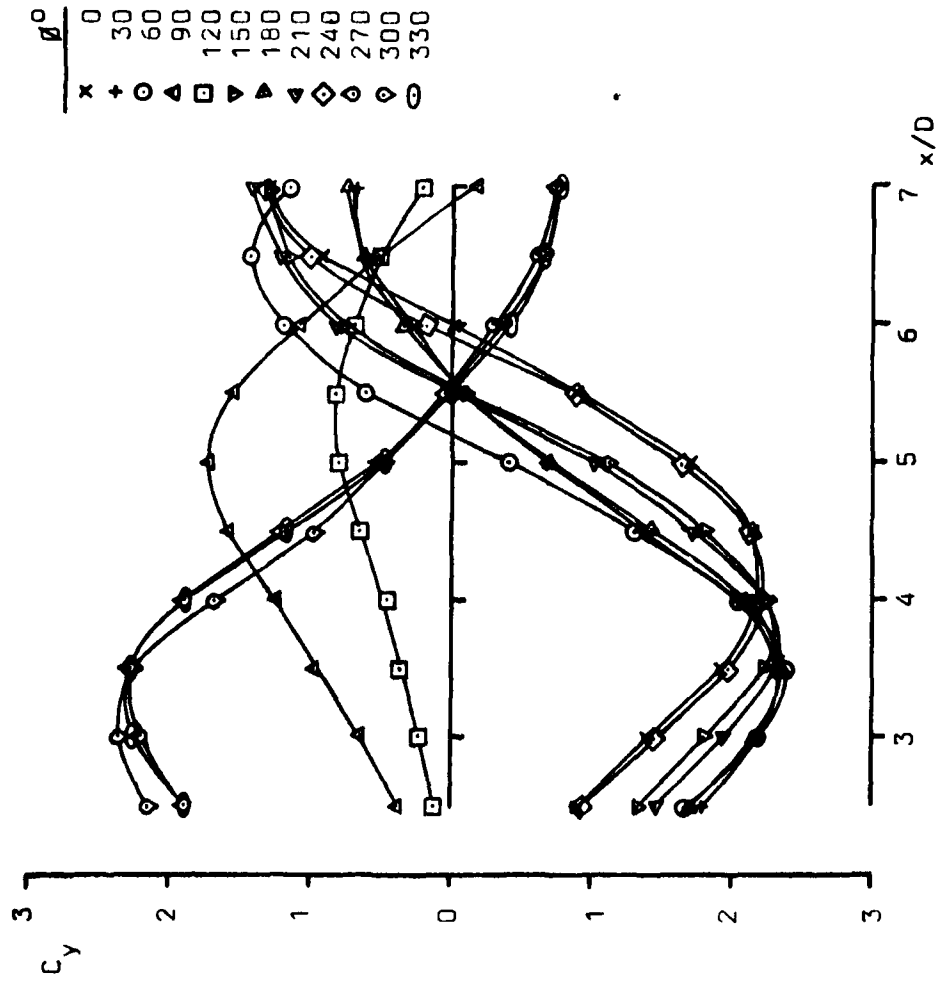


Distribution of Local Side force Coefficients $Re=10^5$
 Ogive Nose Shape.

Figure 61

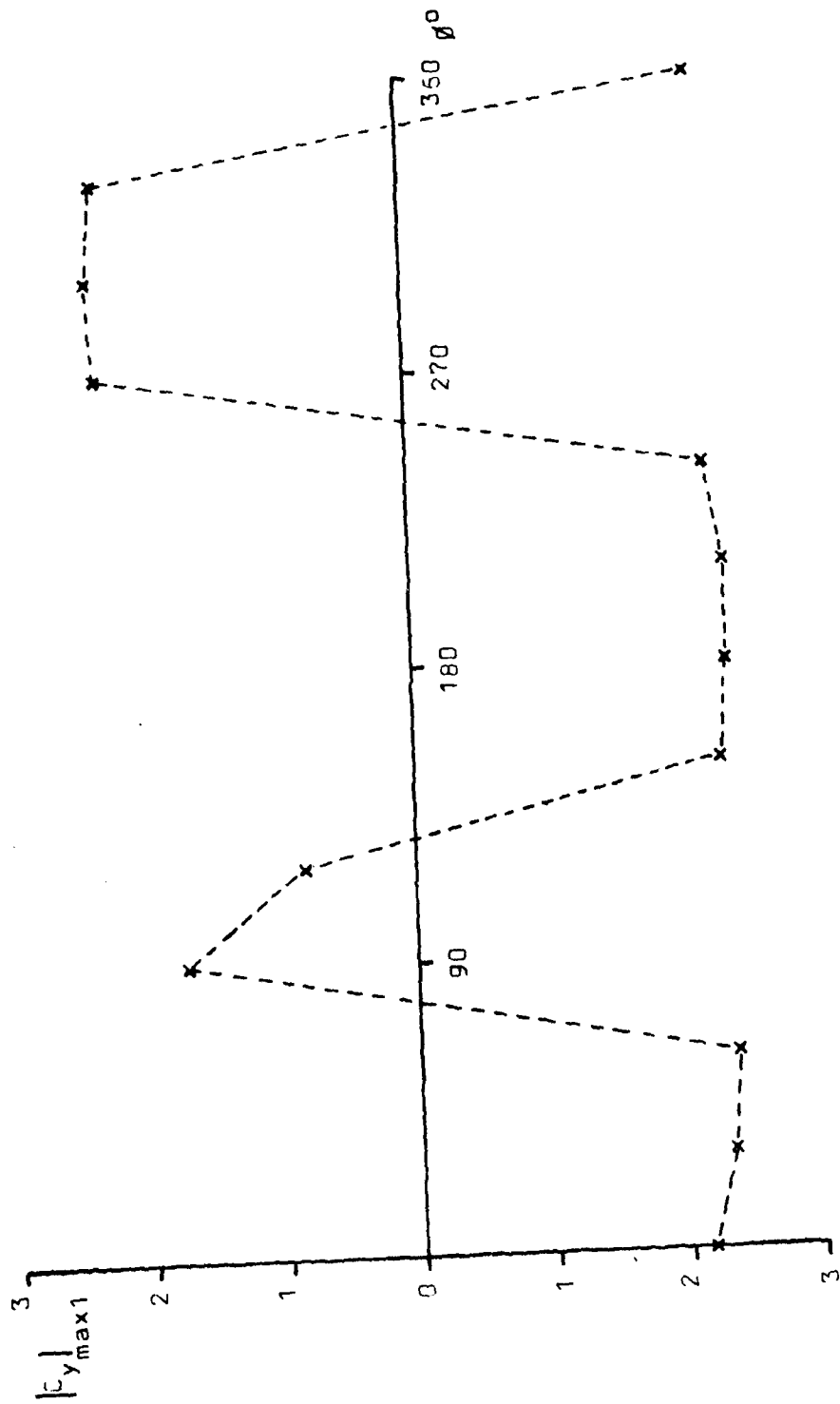


Distribution of Local Side Force Coefficients $Re=10^5$
Ogive Nose Shape.



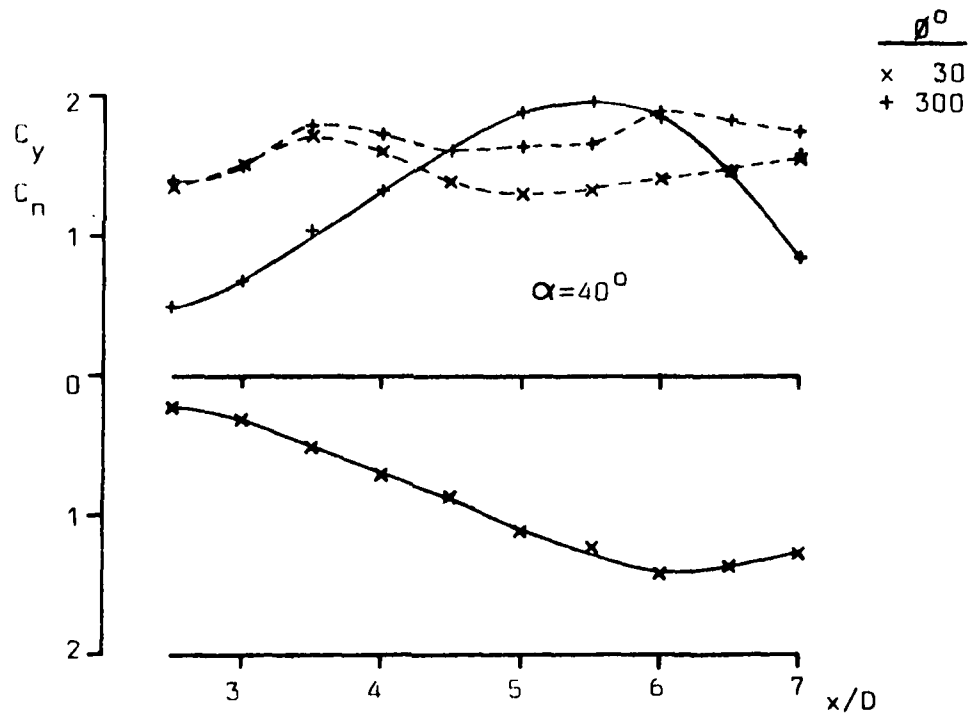
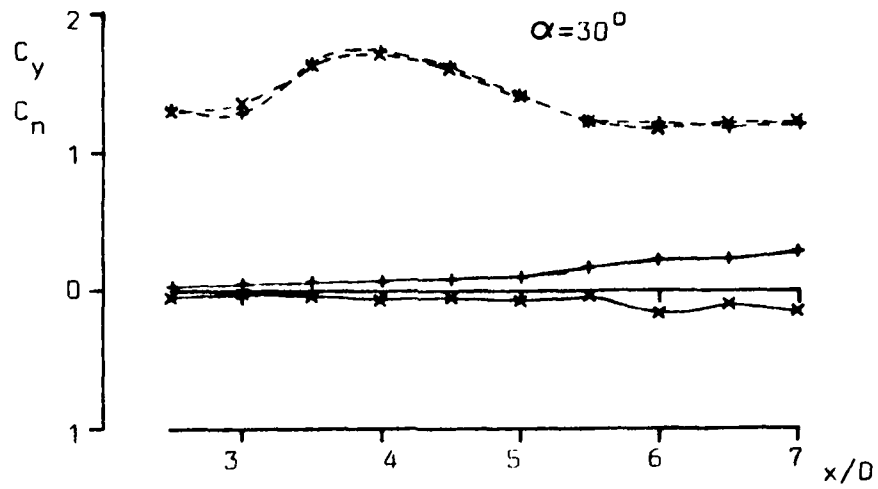
Distribution of Local Side Force Coefficients
 Two Calibre Cone Nose 50° Incidence Re=10⁵

Figure 63



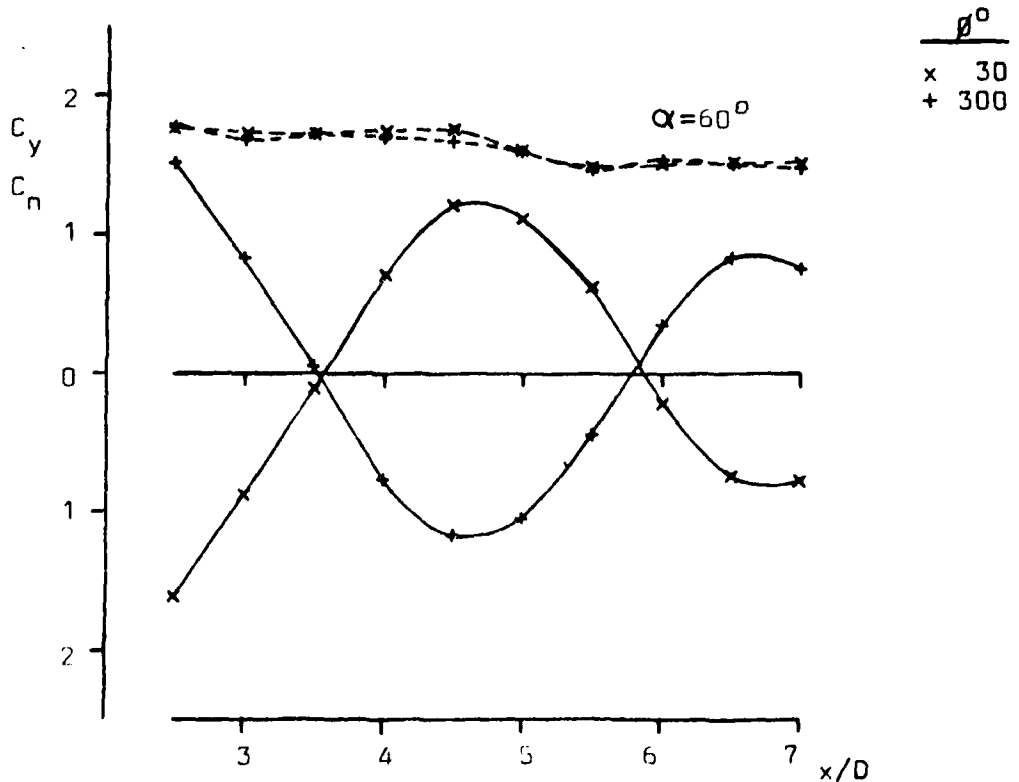
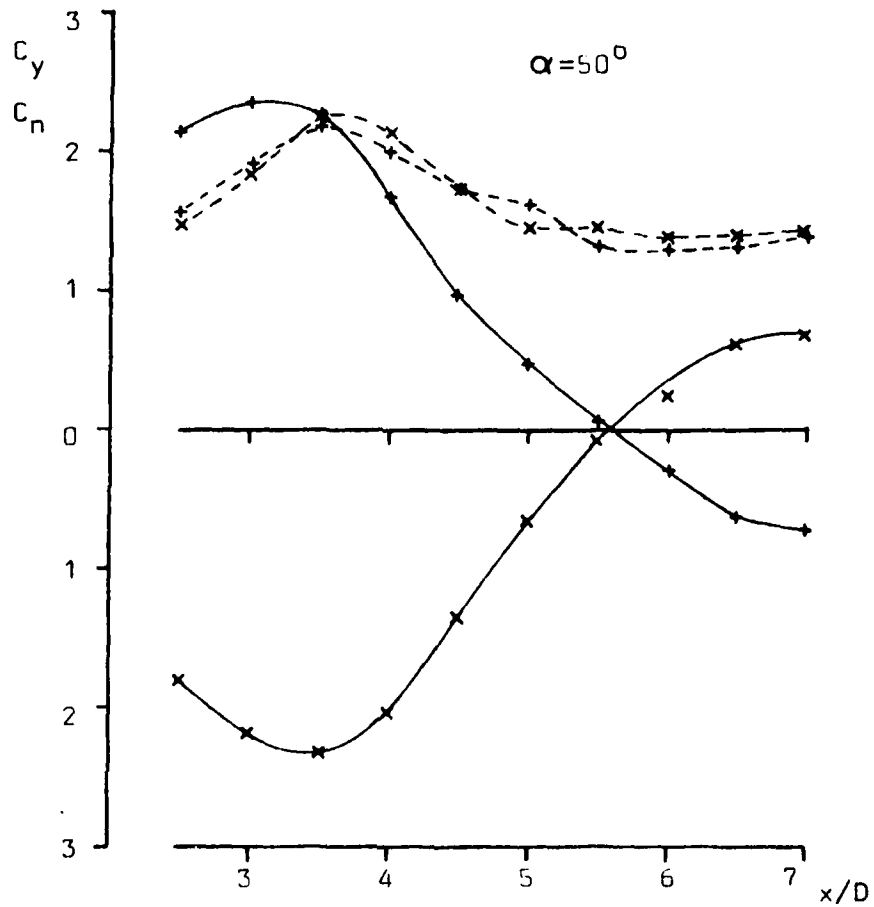
Roll Angle Variation of Maximum Side Forces
Two Calibre Cone Nose 50° Incidence $Re=10^5$

Figure 64



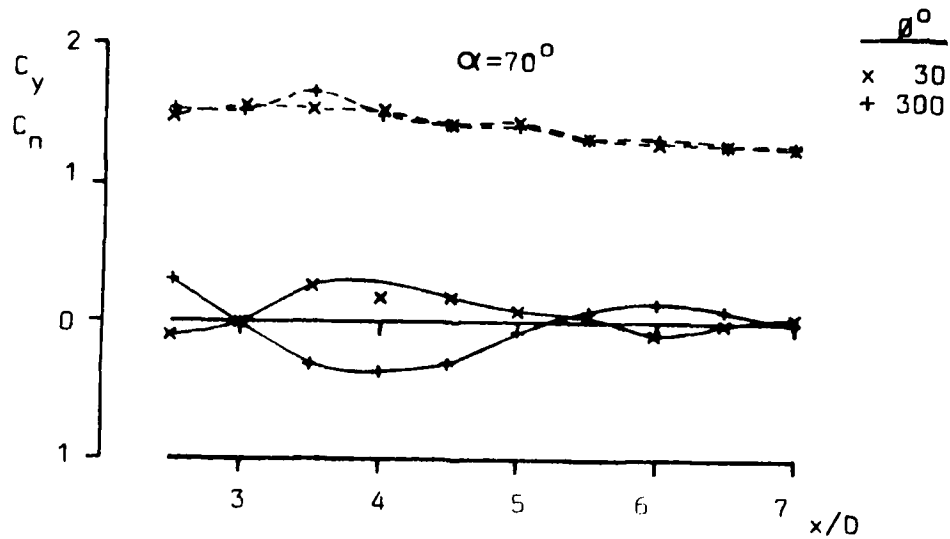
Distribution of Local Force Coefficients
 Two Calibre Cone Nose $Re=10^5$

Figure 65

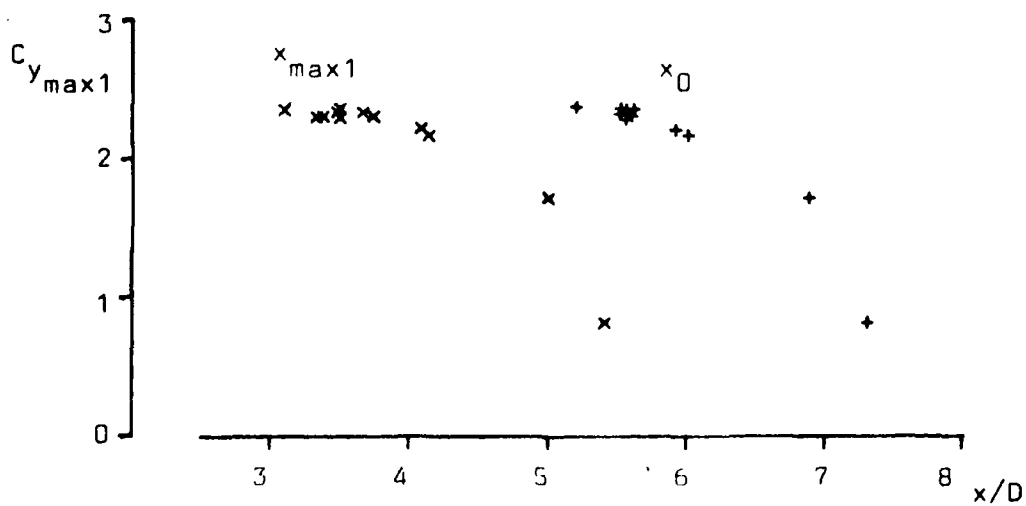


Distribution of Local Force Coefficients
Two Calibre Cone Nose $Re=10^5$

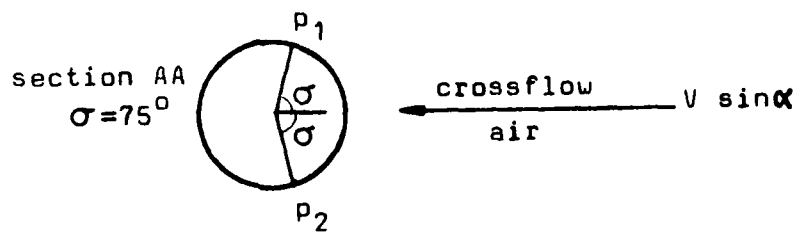
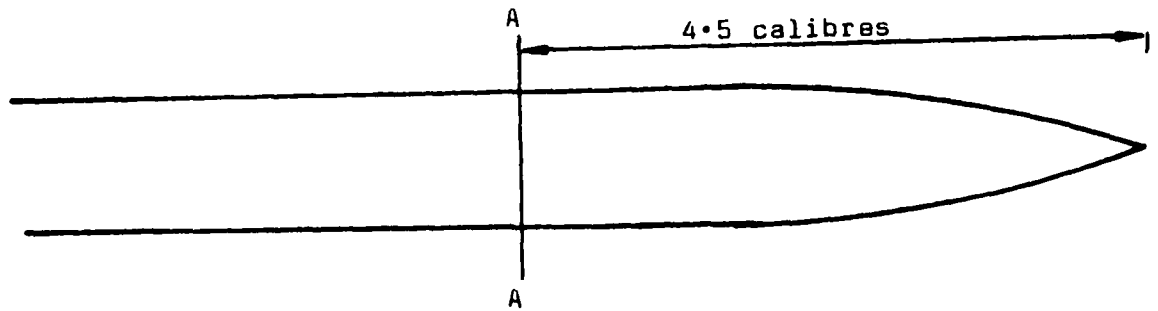
Figure 66



Distribution of Local Force Coefficients
Two Calibre Cone Nose $Re=10^5$



Correlation of Local Side Force First Peak Magnitudes with
Positions of Peaks and with Node Point Positions:-Two Calibre
Cone Nose $Re=10^5$ 50° Incidence



$$\Delta C_p = \frac{P_1 - P_2}{\frac{1}{2} \rho V^2 \sin^2 \alpha}$$

Typical Pressure Coefficient Distribution

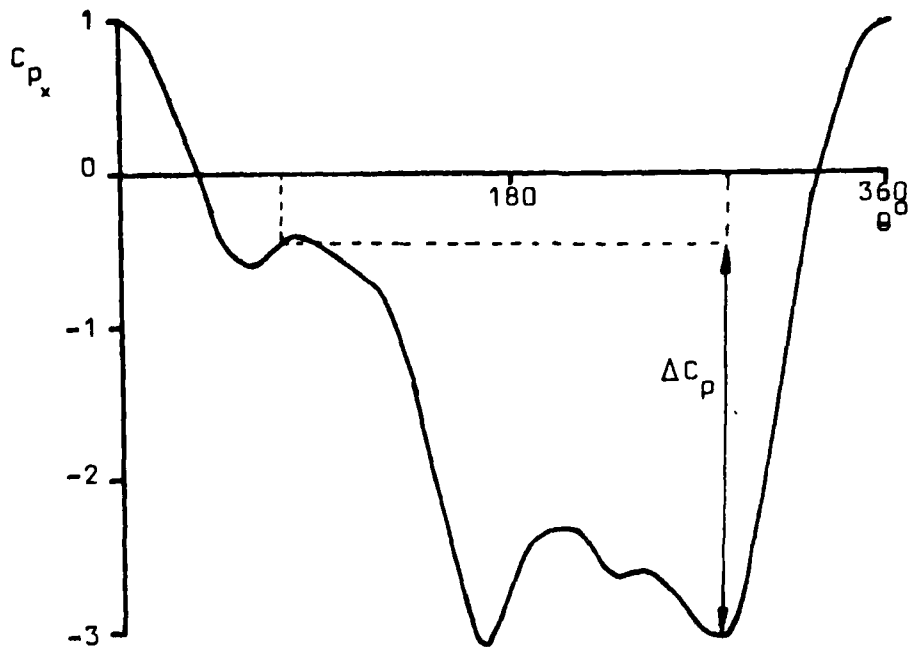
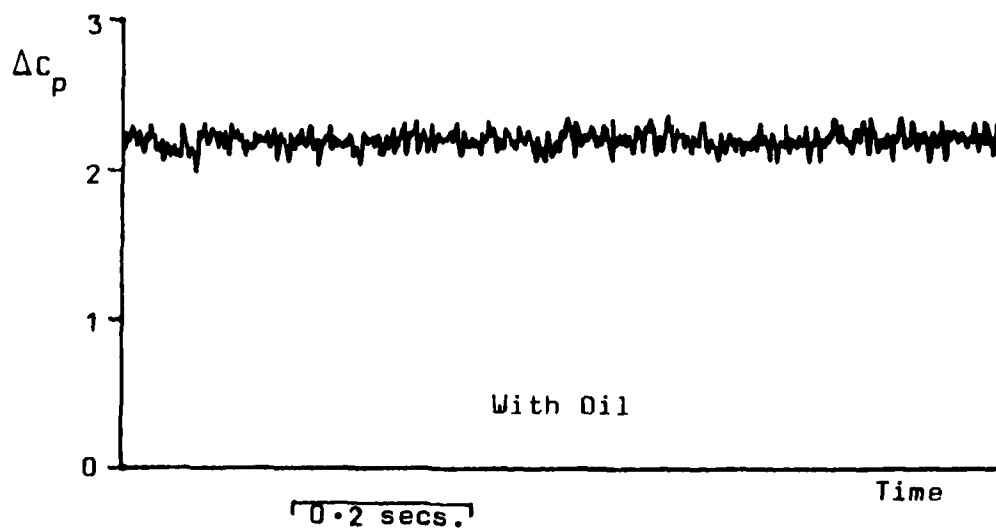
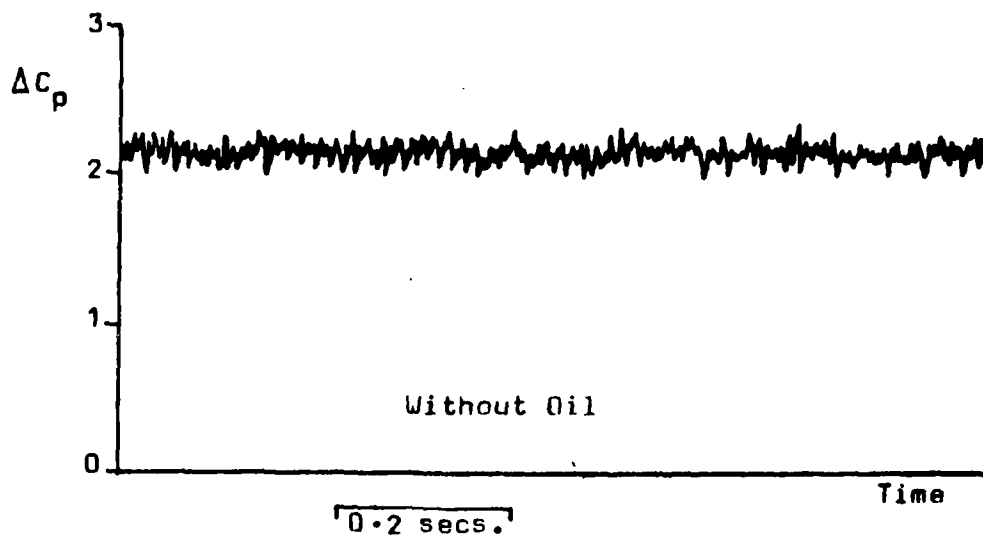


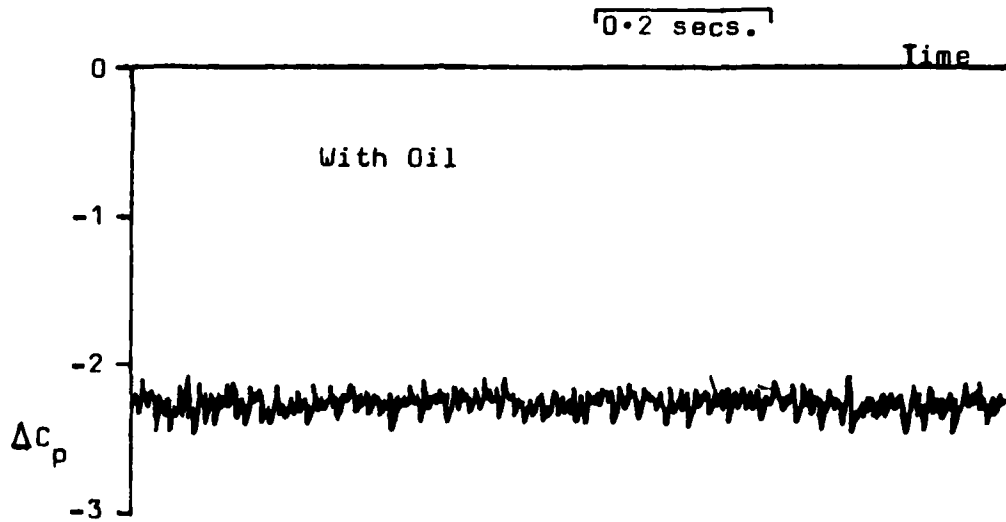
Figure 68



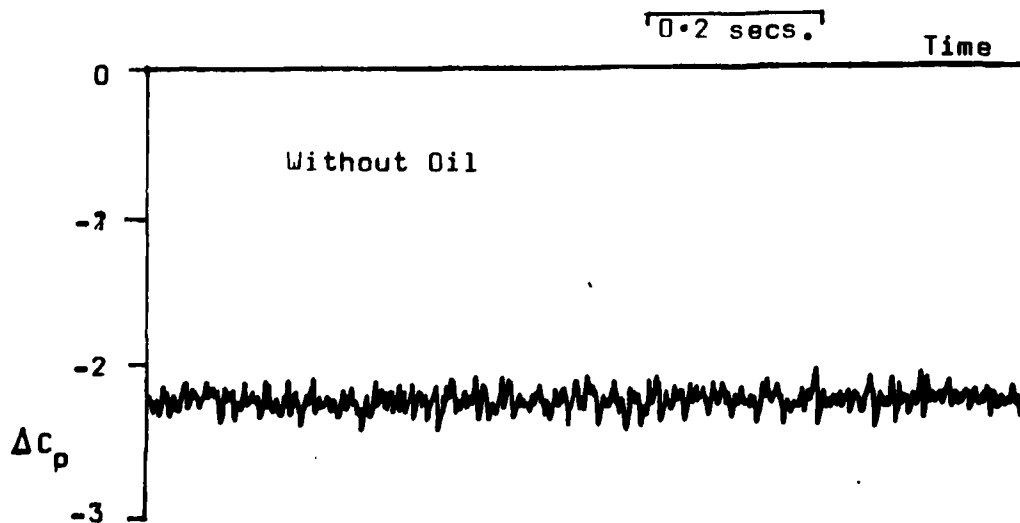
$x/D=4.5$ $Re=10^5$



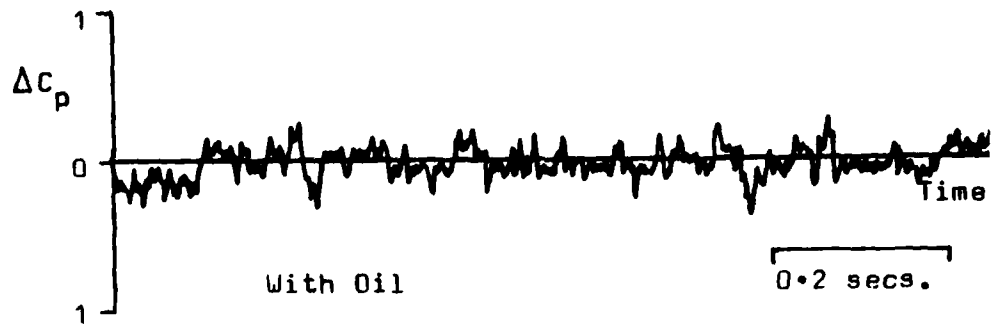
Effect of Oil on Measured Pressure Difference. $\alpha=50^\circ$ $\beta=0^\circ$



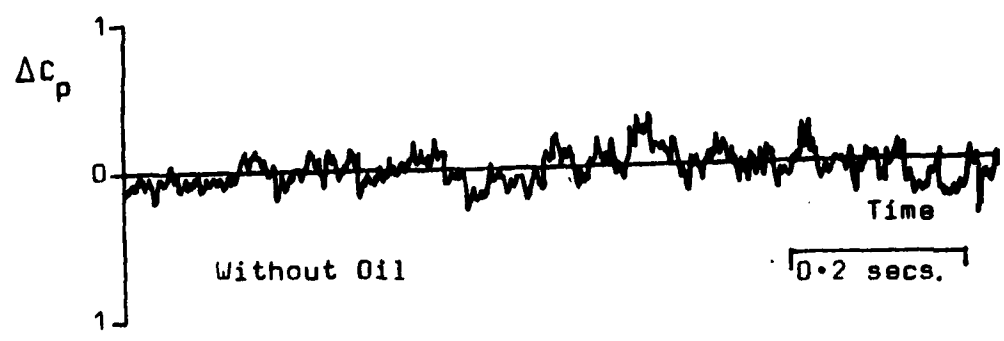
$x/D=4.5$ $Re=10^5$



Effect of Oil on Measured Pressure Difference. $\alpha=50^\circ$ $\beta=90^\circ$
Figure 70



$x/D=4.5 \quad Re=10^5$



Effect of Oil on Measured Pressure Difference. $\alpha=50^\circ \quad \beta=56^\circ$
 Figure 71



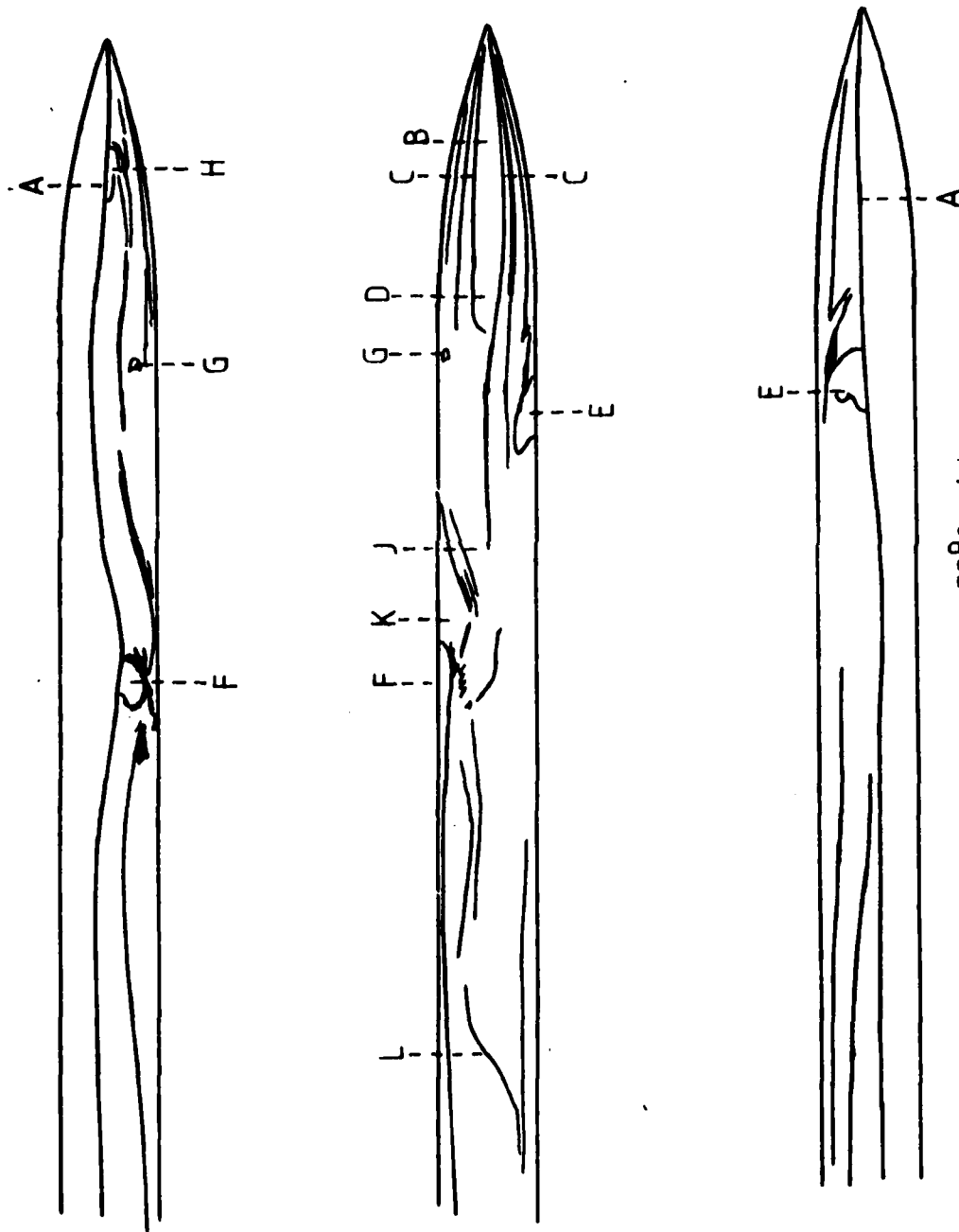
FIGURE 72 SURFACE FLOW VISUALISATION 50° INCIDENCE 0° ROLL



FIGURE 73 SURFACE FLOW VISUALISATION 50° INCIDENCE 90° ROLL

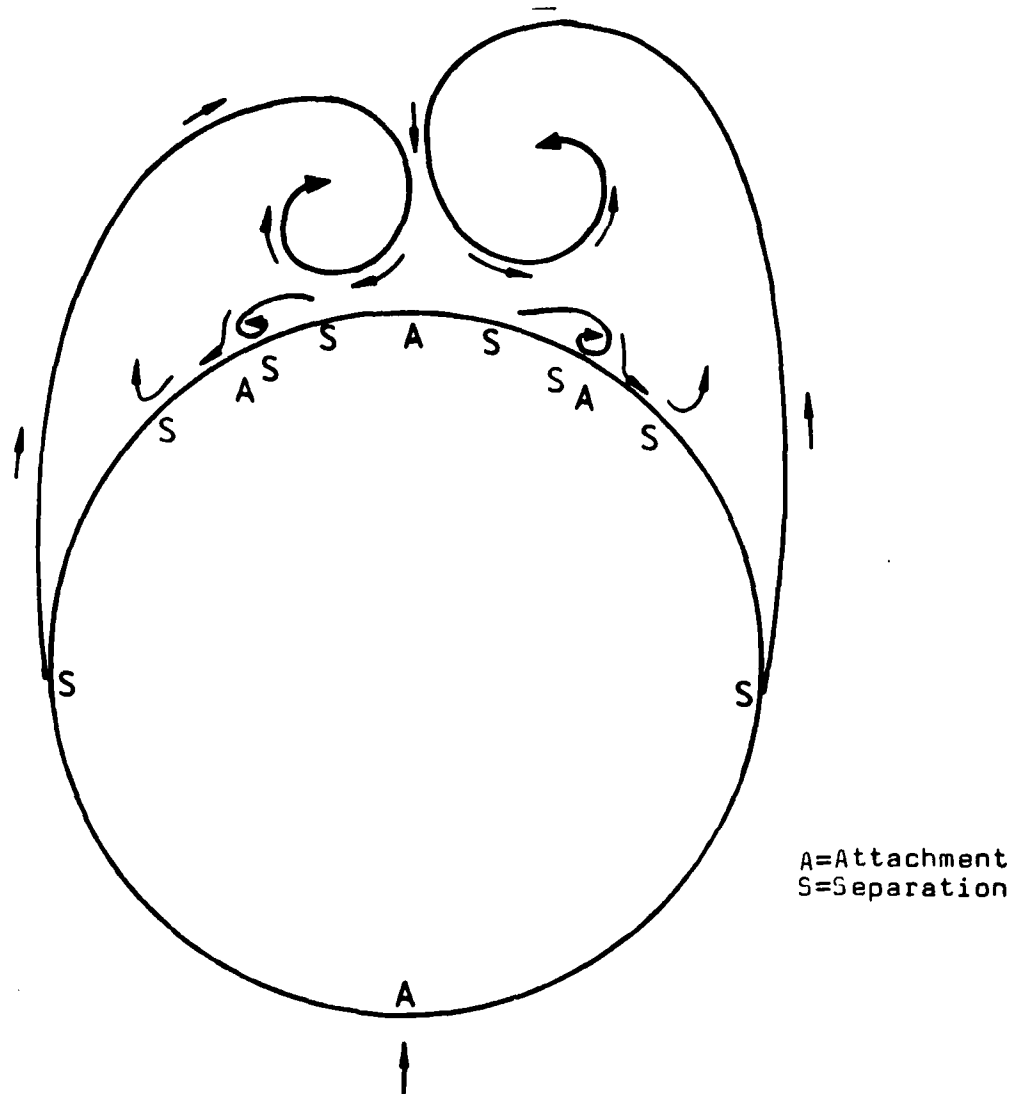


FIGURE 74 SURFACE FLOW VISUALISATION 50° INCIDENCE 56° ROLL



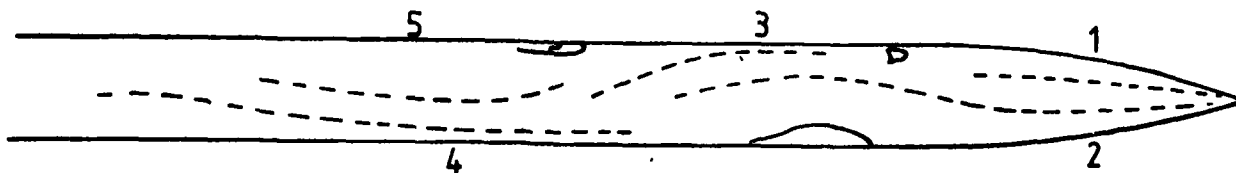
Sketch of Main Surface Flow Features 50° Incidence
 Old Nose 0° Roll Angle

Figure 75

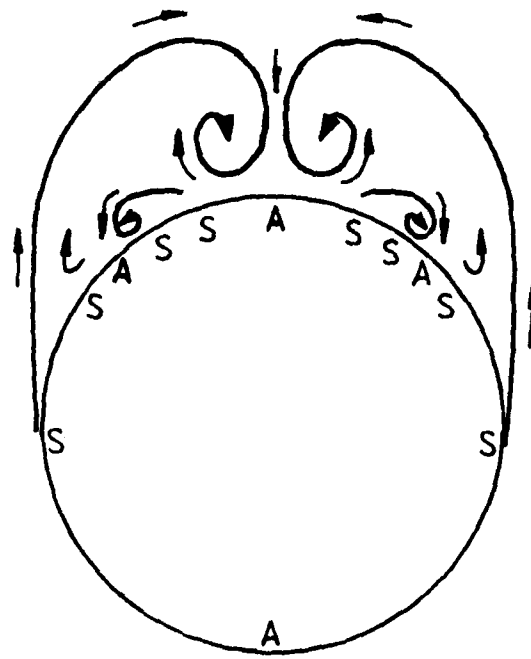


Sketch of Probable Flow Behaviour in the Crossflow Plane
at Stations on the Nose

50° Incidence 0° Roll Angle

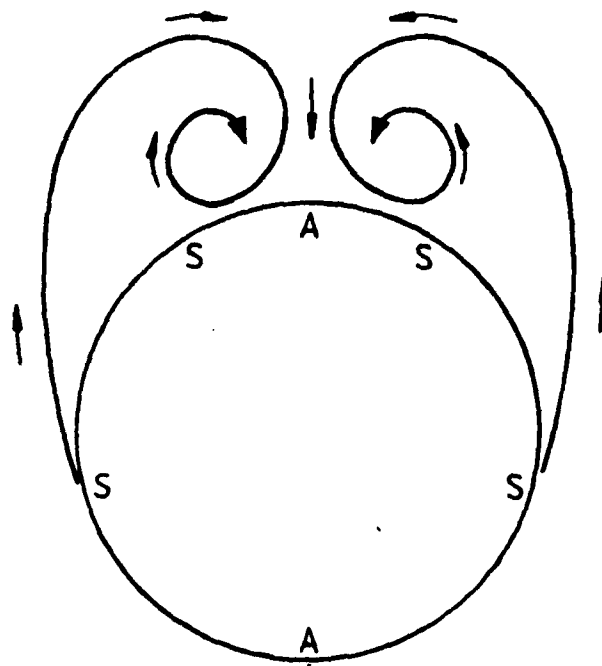


Sketch of Probable Vortex Core Paths in the Vicinity of the
Body Rear View. 50° Incidence 0° Roll Angle



Stations on the Nose

A=Attachment
S=Separation



Stations near $x/D=8$

Sketches of Probable Flow Behaviour in the Crossflow Plane
 50° Incidence 56° Roll Angle

Figure 77

**EN
DAT**